Doctoral Dissertation

Molecular Design of Lithium-ion Solvation and Battery Electrode Reaction in Highly Concentrated Electrolytes (超濃厚電解液中で特有な Li イオン溶媒和と電池電極反応の分子レベルデザイン)

September, 2023

Saki Sawayama

Graduate School of Sciences and Technology for Innovation,

Yamaguchi University

Contents

Chapter 1

General Introduction

1.1 Metal-ion Solvation

1.1.1 *Ion in Solution*

Solvents are used as a reaction field for chemical reactions. In chemical reactions of metal ions, such as metal-ion complexation with ligands and charge-transfer reaction on electrode and so on, "ion solvation" plays a crucial role to directly affect their reactivities. Ions are surrounded several solvent molecules to form a collective ion solvation species in solutions. As solvent parameters that controls the ion-solvent interaction (i.e., solvation), dielectric constant, dipole moment, electron-pair donating and accepting abilities etc. are well known and widely used as an indicator to measure qualitatively the ion-solvent interactions. Particularly, the electron-pair donating and accepting abilities of solvents are useful to estimate the strength of ion-solvent interactions at local scale. Classically, the model for metal ion solvation in aqueous solutions are established as shown in **Figure 1.1**.[1] In Region A, both cations and anions form the first solvation sphere, which contains several solvent molecules via direct ion-solvent interactions. Beyond and adjacent to region A, secondary solvation sphere is formed in region B, which contributes to the ion stabilization through (1) weak indirect electrostatic interactions between the solvent dipole and the ions and (2) weak hydrogen bonds between water molecules between regions A and B. This results in more stable metal ions in enthalpy term; however, the freedom of motion of solvent molecules are largely restricted to be lower entropy state of solvated ions. At a sufficient distance from the ion, solvent molecules in region D (bulk) are not affected to the ion stabilization. Region C found in between regions B and D is a disordered field. The solvent molecules in this region are a high entropy state relative to the bulk (D). Here, in typical aprotic solvents (**Figure 1.2a**), such as acetonitrile (AN), *N*,*N*-dimethylformamide (DMF), and dimethyl sulfoxide (DMSO), the ion solvation can be simplified to be two regions, A (first solvation sphere) and D (bulk). This is because aprotic solvents, unlike water and alcohols, have no intramolecular hydrogen bond accepting sites within a molecule to hardly form a second solvation sphere. Therefore, the reactivity of metal ions in aprotic solvents mainly depends on the first solvation sphere. Therefore, structural study on the first solvation sphere of metal ions is necessary for understanding the metal-ion reactions, such as metal-ion complexation and electrode reaction in aprotic solvent-based electrolyte solutions.

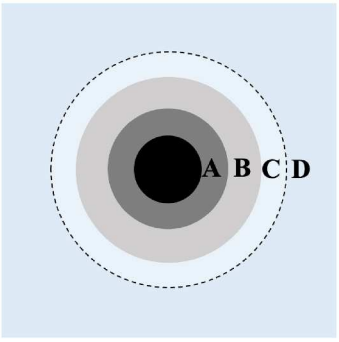

Figure 1.1 Model for metal ion solvation in aqueous solution. The middle black circle: metal ion, A: first solvation sphere, B: second solvation sphere, C: disordered region, and D: bulk.

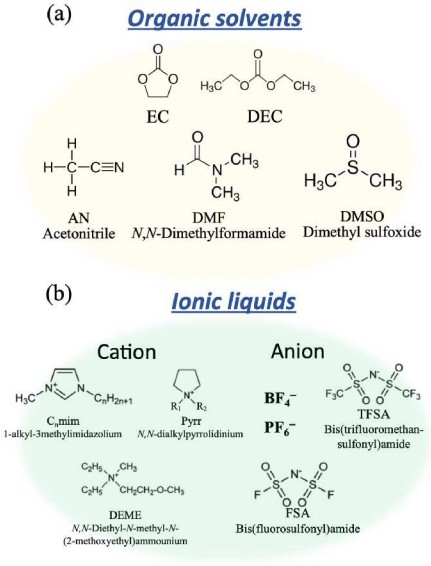

Figure 1.2 Chemical structures of typical (a) organic solvents and (b) ionic liquids (ILs).

1.1.2 *Thermodynamic aspect*

To understand metal-ion solvation on thermodynamic aspect, Born-Harber's cycle process plays a fundamental role to provide an insight based on the thermodynamic quantities (i.e., Gibbs free energy, enthalpy, and entropy).[2] Based on this, ion solvation, in other words, dissociation of salts in solution, is divided into the three processes; (I) sublimation, (II) dissociation, and (III)

solvation, as illustrated in **Figure 1.3**. In process (I), the enthalpy (ΔH°_{sub}) and entropy (ΔS°_{sub}) is positive and their extents depends on the lattice energy in crystal state. The corresponding values in process (II), i.e., an ion-pair dissociates into sole cation and anion, are also positive. When the resulting each ion is added to solution, the cation and anion are solvated with solvent molecules to stabilize the ions in free energy. In the case of overall $\Delta G^{\circ} < 0$ (i.e., sum of processes (I + II) and (III) is negative), the salt dissolutes completely in solution. Therefore, the magnitude of solvation Gibbs energies of the cation and anion determine the salt solubility, which is deeply related to the reactivity of metal ions in metal-ion complexation and electrode redox reaction.

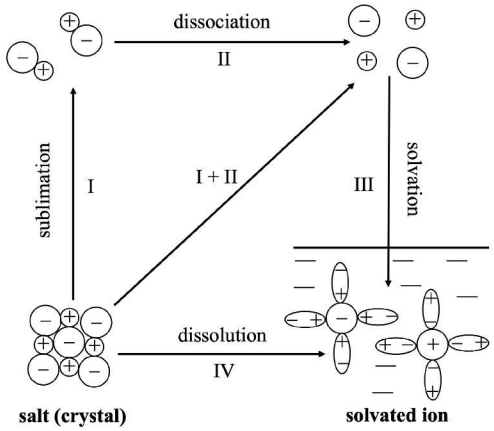

Figure 1.3 The Born-Harber's cycle for dissolution of salt (crystal).

1.1.3 *Role of Solvent molecules*

In organic electrolyte system, some important factors, e.g., (1) the solvation number (n) of metal ions,[3-8] (2) the electron-pair donating ability of solvent molecule (i.e., Gutmann's donor number, D_N),[9, 3-4] and (3) the size of the solvent molecules (i.e., bulkiness),[10, 4] have been recognized to control the metal-ion solvation. Firstly, the solvation number generally depends on the ionic radius and charge of metal ion species, M^{n+}. Many techniques have been brought to bear on the problem of establishing average solvation number for ions in solution, with varying degrees of usefulness and success. For example, using (1) spectroscopy (NMR, ultraviolet-visible (UV), Raman or infrared (IR)), (2) Transport properties (transport numbers, ionic conductivities, mobilities, and viscosities), (3) X-ray/neutron scattering, the average solvation number has been established to be ~4 for small monovalent ions (Li^+, Be^+, Ag^+), ~6 for typical monovalent and divalent ions (alkali metal, alkaline earth metal, and first transition metal ions), and ~8 for trivalent lanthanide ions.[1] Secondly, the electron pair-donating ability of a solvent molecule, which is solvation power of solvent molecule to metal ion, is quantified by Guttman's donor number, D_N.[11] The D_N values of typical aprotic dipole solvents, such as DMF and DMSO (26.6 and 29.8, respectively) are quite larger than that of water (18.0), whereas AN and ethylene carbonate (EC) have smaller D_N values (14.1 and 16.4, respectively) compared to water. On the basis of the D_N values, we can easily expect solvation selectivity in binary or more solvent mixture systems; e.g., if DMF and AN coexist in an electrolyte solution including a certain metal ion, the DMF molecules preferentially solvate to a metal ion relative to AN molecules. The D_N value is also as an indicative parameter to predict salt-dissociation ability in electrolyte solutions; in this case, the electron-pair accepting ability (A_N) also plays a key role in terms of "anion-solvation". Finally, the solvent bulkiness triggers solvation steric effect (or steric repulsion) among the solvent molecules coordinated with metal ions, leading to reducing solvation number and weakened ion-solvent interactions. Ishiguro et al., who firstly pointed out "solvation steric effect" in electrolyte solution using bulky solvent, demonstrated that an octahedrally six-coordinated transition metal ion reduces in solvation number in aprotic bulky solvent *N*,*N*-dimethylpropionamide to be approximately 4.[12-13]

1.2 Li-ion Batteries

Electrochemical energy storage devices, such as rechargeable secondary batteries and supercapacitors have been required to achieve a high energy density and power density for a main power source in large-scale applications. Among them, lithium-ion batteries (LIBs) are one of most important devices and have been widely used because of various positive feature, the high operation voltage, high energy density, and electrochemical/thermodynamic stabilities. LIBs mainly consist of two different electrodes (i.e., positive and negative electrodes), electrolytes, and also separator and so on. In general, graphite and layered transition metal oxide including Li (i.e., $LiCoO_2$, $LiFePO_4$, $LiMn_2O_4$ etc.) are used as the anode and cathode electrodes, respectively. The separator, which is typical from microporous polymer films made with polypropylene and polyethylene, filled with electrolyte solution acts as preventing directly contact between anode and cathode electrodes. The electrolyte dissolving a Li salt in solvents is filled in the LIB cells and plays an important role, i.e., moving Li-ions between anode and cathode on storing the electrochemical energy. The LIBs store electrochemical energy via the chemical reaction as following:

$$\text{Anode: } C + xLi^+ \rightleftarrows Li_xC \quad (2),$$

$$\text{Cathode: } LiMO_2 \rightleftarrows Li_{1-x}MO_2 + xLi^+ \quad (3),$$

Overall reactions: $C + LiMO_2 \rightleftarrows Li_xC + Li_{1-x}MO_2$ (4),
*M: metals of Co, Mn

where (2), (3), and (4) represented the chemical reaction formulas at anode, cathode, and overall reaction formula, respectively. When LIB is charged, Li ions move from cathode to anode and are intercalated into anode electrode in right direction above the formulas. As for discharging LIB, the opposite reaction is occurred in left direction. It is called as Li-ion insertion/desertion reaction, on each electrode during charge/discharge process, which is illustrated in **Figure 1.4**.

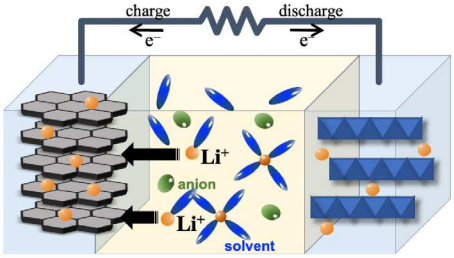

Figure 1.4 The components and principle of common Li-ion batteries.

It has been established that the LIB reaction mechanism includes several stages, as shown in **Figure 1.5**. Firstly, (1) when the Li salt is dissolved in solvent to dissociate to cation and anion, a Li-ion solvation cluster with four-coordinated solvent molecules, $[Li(solvent)_4]^+$, is formed in electrolyte solution. (2) The formed Li-ion cluster and counter-anion diffuse in the bulk electrolyte. In general, the ion diffusion can be characterized based on the Stokes-Einstein equation (eq. 5)[16] as follows,

$$D = kT/C_{SE}\eta r \qquad (5),$$

where D is the diffusion coefficient, k is the Boltzmann constant, T is the absolute temperature, and η is the viscosity. The constant term C_{SE} is specified as 6π when the viscous medium clings to the diffusing particles and as 4π when the diffusing particles slide and move independently of the medium. It is well known that in electrolyte solution system, the C_{SE} is often intermediate value between 6π and 4π.[17] The r is the hydrodynamic radius, corresponding to the size of an ion solvation cluster in solution. The diffusion coefficients of positive and negative ions, D_+ and D_-, respectively, is related to the theoretical molar conductivity (Λ_{NE}) via the Nernst-Einstein equation (eq. 6).

$$\Lambda_{NE} = F^2/RT(D_+ + D_-) \qquad (6),$$

where F is Faraday's constant and R is the gas constant. The self-diffusion coefficient is obtained by various methods as an averaged value of the isolated and aggregated ion species, but the measured molar conductivity Λ_M is usually smaller than Λ_{NE} because only dissociated ion species that can sense the electric field between electrodes are counted for the ionic conductivity. High ionic conductivity by ionic diffusion is essential to cause fast charge-discharge reactions in the LIBs. Finally, (3) Li-ions intercalate into the layered electrode material by desolvation of Li-ion cluster during the charge transfer process near the electrode/electrolyte interface. Abe et al. pointed out that the desolvation process is a key to control the electrode reaction kinetics.[18-20] (Details are provided in section **1.4**).

1.3 Electrolyte Solutions

1.3.1 *Organic Electrolytes*

Organic electrolytes (**Figure 1.2a**) occupy an important position for the development of promising energy storage device applications, such as LIBs, allowing

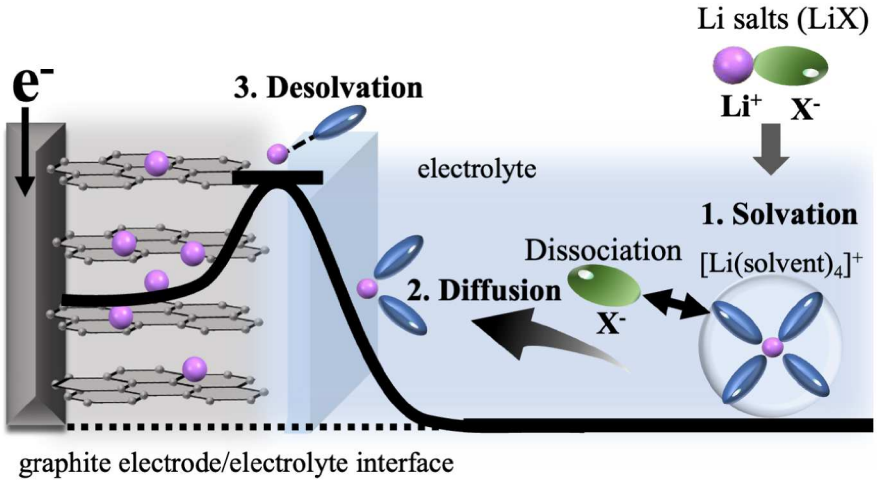

Figure 1.5 Illustration of the LIB electrode reaction process from the bulk electrolyte to the electrode/electrolyte interface.

higher operation voltage and higher ionic conduction compared with aqueous electrolyte solution. In conventional LIBs, it is well known that carbonate-based electrolytes including EC and linear carbonates (dimethyl carbonate (DMC) or/and diethyl carbonate (DEC)) need to use for working stable and reversible LIBs. It should be noted that the carbonate components, especially EC, can occur reductive decomposition during the initial charging process (on the Li-ion insertion) and forms stable passivation films, so called solid electrolyte interphase (SEI), on the graphite anode. This leads to suppress further decomposed products during subsequent charge/discharge cycles.[21-24] The forming SEI allows a reversible Li-ion insertion/deinsertion into/from the graphite anode. For the design of LIB electrolytes, commercialized system, i.e., 1.0 mol dm^{-3} $LiPF_6$/EC+DMC (1:1 by volume) has been optimized, which exhibits the highest ionic conductivity (~ 12 mS cm^{-1})[25] among the other electrolyte with organic solvents and forms a stable SEI formations, resulting in a high stability and long cycle life for rechargeable LIBs. However, current carbonate-based electrolyte systems are highly flammable and volatile owing to the use of organic solvents, which may cause catastrophic fires or explosions, preventing further enlargement and higher capacity of LIBs. Therefore, it is essential to establish safe electrolyte materials, like the nonflammable electrolytes, which include combustion inhibitors and self-extinguishing solvent, and solid-state conversion of liquid electrolytes.

1.3.2 *Nonflammable Electrolytes*

The important factor for the practical LIB application is "safety". One promising approach to establish safe battery system is the application of ionic liquids (ILs), which is due to its inherent negligible volatility and nonflammability.[26-29, 30] ILs consist of only ions (cation and anion, **Figure 1.2b**) and their physicochemical and electrochemical properties depend on their ion structure and combination of ion species. In particular, ILs containing the FSA anion (e.g., [C_2mIm][FSA]:1-ethyl-3-methylimidazolium bis(fluorosulfonyl)amide[31-32]) allow for stable electrode reaction for the graphite electrode, resulting in promising rechargeable IL-based LIBs.[33-35] Indeed, the FSA-based IL electrolytes showed reversible Li insertion/deinsertion reported firstly by Ishilawa et al. (**Figure 1.6**).

Another approach to nonflammable LIB electrolytes is the "addition of nonflammable solvents" into the current conventional carbonate-based electrolytes. In our previous research, we chose fluorinated solvent; tris(2,2,2-trifluoroethyl)phosphate (TFEP) among nonflammable solvents, which is applied as a flame retardant for LIB electrolytes by Xu et al.[36] TFEP has no

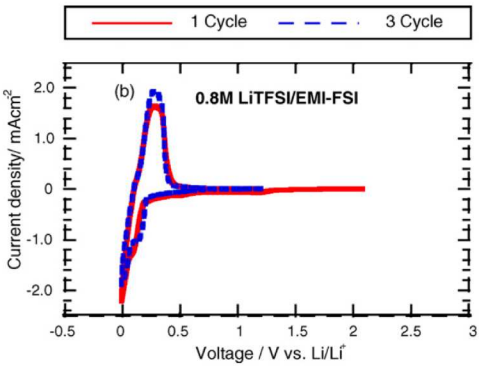

Figure 1.6 Cyclic voltammograms for the graphite electrode in 0.8 M LiTFSA/[C_2mIm][FSA] electrolyte at a scan rate 0.1 mV s^{-1}. (ref. 33, Figure 2b).

flash point and is therefore categorized as a non-hazardous material. The resulting nonflammable electrolytes [i.e., 1.0 mol dm^{-3} $LiPF_6$/EC+DEC containing TFEP] were characterized from both physicochemical and electrochemical viewpoints.[37-41, 10, 4, 6, 42-45] In the EC:DEC:TFEP = 53:27:20 (by volume) electrolyte solution, (1) the electrolyte exhibited a high ionic conductivity (7.5 mS cm^{-1} at 298 K), which exceeds the requirement for practical LIBs (1 mS cm^{-1}), and (2) the electrolyte showed good charge/discharge capacities and reversibility at the graphite electrode. Thus, the system exhibits safe and good LIB performances. Furthermore, we found that the used of TFEP as a "main solvent" showed an excellent thermal stability even at elevated temperature. This advantage characteristic is an essential key for designing much safer LIB electrolytes. However, in the TFEP-based electrolyte system, it has not yet clarified Li-ion solvation structures at the molecular levels, which is key to control the LIB electrode reaction.

1.3.3 *Concentrated Electrolytes*

Recently, a new conceptual LIB electrolyte: concentrated electrolyte comprising extremely high concentrations of Li salt (near or equimolar mixing ratio of Li salt-to-solvent, 1/2 ~ 1/1) has attracted attention as a promising candidate for practical LIB electrolyte and has thus been widely investigated from the viewpoints of battery application and science.[46-54] The electrolyte, also known as "Solvent-in-Salt" liquids, exhibits excellent LIB performance, which is comparable to the current commercialized systems even in carbonate solvent-free state, and acceptable ionic conductivity despite its high viscosity. A typical example is a concentrated aqueous electrolyte system using only Li salt and water to substantially improve the limited electrochemical stability of water (1.23 V)[55] up to 3–3.8 V, resulting in the development of excellent aqueous

LIBs (**Figure 1.7a**).[46, 48-49, 52, 56] Furthermore, a new category of Li-ion conductive liquid based on water, "hydrate-melt" has also reported by Yamada et. al. (**Figure 1.7b**).[57, 52] When two specific Li salts are mixed with water in certain ratio, it found that Li salt dihydrate, which is generally as a solid state, exists as a stable liquid state at room temperature. Indeed, this electrolyte exhibits high voltage tolerance and high Li-ion transport property, enabling a reversible reaction at a commercial $Li_4Ti_5O_{12}$ negative electrode with a low reaction potential (1.55 V versus Li^+/Li) and a high capacity (175 mAh g^{-1}). The resultant aqueous LIBs with high energy density (> 130 Wh kg^{-1}) and high voltage (~2.3–3.1 V) represent significant progress towards performance comparable to that of commercial non-aqueous batteries (with energy densities of ~150–400 Wh kg^{-1} and voltages of ~2.4–3.8 V). These improvement originate from the unique liquid structures in concentrated electrolytes;[46, 57, 50] in detail, (1) all of solvent molecules and counter-anions coordinate to Li-ions, i.e., there are no free solvent molecules in the bulk phase, and thus (2) the Li-ions form the specific ion-ordering structures with complicated multiple ion pairs, (**Figure 1.7c,** in the case of water electrolyte) to modify the electronic state (HOMO/LUMO energy levels) of the counter anions coordinated to the Li-ion change (**Figure 1.8a and b**, in the case of AN electrolytes), resulting in the formation

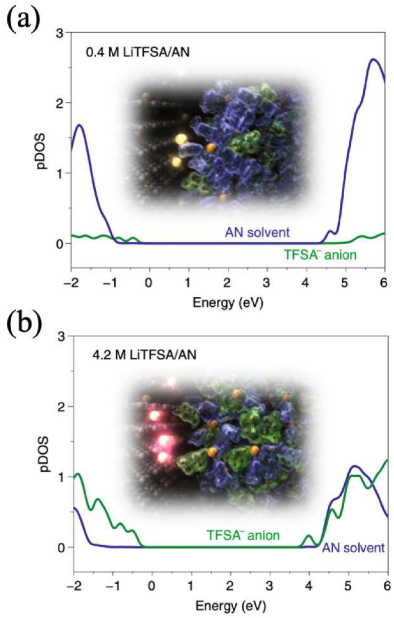

Figure 1.8 (a, b) Calculated electronic structures (projected density of states, pDOS) of (a) dilute 0.4 M, and (b) concentrated 4.2 M LiTFSA/AN electrolytes. Insets show images of the interface between the electrolyte and graphite electrode. (ref. 53, Figure 1d and e).

of a stable anion-derived SEI at the negative electrode.[6, 50] As a results, the concentrated electrolyte improve

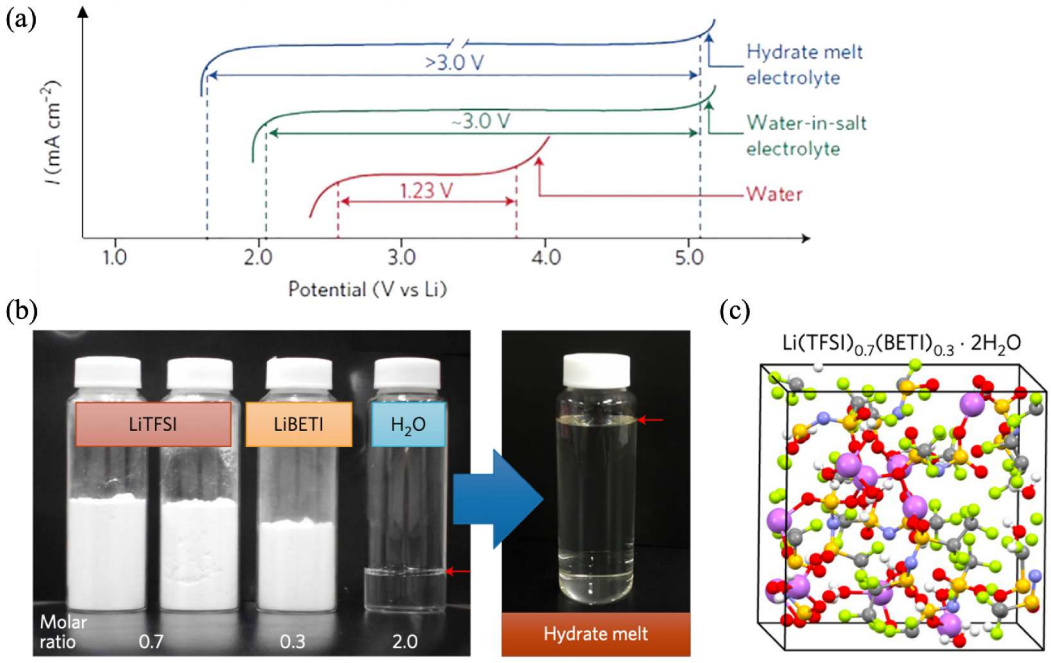

Figure 1.7 (a) Electrochemical windows measured for water at pH = 7, water-in-salt electrolyte (21 mol kg^{-1} LiTFSA in water), and hydrate melt electrolyte (27.8 mol kg^{-1} LiTFSA+LiBETA in water) [ref. 46, Figure 5Bd], (b) Stoichiometric amounts of LiTFSI, LiBETI and water used to prepare a $Li(TFSI)_{0.7}(BETI)_{0.3}\cdot 2H_2O$ hydrate melt. The red arrows indicate the liquid levels. (ref. 52, Figure 1b). (c) Snapshots of equilibrium trajectories obtained from first-principles DFT-MD simulations of $Li(TFSI)_{0.7}(BETI)_{0.3}\cdot 2H_2O$ hydrate melt (28 mol kg^{-1}). Atom colors: Li, purple (presented with a larger size for emphasis); C, dark grey; H, light grey; O, red; N, blue; S, yellow; F, light green. (ref. 52, Figure 2d).

oxidative/reductive stabilities leads to expand its electrochemical window.

Furthermore, in concentrated sulfolane (SL)-based electrolytes, it reported the Li-ion within the ion-ordering structures exhibit a unique Li-ion hopping/exchange mechanism and show high Li-ion conduction behavior (i.e., Li transference number, $t_{Li} \sim 1$, **Figure 1.9**).[58-59] Therefore, it is suggested that control of the "specific ion-ordering structures" of the concentrated electrolytes, which is not found dilute systems, influences the LIB performance.[60, 50] Several combinations of Li salts and solvents have been examined in terms of LIB electrochemistry/technology to optimize their compositions;[61, 48-49, 51, 62-63] however, the fundamental knowledge of the structure formation mechanism at a molecular level is limited.

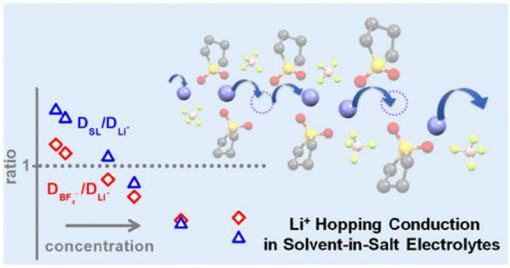

Figure 1.9 Promotion of Li-ion hopping/exchange mechanism and Li transference number (t_{Li}) in concentrated SL-based electrolyte. (ref. 59, Abstract)

1.4 Electrode Reaction Mechanism for LIBs

The LIB electrode reaction mechanism has been established in a dilute electrolyte system (e.g., 1.0 mol dm^{-3} Li salt in solvent mixtures of cyclic and linear carbonates).[18-20] Kinetic studies on an intercalation-type electrode, such as a graphite electrode, have been actively reported to provide molecular insights into the Li-ion intercalation process. Abe et al. reported that the activation energy (E_a) on the Li^+-insertion reaction for the graphite electrode in dilute carbonate-based electrolyte to be 53 – 59 kJ mol^{-1}, which was mainly attributed to the desolvation process for solvated Li-ions, usually 4-coordinated $[Li(solvent)_4]^+$ complex, near the electrode/electrolyte interface.[18-20] Further systematic investigation on electrode reaction kinetics reveals the following results:[20] (1) The E_a value strongly depends on the solvation power of the solvent molecule (D_N); that is, stronger Li-ion solvation (**Figure 1.10a**) leads to larger E_a value, resulting in kinetically unfavorable Li-ion intercalation (**Figure 1.10c**, pass I). However, weaker Li-ion solvation (**Figure 1.10b**) leads to smaller E_a value, resulting in kinetically favorable Li-ion intercalation (**Figure 1.10c**, pass II). (2) In such an intercalation-type reaction, the charge transfer process is almost independent of negative electrode materials and passivation SEI films; that is, only Li-ion desolvation is predominant in reflecting the E_a value. Therefore, controlling ion-solvent interactions to achieve "much weaker Li-ion coordination" may be a key to developing

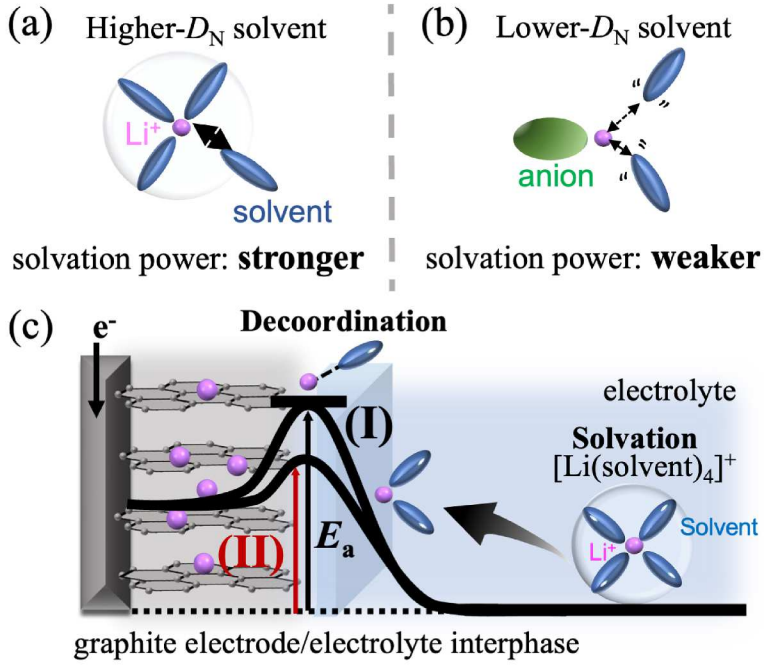

Figure 1.10 Schematic illustration of the interaction of Li ion with (a) higher-D_N solvent and (b) lower-D_N solvent, and (c) possible electrode reaction mechanism via the Li ion decoordination at the charge transfer reaction for the graphite anode.

practical LIBs with high-rate performance. However, an electrode reaction kinetics and mechanism at the electrode/electrolyte interface in concentrated electrolyte systems have not been clarified detail at the molecular levels.

1.5 Purpose of This Study

As mentioned above, to develop new nonflammable LIB electrolytes using fluorinated solvents, I focused on the "Li-ion solvation" in their electrolytes, which directly control the LIB electrode reaction. My major focus is to structurally design the Li ion solvation in the highly concentrated nonflammable electrolytes at the molecular level to control the LIB electrode reaction using the graphite electrode as a model system. The detailed procedures of experimental and theoretical methods are described in Chapter 2. In Chapter 3, I focused on tris(2,2,2-trifluoroethyl)phosphate (TFEP) as an electrolyte solvent for nonflammable LIBs, which has a bulky molecular structure (molecular volume: 288.6 $Å^3$). The combined structural and electrochemical study was performed for the TFEP-based electrolyte containing LiFSA salt in dilute salt condition to demonstrate successful Li-ion insertion reaction into a graphite electrode triggered via a structural control of Li-ion solvation by introducing a small-size molecule into the TFEP electrolytes. In Chapter 4, I extended the LiFSA/TFEP electrolytes to concentrated electrolytes and proposed a molecular design for Li ion-ordered structures that facilitates the LIB electrode reaction. In Chapter 5, the 2,2,2-trifluoroethyl acetate (TFEAc) having smaller molecular size (147.5 $Å^3$), and weaker coordination power was selected as a main solvent among fluorinated solvents to find out the role of the two solvent characteristics on the ion solvation and electrode reaction in dilute LiTFSA/TFEAc electrolytes. In Chapter 6, I tried to establish the highly concentrated electrolyte based on the TFEAc solvent, resulting in a kinetically favorable electrode reaction with lower activation energy. Finally, I summarized overall conclusion in Chapter 7, and pointed out the importance of the solvent parameters; particularly, molecular size and coordination power to metal ions of solvent molecule, on the battery electrode reaction.

1.6 References

(1) Burgess, J. *Ions in Solution, 2nd ed.*, Horwood Publishing: 1999.

(2) Ishida, Y. A Study on the Hydration of Ion. *BULL. SHIMANE UNrv.* **1961,** *10*, 17-27.

(3) Sawayama, S.; Ochi, R.; Mimura, H.; Morita, M.; Fujii, K. 2,2,2-Trifluoroethyl Acetate as an Electrolyte Solvent for Lithium-Ion Batteries: Effect of Weak Solvation on Electrochemical and Structural Characteristics. *J. Phys. Chem. C* **2021,** *125*, 27098-27105.

(4) Sawayama, S.; Todorov, Y. M.; Mimura, H.; Morita, M.; Fujii, K. Fluorinated alkyl-phosphate-based electrolytes with controlled lithium-ion coordination structure. *Phys. Chem. Chem. Phys.* **2019,** *21*, 11435-11443.

(5) Shibata, M.; Sawayama, S.; Osugi, M.; Fujii, K. Structural aspect on "Salting-in" mechanism of PEG chains into a phosphonium-based ionic liquid using lithium salt. *J. Mol. Liq.* **2022,** *366*, 120255.

(6) Sogawa, M.; Sawayama, S.; Han, J.; Satou, C.; Ohara, K.; Matsugami, M.; Mimura, H.; Morita, M.; Fujii, K. Role of Solvent Size in Ordered Ionic Structure Formation in Concentrated Electrolytes for Lithium-Ion Batteries. *J. Phys. Chem. C* **2019,** *123*, 8699-8708.

(7) Sogawa, M.; Todorov, Y. M.; Hirayama, D.; Mimura, H.; Yoshimoto, N.; Morita, M.; Fujii, K. Role of Solvent Bulkiness on Lithium-Ion Solvation in Fluorinated Alkyl Phosphate-Based Electrolytes: Structural Study for Designing Nonflammable Lithium-Ion Batteries. *J. Phys. Chem. C* **2017,** *121*, 19112-19119.

(8) Suzuki, K.; Sawayama, S.; Deguchi, Y.; Sai, R.; Han, J.; Fujii, K. A structural and electrochemical study of lithium-ion battery electrolytes using an ethylene sulfite solvent: from dilute to concentrated solutions. *Phys. Chem. Chem. Phys.* **2022,** *24*, 27321-27327.

(9) Doi, T.; Fujii, R.; Aoki, Y.; Nagashima, T.; Takehara, K.; Inaba, M. Physicochemical Features of Fluorinated Ethyl Acetate-Based Highly Concentrated Electrolyte Solutions and Their Effects on Electrochemical Properties of $LiNi_{0.8}Co_{0.1}Mn_{0.1}O_2$ Positive Electrodes. *J. Phys. Chem. C* **2021,** *125*, 12578-12584.

(10) Sawayama, S.; Morinaga, A.; Mimura, H.; Morita, M.; Katayama, Y.; Fujii, K. Fluorophosphate-Based Nonflammable Concentrated Electrolytes with a Designed Lithium-Ion-Ordered Structure: Relationship between the Bulk Electrolyte and Electrode Interface Structures. *ACS Appl. Mater. Interfaces* **2021,** *13*, 6201-6207.

(11) GUTMANN, V. EMPIRICAL PARAMETERS FOR DONOR AND ACCEPTOR PROPERTIES OF SOLVENTS. *Electrochemical Acta* **1976,** *21*, 661-670.

(12) Asada, M.; Mitsugi, T.; Ogura, T.; Fujii, K.; Umebayashi, Y.; Ishiguro, S. Solvation number and conformation of *N,N*-dimethylacrylamide and *N,N*-dimethylpropionamide in the coordination sphere of the cobalt(II) ion in solution studied by FT-IR and FT-Raman spectroscopy. *Analytical Sciences* **2007,** *23*, 835-840.

(13) Umebayashi, Y.; Mroz, B.; Asada, M.; Fujii, K.; Matsumoto, K.; Mune, Y.; Probst, M.; Ishiguro, S. Conformation of solvent *N,N*-dimethylpropionamide in

the coordination sphere of the zinc(II) ion studied by Raman spectroscopy and DFT calculations. *J. Phys. Chem. A* **2005,** *109*, 4862-4868.
(14) Xu, W.; Cooper, E. I.; Angell, C. A. Ionic Liquids: Ion Mobilities, Glass Temperatures, and Fragilities. *J. Phys. Chem. B* **2003,** *107*, 6170-6178.
(15) Harris, K. R. Relations between the Fractional Stokes-Einstein and Nernst-Einstein Equations and Velocity Correlation Coefficients in Ionic Liquids and Molten Salts. *J. Phys. Chem. B* **2010,** *114*, 9572-9577.
(16) Edward, J. T. Molecular Volumes and the Stokes-Einstein Equation. *J. Chem. Educ.* **1970,** *47*, 261-270.
(17) Ue, M.; Mori, S. Mobility and Ionic Association of Lithium Salts in a Propylene Carbonate-Ethyl Methyl Carbonate Mixed Solvent. *J. Electrochem. Soc.* **1995,** *142*, 2577-2581.
(18) Abe, T.; Fukuda, H.; Iriyama, Y.; Ogumi, Z. Solvated Li-Ion Transfer at Interface Between Graphite and Electrolyte. *J. Electrochem. Soc.* **2004,** *151*, A1120.
(19) Abe, T.; Sagane, F.; Ohtsuka, M.; Iriyama, Y.; Ogumi, Z. Lithium-Ion Transfer at the Interface Between Lithium-Ion Conductive Ceramic Electrolyte and Liquid Electrolyte-A Key to Enhancing the Rate Capability of Lithium-Ion Batteries. *J. Electrochem. Soc.* **2005,** *152*.
(20) Kondo, Y.; Abe, T.; Yamada, Y. Kinetics of Interfacial Ion Transfer in Lithium-Ion Batteries: Mechanism Understanding and Improvement Strategies. *ACS Appl. Mater. Interfaces* **2022,** *14*, 22706-22718.
(21) Aurbach, D.; Zaban, A.; Ein-Eli, Y.; Weissman, I. Recent studies on the correlation between surface chemistry, morphology, three-dimensional structures and performance of Li and Li-C intercalation anodes in several important electrolyte systems. *J. Power Sources* **1997,** *68*, 91-98.
(22) Fong, R.; Sacken, U. v.; Dahn, J. R. Studies of Lithium Intercalation into Carbons Using Nonaqueous Electrochemical Cells. *J. Electrochem. Soc.* **1990,** *137*, 2009-2013.
(23) Nie, M.; Chalasani, D.; Abraham, D. P.; Chen, Y.; Bose, A.; Lucht, B. L. Lithium ion battery graphite solid electrolyte interphase revealed by microscopy and spectroscopy. *J. Phys. Chem. C* **2013,** *117*, 1257-1267.
(24) Peled, E. The electrochemical behavior of alkali and alkaline earth metals in nonaqueous battery systems—the solid electrolyte interphase model. *J. Electrochem. Soc.* **1979,** *126*, 2047-2051.
(25) Dahbi, M.; Ghamouss, F.; Tran-Van, F.; Lemordant, D.; Anouti, M. Comparative study of EC/DMC LiTFSI and $LiPF_6$ electrolytes for electrochemical storage. *J. Power Sources* **2011,** *196*, 9743-9750.
(26) Armand, M.; Endres, F.; MacFarlane, D. R.; Ohno, H.; Scrosati, B. Ionic-liquid materials for the electrochemical challenges of the future. *Nat. Mater.* **2009,** *8*, 621-629.
(27) Seki, S.; Kobayashi, Y.; Miyashiro, H.; Ohno, Y.; Usami, A.; Mita, Y.; Kihira, N.; Watanabe, M.; Terada, S. Lithium Secondary Batteries Using Modified-Imidazolium Room-Temperature Ionic Liquid. *J. Phys. Chem. B* **2006,** *110*, 10228-10230.
(28) Tokuda, H.; Hayamizu, K.; Ishii, K.; Abu Bin Hasan Susan, M.; Watanabe, M. Physicochemical properties and structures of room temperature ionic liquids. 1. Variation of anionic species. *J. Phys. Chem. B* **2004,** *108*, 16593-16600.
(29) Tokuda, H.; Hayamizu, K.; Ishii, K.; Susan, M. A. B. H.; Watanabe, M. Physicochemical properties and structures of room temperature ionic liquids. 2. Variation of alkyl chain length in imidazolium cation. *J. Phys. Chem. B* **2005,** *109*, 6103-6110.
(30) Watanabe, M. Design and Materialization of Ionic Liquids Based on an Understanding of Their Fundamental Properties. *Electrochemistry* **2016,** *84*, 642-653.
(31) Fujii, K.; Seki, S.; Fukuda, S.; Kanzaki, R.; Takamuku, T.; Umebayashi, Y.; Ishiguro, S.-i. Anion Conformation of Low-Viscosity Room-Temperature Ionic Liquid 1-Ethyl-3-methylimidazolium Bis(fluorosulfonyl) Imide. *J. Phys. Chem. B* **2007,** *111*, 12829-12833.
(32) Lopes, J. N. C.; Shimizu, K.; Pádua, A. A. H.; Umebayashi, Y.; Fukuda, S.; Fujii, K.; Ishiguro, S. Potential Energy Landscape of Bis(fluorosulfonyl)amide. *J. Phys. Chem. B* **2008,** *112*, 9449-9455.
(33) Ishikawa, M.; Sugimoto, T.; Kikuta, M.; Ishiko, E.; Kono, M. Pure ionic liquid electrolytes compatible with a graphitized carbon negative electrode in rechargeable lithium-ion batteries. *J. Power Sources* **2006,** *162*, 658-662.
(34) Matsumoto, H.; Sakaebe, H.; Tatsumi, K.; Kikuta, M.; Ishiko, E.; Kono, M. Fast cycling of $Li/LiCoO_2$ cell with low-viscosity ionic liquids based on bis(fluorosulfonyl)imide $[FSI]^-$. *J. Power Sources* **2006,** *160*, 1308-1313.
(35) Yamagata, M.; Nishigaki, N.; Nishishita, S.; Matsui, Y.; Sugimoto, T.; Kikuta, M.; Higashizaki, T.; Kono, M.; Ishikawa, M. Charge–discharge behavior of graphite negative electrodes in bis(fluorosulfonyl)imide-based ionic liquid and structural aspects of their electrode/electrolyte interfaces. *Electrochimica Acta* **2013,** *110*, 181-190.
(36) Xu, K.; Zhang, S.; Allen, J. L.; Jow, T. R. Evaluation of Fluorinated Alkyl Phosphates as Flame Retardants in Electrolytes for Li-Ion Batteries: II. Performance in Cell. *J. Electrochem. Soc.* **2003,** *150*, A170-A175.

(37) Chen, J.; Naveed, A.; Nuli, Y.; Yang, J.; Wang, J. Designing an intrinsically safe organic electrolyte for rechargeable batteries. *Energy Stor. Mater.* **2020,** *31*, 382-400.
(38) Chikaoka, Y.; Nakata, N.; Fujii, K.; Sawayama, S.; Ochi, R.; Iwama, E.; Okita, N.; Harada, Y.; Orikasa, Y.; Naoi, W.; Naoi, K. Strategy for Ultrafast Cathode Reaction in Magnesium-Ion Batteries Using BF_4 Anion Based Dual-Salt Electrolyte Systems: A Case Study of $FePO_4$. *ACS Appl. Energy Mater.* **2023,** *6*, 4657-4670.
(39) Dong, Y.; Zhang, N.; Li, C.; Zhang, Y.; Jia, M.; Wang, Y.; Zhao, Y.; Jiao, L.; Cheng, F.; Xu, J. Fire-Retardant Phosphate-Based Electrolytes for High-Performance Lithium Metal Batteries. *ACS Appl. Energy Mater.* **2019,** *2*, 2708-2716.
(40) Hazama, T.; Fujii, K.; Sakai, T.; Aoki, M.; Mimura, H.; Eguchi, H.; Todorov, Y.; Yoshimoto, N.; Morita, M. High-performance gel electrolytes with tetra-armed polymer network for Li ion batteries. *J. Power Sources* **2015,** *286*, 470-474.
(41) NAKAGAWA, H.; SHIBATA, Y.; FUJINO, Y.; TABUCHI, T.; INAMASU, T.; MURATA, T. Application of Nonflammable Electrolytes to High Performance Lithium-ion Cells. *Electrochemistry* **2010**, 406-408.
(42) Takada, K.; Yamada, Y.; Yamada, A. Optimized Nonflammable Concentrated Electrolytes by Introducing a Low-Dielectric Diluent. *ACS Appl. Mater. Interfaces* **2019,** *11*, 35770-35776.
(43) Todorov, Y. M.; Aoki, M.; Mimura, H.; Fujii, K.; Yoshimoto, N.; Morita, M. Thermal and electrochemical properties of nonflammable electrolyte solutions containing fluorinated alkylphosphates for lithium-ion batteries. *J. Power Sources* **2016,** *332*, 322-329.
(44) Wang, Q.; Jiang, L.; Yu, Y.; Sun, J. Progress of enhancing the safety of lithium ion battery from the electrolyte aspect. *Nano Energy* **2019,** *55*, 93-114.
(45) Xu, K.; Ding, M. S.; Zhang, S.; Allen, J. L.; Jow, T. R. Evaluation of Fluorinated Alkyl Phosphates as Flame Retardants in Electrolytes for Li-Ion Batteries: I. Physical and Electrochemical Properties. *J. Electrochem. Soc.* **2003,** *150*.
(46) Borodin, O.; Self, J.; Persson, K. A.; Wang, C.; Xu, K. Uncharted Waters: Super-Concentrated Electrolytes. *Joule* **2020,** *4*, 69-100.
(47) Lu, D.; Tao, J.; Yan, P.; Henderson, W. A.; Li, Q.; Shao, Y.; Helm, M. L.; Borodin, O.; Graff, G. L.; Polzin, B.; Wang, C. M.; Engelhard, M.; Zhang, J. G.; De Yoreo, J. J.; Liu, J.; Xiao, J. Formation of Reversible Solid Electrolyte Interface on Graphite Surface from Concentrated Electrolytes. *Nano Lett.* **2017,** *17*, 1602-1609.
(48) Suo, L.; Borodin, O.; Gao, T.; Olguin, M.; Ho, J.; Fan, X.; Luo, C.; Wang, C.; Xu, K. "Water-in-salt" electrolyte enables high-voltage aqueous lithium-ion chemistries. *Science* **2015,** *350*, 938-943.
(49) Suo, L.; Borodin, O.; Sun, W.; Fan, X.; Yang, C.; Wang, F.; Gao, T.; Ma, Z.; Schroeder, M.; von Cresce, A.; Russell, S. M.; Armand, M.; Angell, A.; Xu, K.; Wang, C. Advanced High-Voltage Aqueous Lithium-Ion Battery Enabled by "Water-in-Bisalt" Electrolyte. *Angew. Chem. Int. Ed.* **2016,** *55*, 7136-7141.
(50) Yamada, Y.; Furukawa, K.; Sodeyama, K.; Kikuchi, K.; Yaegashi, M.; Tateyama, Y.; Yamada, A. Unusual Stability of Acetonitrile-Based Superconcentrated Electrolytes for Fast-Charging Lithium-ion Batteries. *J. Am. Chem. Soc.* **2014,** *136*, 5039-5046.
(51) Yamada, Y.; Takazawa, Y.; Miyazaki, K.; Abe, T. Electrochemical Lithium Intercalation into Graphite in Dimethyl Sulfoxide-Based Electrolytes: Effect of Solvation Structure of Lithium Ion. *J. Phys. Chem. C* **2010,** *114*, 11680–11685.
(52) Yamada, Y.; Usui, K.; Sodeyama, K.; Ko, S.; Tateyama, Y.; Yamada, A. Hydrate-melt electrolytes for high-energy-density aqueous batteries. *Nat. Energy* **2016,** *1*, 16129.
(53) Yamada, Y.; Wang, J.; Ko, S.; Watanabe, E.; Yamada, A. Advances and issues in developing salt-concentrated battery electrolytes. *Nat. Energy* **2019,** *4*, 269-280.
(54) Zheng, J.; Lochala, J. A.; Kwok, A.; Deng, Z. D.; Xiao, J. Research Progress towards Understanding the Unique Interfaces between Concentrated Electrolytes and Electrodes for Energy Storage Applications. *Advanced Science* **2017,** *4*, 1700032.
(55) W. Li; J. R. Dahn; Wainwright, D. S. Rechargeable Lithium Batteries with Aqueous Electrolytes. *Science* **1994,** *264*, 1115-1118.
(56) Yang, C.; Chen, J.; Qing, T.; Fan, X.; Sun, W.; von Cresce, A.; Ding, M. S.; Borodin, O.; Vatamanu, J.; Schroeder, M. A.; Eidson, N.; Wang, C.; Xu, K. 4.0 V Aqueous Li-Ion Batteries. *Joule* **2017,** *1*, 122-132.
(57) Miyazaki, K.; Takenaka, N.; Watanabe, E.; Iizuka, S.; Yamada, Y.; Tateyama, Y.; Yamada, A. First-Principles Study on the Peculiar Water Environment in a Hydrate-Melt Electrolyte. *J. Phys. Chem. Lett.* **2019,** *10*, 6301-6305.
(58) Alvarado, J.; Schroeder, M. A.; Zhang, M.; Borodin, O.; Gobrogge, E.; Olguin, M.; Ding, M. S.; Gobet, M.; Greenbaum, S.; Meng, Y. S.; Xu, K. A carbonate-free, sulfone-based electrolyte for high-voltage Li-ion batteries. *Materials Today* **2018,** *21*, 341-353.
(59) Dokko, K.; Watanabe, D.; Ugata, Y.; Thomas, M. L.; Tsuzuki, S.; Shinoda, W.; Hashimoto, K.; Ueno, K.; Umebayashi, Y.; Watanabe, M. Direct Evidence for Li Ion Hopping Conduction in Highly Concentrated Sulfolane-Based Liquid Electrolytes. *J. Phys. Chem. B* **2018,** *122*, 10736-10745.

(60) Sodeyama, K.; Yamada, Y.; Aikawa, K.; Yamada, A.; Tateyama, Y. Sacrificial Anion Reduction Mechanism for Electrochemical Stability Improvement in Highly Concentrated Li-Salt Electrolyte. *J. Phys. Chem. C* **2014,** *118*, 14091-14097.
(61) Nie, M.; Abraham, D. P.; Seo, D. M.; Chen, Y.; Bose, A.; Lucht, B. L. Role of Solution Structure in Solid Electrolyte Interphase Formation on Graphite with LiPF6in Propylene Carbonate. *J. Phys. Chem. C* **2013,** *117*, 25381-25389.
(62) Yamada, Y.; Usui, K.; Chiang, C. H.; Kikuchi, K.; Furukawa, K.; Yamada, A. General observation of lithium intercalation into graphite in ethylene-carbonate-free superconcentrated electrolytes. *ACS Apppl. Mater. Interfaces* **2014,** *6*, 10892-10899.
(63) Yoshida, K.; Nakamura, M.; Kazue, Y.; Tachikawa, N.; Tsuzuki, S.; Seki, S.; Dokko, K.; Watanabe, M. Oxidative-Stability Enhancement and Charge Transport Mechanism in Glyme-Lithium Salt Equimolar Complexes. *J. Am. Chem. Soc.* **2011,** *133*, 13121-13129.

Chapter 2

Experimental

2.1 Materials

LiFSA [FSA: bis(fluorosulfonyl)amide; Kanto Chemical, battery grade] and LiTFSA [TFSA: bis(trifluoromethanesulfonyl)amide; Kanto Chemical, battery grade] salt was vacuum dried at 373 K for 50 h before use. TFEP [tris(2,2,2-trifluoroethyl)phosphate] ; TOSOH FINECHEM, battery grade), AN (acetonitrile; FUJIFILM Wako Pure Chemical, CO., super-dehydrated), [C_2mIm][FSA] (1-ethyl -3-methylimidazolium FSA; Kanto Chemical), TFEAc (2,2,2-trifluoroethyl acetate; TOSOH FINECHEM, battery grade) and EC (ethylene carbonate; Kishida Chemical, battery grade) were used without further purification. Sample electrolyte solutions were prepared by weighing the solvent and Li salt to the required molar ratio (Li salt:solvent) in an Ar-filled glovebox; the corresponding molarities (Li salt concentration, c_{Li}) were then calculated using the solution density (g cm^{-3}). Densities were measured using an SVM™ 3000 Stabinger viscometer (Anton Paar) at 298 K. The water content in the sample solution was determined to be less than 50 ppm by Karl Fischer titration.

2.2 Electrochemical Measurements

Linear sweep voltammetry (LSV, HZ-5000; Hokuto Denko) was measured by using a platinum working electrode (1.0 cm^2) with a Li foil (counter and reference electrodes, 3.75 and 0.30 cm^2, respectively) at 298 K to evaluated electrochemical window (oxidative/reductive stabilities). LSVs were performed by scanning the cell voltage from the open circuit potential toward more negative or positive potentials at a scan rate of 5.0 mV s^{-1}.

Cyclic voltammetry (CV, HZ-5000; Hokuto Denko) was conducted using a conventional three-electrode cell (**Figure 2.1a**) with graphite (thickness: 0.01 mm, diameter: 10 ϕ, 4.4 mg cm^{-2}, Piotrek) as the working electrode and a Li foil as both the counter and reference electrodes (3.75 and 0.30 cm^2, respectively) at a scan rate of 0.2 mV s^{-1} and voltage range of 0–3 V.

Charge–discharge cycling and rate property test used a CR2032 coin-type two-electrode cell (**Figure 2.1b**) with a graphite as the working electrode (thickness: 0.01 mm, diameter: 10 ϕ, 4.4 mg cm^{-2}, Piotrek) and Li foil as the counter electrode (6.15 cm^2). The cell was charged and discharged with a 0.1 C rate over a voltage range of 0–2.7 V and discharged at various C-rare (0.1–5 C, corresponding to a current density of 0.16–8.02 mA cm^{-2}).

Ionic conductivity was measured by AC impedance spectroscopy using a frequency response analyzer (SI-1260; Solartron) in the frequency range of 100 kHz to 10 mHz at 298 K. The ionic conductivity cell shows in **Figure 2.1c**. The cell constants were measured in aqueous KCl solutions (0.01, 0.1, and 1.0 mol dm^{-3}, κ = 0.00241, 0.0204, 0.171 S cm^{-1} at 298 K, respectively) as standard sample solutions. The ionic conductivity σ (S cm^{-1}) was calculated by extrapolation from a cole-cole

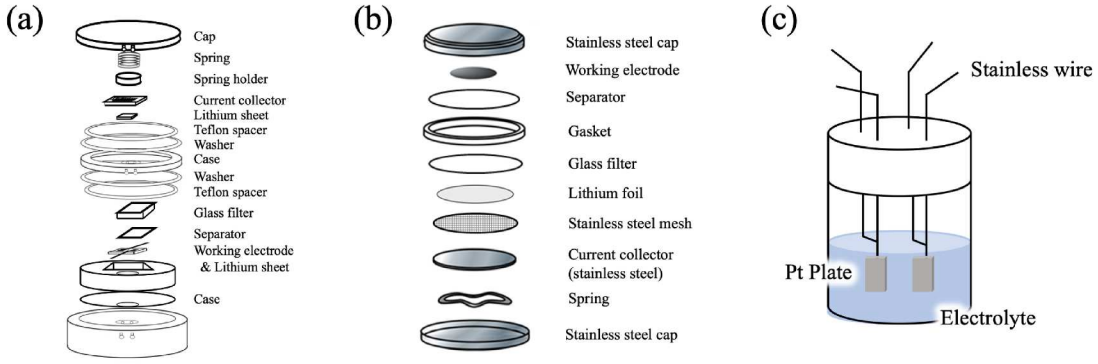

Figure 2.1 (a) Schematic diagram of three electrode metal cell and (b) diagram of the apparatus for the two electrodes coin type cell and (c) diagram of the apparatus for the ionic conductivity measurement.

plot to obtain the real axis and intercept resistances using equation (1);

$$\sigma = 1/R \times C \qquad (1).$$

Where, R and C are the resistance and capacitance, respectively.

Electrochemical impedance was measured by the AC impedance method over the frequency range from 1.0 MHz to 10 mHz with a peak-to-peak amplitude of 10 mV at 298 K. The measurements were performed for a three-electrode cell with graphite as the working electrode (thickness: 0.01 mm, diameter: 10 ϕ, 4.4 mg cm^{-2}, Piotrek) and Li foil as the counter and reference electrodes (3.75 and 0.30 cm^2, respectively) under open circuit conditions.

Flame tests were conducted by using a glass filter soaked with each electrolyte close to gas burner flame in a draft chamber.

2.3 Measurements and Analysis

Vibrational spectroscopy

Raman spectroscopy was performed using a FT-Raman/IR spectrometer (FT/IR-6100; Jasco) equipped with an Nd:YaGlaser (1064 nm), in Chapter 3 and 4. The sample solution was filled in a quartz cell, and the Raman spectrum was measured with an optical resolution of 4.0 cm^{-1} and were accumulated 1024 times in order to achieve a sufficiently high signal-to-noise ratio. Dispersion Raman spectroscopy was performed using a dispersion Raman spectrometer (NRS-3100; Jasco) equipped with a 532.2 nm wavelength laser at 298 K, in Chapter 5. The sample solution was filled in a quartz cell, and the Raman spectrum was measured with an optical resolution of 4.0 cm^{-1}.

Attenuated total reflection infrared (ATR-IR) spectroscopy was performed using FT-IR spectroscopy (FT/IR-6100; Jasco); the instrument was equipped with a KBr beam splitter and a single-reflection ATR cell. The sample solution was placed on a diamond prism with an incident angle of 45°. The optical resolution was 4.0 cm^{-1}, and the evanescent wave penetration depth, d_p, per reflection by a diamond prism was estimated using the following equation;

$$d_p = \lambda/[2\pi n_1(\sin^2\theta - n_2^2/n_1^2)^{1/2}] \qquad (2),$$

where λ is the wavelength, θ is the angle of incident (= 45°), and n_1 and n_2 are the refractive indices of the diamond prism (2.42) and sample solutions, respectively. The reflective indices of the samples at 298 K were determined using an Abbe refractometer (NAR-1 T Solid; Atago), which are listed in each Chapter. The observed absorbance A was thus corrected using the estimated d_p value, that is, A/d_p. The resulting IR and Raman spectra were deconvoluted into individual bands using a nonlinear least-squares curve-fitting based on a pseudo-Voigt function.[1-3]

$$f_V(v) = \gamma f_L(v) + (1-\gamma) f_G(v) \qquad (3),$$
$$f_L(v) = h / \{1 + (v - v_0)^2 / + \omega^2\} \qquad (4),$$
$$f_G(v) = h \exp\{-(v - v_0)^2 / \omega^2\} \qquad (5).$$

Where, $f_L(v)$ and $f_G(v)$ are Lorentzian and Gaussian functions, respectively, and v is the fraction of Lorentz components, $o < v < 1$. The h is the peak height, v is the wavenumber, and ω is the half-width at half maximum. The intensity I of a single peak is given by

$$I = \gamma I_L + (1-\gamma) I_G \qquad (6),$$

where, I_L is Lorentz component and I_G is Gauss component. In terms of Raman spectra, the integrated intensity of a single band for free solvent molecule in bulk is represented as $I_f = J_f c_f$, where J_f and c_f are the Raman scattering coefficient and the concentration, respectively. Similarly, the integrated intensity of a single band for bound solvent molecule in the Li-ion coordination sphere is represented as $I_b = J_b c_b$. Using mass balance equations; $c_f = c_T - c_b = c_T - nc_{Li}$, where c_T, c_{Li}, and n represent the total solvent and Li-ion concentrations and the number of solvent molecule bound to Li-ion, respectively. The following equation can be obtained;

$$I_f/c_T = -nJ_f (c_{Li}/c_T) + J_f \qquad (7),$$

plots of I_f/c_T against c_{Li}/c_T give a straight line with the slope α (= $-nJ_f$) and intercept β (= J_f), and the n value is thus obtained from $n = -\alpha/\beta$. Peak deconvolution in the IR spectra was similar to the Raman spectra, and the integrated intensity of the single band is given as $I = \varepsilon c d_p$, where ε is the molar absorption coefficient.

High-energy X-ray total scattering

High energy X-ray total scattering (HEXTS) measurements were conducted at 298 K using a high-energy X-ray diffraction apparatus (BL04B2 beamline, SPring-8, JASRI, Japan).[4] Monochromatized 61.4 keV X-rays were obtained using a Si(220) monochromator. The observed X-ray scattering intensities were corrected for absorption, polarization, and incoherent scattering to determine coherent scattering intensities, $I_{coh}(q)$.[5-7] The experimental X-ray structure factor per stoichiometric volume, $S^{exp}(q)$, was obtained using the following equation; (8). The $I_{coh}(q)$ is the coherent scattering intensity obtained from the corrected X-ray scattering

intensity, n_i and $f_i(q)$ correspond to the number and atomic scattering factor of atom i, respectively, and N is the total number of atoms in the stoichiometric volume. The radial distribution function, $G^{exp}(r)$ is obtained using the inverse Fourier transform of the $S^{exp}(q)$ as follows; (9), where ρ_0 corresponds to the number density of atoms, q_{max} corresponds to the maximum value of q (25 $Å^{-1}$), and $W(q)$, (10) corresponds to the Lorch window function.[8-10]

In situ SEIRAS spectroscopy

In situ surface enhanced infrared absorption spectroscopy (SEIRAS) was performed using a Nicolet iS50 FTIR (Thermo Fischer Scientific) spectrometer equipped with a Mercury Cadmium Telluride detector and with an optical resolution of 4 cm^{-1}. The optical path was fully replaced with N_2 gas. A Pt-deposited Si prism (3.14 cm^2) was mounted in a spectro-electrochemical three-electrode cell with a Li foil (counter and reference electrodes, 1.5 and 1.5 cm^2, respectively, **Figure 2.2**). The surface of the Si prisms was repeatedly polished with 1 μm polycrystalline diamond abrasive and cleaned with pure water. After polishing, the smoothed surface was immersed in a 40% NH_4F solutions of etching agent for 1 minute to remove the surface oxide film, and then hydrogen-terminated. The surface was immersed in 0.5 mM $PdCl_2$ + 1% HF solutions for 5 minutes to adsorb Pd on the surface. Then, I prepared an electroless Pt plating solution containing 0.01 mol dm^{-3} $[Pt(NH_3)_6]OH_4$ + pH buffer: 1.0 mol dm^{-3} NH_3 (28%) + reducing agent 0.06 mol dm^{-3} hydrazine. The plated Si prisms (**Figure 2.3**) were fabricated by plating in a high-temperature water

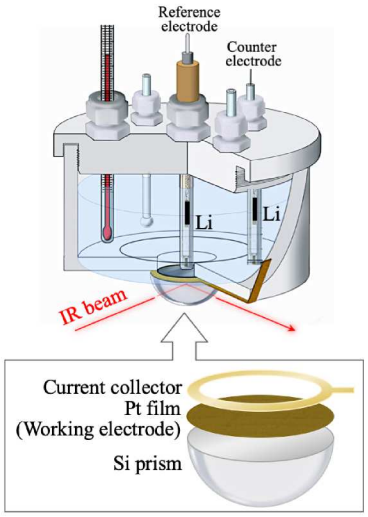

Figure 2.2 Schematic of the spectroelectrochemical cell for *in situ* SEIRAS cell.

bath at 320 K for about 7 to 12 min. The cell was set in the spectrometer at an incident beam angle of 67° to

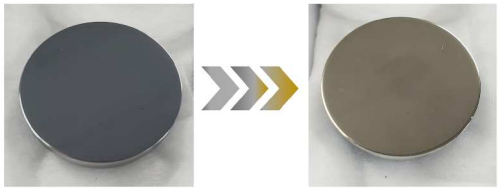

Figure 2.3 The images of the Pt-deposited Si prism.

record SEIRA spectra during LSV measurements (HSV-100, Hokuto Denko). All spectra were presented in the form of absorbance according to $\log(I_0/I)$, where I_0 and I are the reference spectrum (measured at 3.0 V vs Li/Li^+) and the *in situ* spectrum at a given potential, respectively.

MD simulations

An all-atom molecular dynamics (MD) simulation was conducted using the GROMACS 2018.8 program, applying the *NTP* ensemble condition (298 K and 1 atm) in a cubic cell.[11, 8] The composition (i.e., number of LiFSA salts and solvent molecules) in simulation box and the box length at equilibrium condition are listed in each chapter. The total simulation time was 15.0 ns. Data collected at 0.1 ps intervals from the last 500 ps were analyzed to determine X-ray weighted structure factors and radial distribution functions ($S^{MD}(q)$ and $G^{MD}(r)$, respectively). The resulting density values were in good agreement with the corresponding experimental density values (see each Chapter Table). The CLaP and OPLS-AA force fields, including intermolecular Lennard–Jones (LJ) and Coulombic interactions and intramolecular interactions (i.e., bond stretching, angle bending, and torsion of dihedral angles) were used for FSA,[12] TFEP,[13-14] AN[15-16] and TFEAc,[17, 16] respectively. The LJ parameter for Li ions (see the Li salt/carbonate solvent system[18]) was used. In the partial charges (q^+ and q^-) for Li^+ and FSA^-, we assumed the effective partial charge due to ion-solvation to modify them from the original values. The modified values are shown in **Figure A3.1** (TFEP, AN[19], and LiFSA[12] in Chapter 3) and **Figure A6.1** (LiFSA[12] and TFEAc[17, 16] in Chapter 6). The values of TFEP were calculated based on ChelpG method (MP2/cc-pVTZ(-f) calculation).[20]

The $S^{MD}(q)$ functions were calculated using the trajectory from the MD simulations as follows; (11), where r', the limit of the integration, was set to 25 Å, n_i and N are the number of i atoms and the total number of atoms in the simulation box, respectively, and $g_{ij}^{MD}(r)$ is the atom–atom pair correlation function between atoms i and j. $G^{MD}(r)$ was obtained from the calculated $S^{MD}(q)$ using an inverse Fourier transform.

DFT calculations

Density functional theory (DFT) calculations were performed using Gaussian 09 software.[21] The geometry

$$S^{\exp}(q) = \frac{\frac{I_{\mathrm{coh}}(q)}{N} - \sum n_i f_i(q)^2}{\left\{\sum n_i f_i(q)\right\}^2} + 1 \tag{8}$$

$$G^{\exp}(r) - 1 = \frac{1}{2\pi^2 r \rho_0} \int_0^{q_{\max}} q\{S^{\exp}(q) - 1\} \sin(qr) W(q) \mathrm{d}q \tag{9}$$

$$W(q) = \frac{\sin(\pi\, q/qmax)}{\pi\, q/qmax} \tag{10}$$

$$S^{\mathrm{MD}}(q) = \begin{cases} \dfrac{\sum_i \sum_j \left\{\dfrac{n_i(n_j - 1) f_i(q) f_j(q)}{N(N-1)}\right\}}{\left\{\sum_k \left(\dfrac{n_k f_k(q)}{N}\right)\right\}^2} \displaystyle\int_0^{r'} 4\pi r^2 \rho_0 \left\{g_{ij}^{\mathrm{MD}}(r) - 1\right\} \frac{\sin qr}{qr} \mathrm{d}r + 1 \ (i = j) \\ \dfrac{\sum_i \sum_j \left\{\dfrac{2 n_i n_j f_i(q) f_j(q)}{N^2}\right\}}{\left\{\sum_k \dfrac{(n_k f_k(q)}{N}\right\}^2} \displaystyle\int_0^{r'} 4\pi r^2 \rho_0 \left\{g_{ij}^{\mathrm{MD}}(r) - 1\right\} \frac{\sin qr}{qr} \mathrm{d}r + 1 \ (i \neq j) \end{cases} \tag{11}$$

of Li-ion complexes were fully optimized at the B3LYP/6-311** level in order to evaluate highest unoccupied molecular orbital (HOMO) energy (E_{HOMO}) and lowest unoccupied molecular orbital (LUMO) energy (E_{LUMO}) and obtain their theoretical Raman bands[22-23] in Chapter 4 and 5. The binding energy ΔE_{bind} was calculated as the SCF energy difference between the Li-X (= solvent molecule (1:1) complex and its individual components (Li^+ and X) according to $\Delta E_{\mathrm{bind}} = E_{\mathrm{SCF}}$ (complex) − E_{SCF} (Li^+) − E_{SCF} (X) and then corrected by the basis set superposition error using the counterpoise method[24] in **Figure A5.1 (**Chapter 5).

2.4 References

(1) Fujii, K.; Fujimori, T.; Takamuku, T.; Kanzaki, R.; Umebayashi, Y.; Ishiguro, S. Conformational Equilibrium of Bis(trifluoromethanesulfonyl) Imide Anion of a Room-Temperature Ionic Liquid: Raman Spectroscopic Study and DFT Calculations. *J. Phys. Chem. B* **2006,** *110*, 8179-8183.

(2) Fujii, K.; Kumai, T.; Takamuku, T.; Umebayashi, Y.; Ishiguro, S. Liquid structure and preferential solvation of metal ions in solvent mixtures of *N*,*N*-dimethylformamide and *N*-methylformamide. *J. Phys. Chem. A* **2006,** *110*, 1798-1804.

(3) Umebayashi, Y.; Matsumoto, K.; Watanabe, M.; Katoh, K.; Ishiguro, S. Indivisual Solvation Numbers around the Nickel(II) Ion in an *N*,*N*-Dimethylformamide and *N*,*N*-Dimethylacetamide Mixture Determinded by Raman Spectrophotometry. *Analytical Sciences* **2001,** *17*, 323-326.

(4) Kohara, S.; Suzuya, K.; Kashihara, Y.; Matsumoto, N.; Umesaki, N.; Sakai, I. A Horizontal Two-axis Diffractometer for High-energy X-ray Diffraction Using Synchrotron Radiation on Bending Magnet Beamline BL04B2 at SPring-8. *Nucl. Instrum. Meth. A* **2001,** *467-468*, 1030-1033.

(5) Cromer, D. T. Compton Scattering Factors for Aspherical Free Atoms. *J. Chem. Phys.* **1969,** *50*, 4857-4859.

(6) Hubbell, J. H.; Veigele, W. J.; Briggs, E. A.; Brown, R. T.; Cromer, D. T.; Howerton, R. J. Atomic form factors, incoherent scattering functions, and photon scattering cross sections. *J. Phys. Chem. Ref. Data* **1975,** *4*, 471.

(7) Sakai, S. *KEK Report 90-16*, National Laboratory for High Energy Physics: Tsukuba, Japan, 1990.

(8) Hirosawa, K.; Fujii, K.; Hashimoto, K.; Shibayama, M. Solvated Structure of Cellulose in a Phosphonate-Based Ionic Liquid. *Macromolecules* **2017,** *50*, 6509-6517.

(9) Kamiyama, Y.; Shibata, M.; Kanzaki, R.; Fujii, K. Lithium-ion coordination-induced conformational change of PEG chains in ionic-liquid-based electrolytes. *Phys. Chem. Chem. Phys.* **2020,** *22*, 5561-5567.

(10) Shibata, M.; Sawayama, S.; Osugi, M.; Fujii, K. Structural aspect on "Salting-in" mechanism of PEG chains into a phosphonium-based ionic liquid using lithium salt. *J. Mol. Liq.* **2022,** *366*, 120255.

(11) Fujii, K.; Ueki, T.; Hashimoto, K.; Kobayashi, Y.; Kitazawa, Y.; Hirosawa, K.; Matsugami, M.; Ohara, K.; Watanabe, M.; Shibayama, M. Microscopic Structure of Solvated Poly(benzyl methacrylate) in an Imidazolium-

Based Ionic Liquid: High-Energy X-ray Total Scattering and All-Atom MD Simulation Study. *Macromolecules* **2017,** *50*, 4780-4786.
(12) Shimizu, K.; Almantariotis, D.; Gomes, M. F. C.; Pádua, A. A. H.; Lopes, J. N. C. Molecular Force Field for Ionic Liquids V: Hydroxyethylimidazolium, Dimethoxy-2- Methylimidazolium, and Fluoroalkylimidazolium Cations and Bis(Fluorosulfonyl)Amide, Perfluoroalkanesulfonylamide, and Fluoroalkylfluorophosphate Anions. *J. Phys. Chem. B* **2010,** *114*, 3592–3600.
(13) Cui, S.; de Almeida, V. F.; Khomami, B. Molecular dynamics simulations of tri-*n*-butyl-phosphate/*n*-dodecane mixture: hermophysical properties and molecular structure. *J. Phys. Chem. B* **2014,** *118*, 10750-10760.
(14) Duarte, P.; Silva, M.; Rodrigues, D.; Morgado, P.; Martins, L. F.; Filipe, E. J. Liquid mixtures involving hydrogenated and fluorinated chains: (p, ρ, T, x) surface of (ethanol + 2,2,2-trifluoroethanol), experimental and simulation. *J. Phys. Chem. B* **2013,** *117*, 9709-9717.
(15) Lopes, J. N. A. C.; Gomes, M. F. C.; Pádua, A. A. H. Nonpolar, Polar, and Associating Solutes in Ionic Liquids. *J. Phys. Chem. B* **2006,** *110*, 16816-16818.
(16) Price, M. L. P.; Ostrovsky, D.; Jorgensen, W. L. Gas-Phase and Liquid-State Properties of Esters, Nitriles, and Nitro Compounds with the OPLS-AA Force Field. *J Comput Chem* **2001,** *22*, 1340–1352.
(17) Jorgensen, W. L.; Maxwell, D. S.; Tirado-Rives, J. Development and Testing of the OPLS All-Atom Force Field on Conformational Energetics and Properties of Organic Liquids. *J. Am. Chem. Soc.* **1996,** *118*, 11225-11236.
(18) Soetens, J.-C.; Millot, C.; Maigret, B. Molecular Dynamics Simulation of $Li^+BF_4^-$ in Ethylene Carbonate, Propylene Carbonate, and Dimethyl Carbonate Solvents. *J. Phys. Chem. A* **1998,** *102*, 1056-1061.
(19) Nikitin, A. M.; Lyubartsev, A. P. New six-site acetonitrile model for simulations of liquid acetonitrile and its aqueous mixtures. *J Comput Chem* **2007,** *28*, 2020-2026.
(20) Sogawa, M.; Sawayama, S.; Han, J.; Satou, C.; Ohara, K.; Matsugami, M.; Mimura, H.; Morita, M.; Fujii, K. Role of Solvent Size in Ordered Ionic Structure Formation in Concentrated Electrolytes for Lithium-Ion Batteries. *J. Phys. Chem. C* **2019,** *123*, 8699-8708.
(21) Frisch, M. J.; Trucks, G. W.; Schlegel, H. B.; Scuseria, G. E.; Robb, M. A.; Cheeseman, J. R.; Scalmani, G.; Barone, V.; Mennucci, B.; Petersson, G. A., etc. . Gaussian 09; Gaussian, Inc.:. *Wallingford, CT.* **2009**.
(22) Fujii, K.; Wakamatsu, H.; Todorov, Y.; Yoshimoto, N.; Morita, M. Structural and Electrochemical Properties of Li Ion Solvation Complexes in the Salt-Concentrated Electrolytes Using an Aprotic Donor Solvent, *N*,*N*-Dimethylformamide. *J. Phys. Chem. C* **2016,** *120*, 17196-17204.
(23) Sawayama, S.; Morinaga, A.; Mimura, H.; Morita, M.; Katayama, Y.; Fujii, K. Fluorophosphate-Based Nonflammable Concentrated Electrolytes with a Designed Lithium-Ion-Ordered Structure: Relationship between the Bulk Electrolyte and Electrode Interface Structures. *ACS Appl. Mater. Interfaces* **2021,** *13*, 6201-6207.
(24) Asada, M.; Fujimori, T.; Fujii, K.; Kanzaki, R.; Umebayashi, Y.; Ishiguro, S. Solvation structure of magnesium, zinc, and alkaline earth metal ions in *N*,*N*-dimethylformamide, *N*,*N*-dimethylacetamide, and their mixtures studied by means of Raman spectroscopy and DFT calculations –Ionic size and electronic effects on steric congestion–. *J. Raman Spectrosc.* **2007,** *38*, 417-426.

Chapter 3

Fluorinated Alkyl-Phosphate-Based Electrolytes with Controlled Lithium-Ion Coordination Structure

3.1 Introduction

In the nonflammable organic solvents category, Xu et al. reported that tris(2,2,2-trifluoroethyl) phosphate (TFEP) can be applied as a nonflammable additive to carbonate solvent-based LIB electrolytes;[1-2] they reported that an optimized TFEP in carbonate-based electrolyte system led to sufficient LIB performance: 15%–20% TFEP in 1.0 mol kg^{-1} $LiPF_6$/EC+EMC (1:1 by weight). We have reported that nonflammable electrolytes based on $LiPF_6$ and cyclic/linear carbonate mixtures containing TFEP as a nonflammable additive can work well in both solution and polymer gel-based rechargeable LIBs.[3] Furthermore, we found that the nonflammable electrolyte systems using TFEP as the main solvent, 0.5 mol dm^{-3} Li salt/TFEP containing EC, showed great thermal stability up to 673 K.[4-5] In a previous study, we reported on the structural properties of the Li bis(trifluoromethanesulfonyl)amide (LiTFSA) salt in a TFEP electrolyte solution at a molecular level:[6] (1) TFEP can be categorized as an aprotic solvent with weak electron-pair donating ability showing weak ion-solvent interactions, (2) the large molecular size of TFEP causes a steric repulsion among the TFEP molecules in the Li-ion solvation sphere, and thus (3) Li-ions prefer to form ion-pair complexes with the TFSA anion, even in low Li salt concentrations (c_{Li}), to reduce the steric repulsion among the solvated TFEP molecules.

In a conventional LIB employing a graphite electrode, carbonate organic electrolytes are required to achieve stability and reversibility. Here, we note that the FSA anion plays a key role, together with carbonate solvents in the LIB electrode reaction.[7-9] Ishikawa et al. reported that FSA-based IL electrolytes containing Li-ions exhibit excellent electrochemical performances; i.e., Li-ion insertion into graphite occurs in FSA-based ILs without carbonate components.[10-12] However, in TFSA-based IL electrolytes, no electrode reactions are observed in such carbonate-free systems. They proposed a model of the electrode reaction mechanism focusing on the electrode/electrolyte interface, which is not a conventional SEI, in the LiFSA/[C_2mIm][FSA] electrolyte system (C_2mIm: 1-ethyl-3-methylimidazolium cation) as follows:[13] (1) in the neat IL, the C_2mIm cations locate at the primary layer of the graphite anode during charging. (2) When the Li salt is added to the IL, the primary layer is occupied by Li-ions rather than the C_2mIm cations, and the secondary layer is then filled with FSA anions binding to the Li-ions outside to form a compact double-layer structure. (3) This $Li^+\cdots FSA^-$-based double layer may prevent decomposition of the organic C_2mIm cations, leading to stable Li-ion insertion into the graphite. In this model, the weak solvation of Li-ions with FSA is an essential factor; that is, weaker $Li^+\cdots FSA^-$ interactions facilitate FSA desolvation from the first solvation sphere, followed by the directly Li-ion-located primary layer on the graphite. This mechanism could be applied to the TFSA-based electrolyte system due to a stronger $Li^+\cdots TFSA^-$ interaction in the Li-ion solvation complexes hindering TFSA desolvation.

In this work, by exploiting the inherent FSA-coordination characteristics, I aimed to develop "Li^+ coordination-controlled organic electrolytes" to enable the LIB electrode reaction in a carbonate-free system. I selected TFEP as self-extinguishing properties, resulting in non-flammable organic electrolytes.[1-2, 14] To allow Li-ion insertion into a graphite electrode for LIBs, I propose Li-ion solvation-controlled electrolytes using an TFEP and an LiFSA salt, which has FSA-coordination characteristics at the molecular levels.

3.2 Experimental

3.2.1 *Materials*

I prepared ternary LiFSA/TFEP+AN solutions at fixed c_{Li} = 1.0 mol dm^{-3} and varied the ratio of Li salt to AN (by mol.), i.e., Li:AN = 1:0, 1:1, and 1:2 (termed the 1:0, 1:1, and 1:2 solutions). The 1:0 solution corresponds to the binary LiFSA/TFEP solution. Sample electrolyte solutions were prepared by weighing the solvent and Li salt to the required molar ratio (Li salt:solvent) in an Ar-

filled glovebox; the corresponding molarities (Li salt concentration, c_{Li}) were then calculated using the solution density (g cm^{-3}) are listed in **Table A3.1** (in **Appendix**). The composition (i.e., number of LiFSA salts and solvent molecules) of the MD simulation box is listed in **Table A3.2**. The resulting density values were in good agreement with the corresponding experimental density values.

3.3 Results and Discussion

3.3.1 *Li-ion complexes in neat TFEP*

Figure 3.1a shows IR spectra of LiFSA/TFEP solutions with different Li salt concentrations (c_{Li}), from 700 to 1000 cm^{-1}. The broad band at approximately 880–910 cm^{-1} for the c_{Li} = 0 mol dm^{-3} solution (neat TFEP, blue line), which is assigned to the O–P–O asymmetric stretching mode of TFEP in the bulk[15, 6] (termed free TFEP), gradually decreased in intensity as c_{Li} increased. Conversely, a new band appeared at a higher frequency (approximately 903.5 cm^{-1}, shown by a red arrow in the figure) and intensified as c_{Li} increased. It was established in our previous study (IR spectroscopy and DFT calculations)[6] that the 903.5 cm^{-1} band is assigned to the TFEP bound to the Li-ion (termed bound TFEP). I observed a clear isosbestic point at 907.0 cm^{-1}, suggesting that the TFEP molecules coexisted as two species, i.e., free and bound TFEP, in the c_{Li} solutions examined herein. In the 700–770 cm^{-1} range, two bands centered at 745.3 and 758.2 cm^{-1} increased in intensity as c_{Li} increased. These bands originated from the FSA component (the former corresponding to "free FSA" in the bulk and the atter to "bound FSA" in the first coordination sphere of the Li-ion); this will be discussed in detail in a later section.

To determine the solvation number of TFEP molecules around Li-ions, I performed a least-squares curve-fitting analysis of the observed IR spectra (800–1000 cm^{-1}) to deconvolute the spectrum into individual bands for each component. In the neat TFEP system (c_{Li} = 0 mol dm^{-3}), the IR spectrum from 850 to 950 cm^{-1}, which is assigned to the free TFEP [ν_{as}(O–P–O)] mentioned above, was significantly distorted. According to a previous IR and DFT study,[6] the distorted broad spectrum can be represented by two components, as TFEP has complex geometry and molecular flexibility. In this study, the IR spectrum in this range was deconvoluted using two bands of free TFEP; the fitting parameters (half-width at half-maximum and Gauss/Lorentz ratio on pseudo-Voigt functions) and the ratio of the band height between the two bands were fixed for all c_{Li} during the current fitting analysis. A typical result for c_{Li} = 1.0 mol dm^{-3} is shown in **Figure 3.1b**. The IR spectrum could be deconvoluted into two free TFEP components (blue line: 887.0 and 907.2 cm^{-1}) and one bound TFEP component (red line: 903.5 cm^{-1}), which was also applied to the IR spectra for all c_{Li}. I estimated the solvation number for the Li-ions (n_{TFEP}) by analyzing the sum of the integrated intensities for the 887.0 and 907.2 cm^{-1} bands (i.e., I_f = I_{887} + I_{907}) as a function of c_{Li}. **Figure 3.2** shows a plot of I_f/c_T vs. c_{Li}/c_T based on the equation (1) given in the Experimental Section. For every c_{Li} investigated here, the plots fall on a straight line with slope $-n\varepsilon_f$ and intercept ε_f such that n_{TFEP} = 2.2 ± 0.3 according to n = −slope/intercept. This indicates that Li-ions are solvated with two TFEP molecules in solution, which is similar to the analogous LiTFSA/TFEP electrolyte system described in the previous study (n_{TFEP} = 2.0 ± 0.1).[6] Here, the resulting n_{TFEP} is significantly below the corresponding values reported for conventional aprotic solvents, i.e., a tetrahedral [Li(solvent)$_4$]$^+$ complex with n = 4.[16-17] I predicted that the Li-ions coordinate with both the TFEP and FSA (counter-anion) components to form [Li(TFEP)$_2$(FSA)$_m$] ion-pair complexes. Thus, the current LiFSA/TFEP system was subjected to further structural investigation using IR spectroscopy, focusing especially on FSA coordination in the Li-ion complexes.

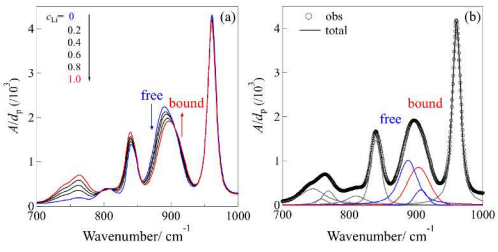

Figure 3.1 (a) IR spectra of LiFSA/TFEP solutions with different c_{Li}. (b) A typical curve-fitting result for the c_{Li} = 1.0 mol dm^{-3} solution.

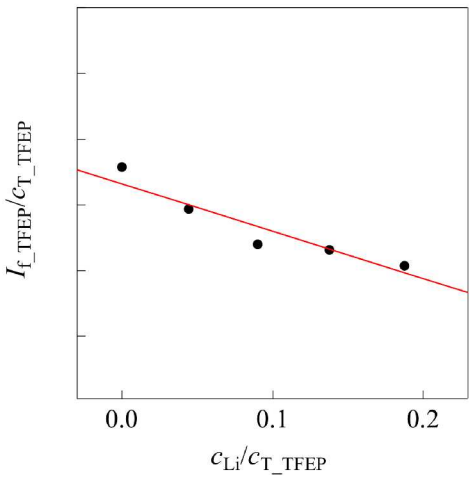

Figure 3.2 I_{f_TFEP}/c_{T_TFEP} vs. c_{Li}/c_{T_TFEP} plot using the deconvoluted bands (I_{f_TFEP} = I_{887} + I_{907}) of the free TFEP.

Figure 3.3a shows IR spectra for LiFSA/TFEP solutions with varying c_{Li} from 700 to 800 cm^{-1}; these bands are assigned to the S-N-S and S-F symmetric stretching vibrations of the FSA component. As shown in the figure, two bands at around 745.3 and 758.2 cm^{-1} intensified as c_{Li} increased. To assign these to potential FSA components, I also performed IR measurements for the TFEP solutions containing 1-ethyl-3-methylimidazolium FSA ionic liquid ([C_2mIm][FSA]) as a model system; I assumed herein that [C_2mIm][FSA] dissolved in TFEP is completely dissociated to C_2mIm^+ and FSA^- ions owing to the larger ionic size of the delocalized C_2mIm^+ cation, leading to "free-FSA" detection from the present IR spectra. The result is shown in the Supporting Information. The IR spectrum for a 1.0 mol dm^{-3} [C_2mIm][FSA]/TFEP solution contained two bands at 745.3 and 758.2 cm^{-1}. Based on this observation, it is feasible that the spectrum originating from free FSA consisted of two bands in this frequency range, which might be due to the molecular flexibility of FSA allowing formation of various FSA conformers in the liquid state.[18-20] Considering this model system, I conducted a band deconvolution analysis for the LiFSA/TFEP system as follows: (1) With regard to the free-FSA component, I fixed the fitting parameters (frequency position, width, ratio of heights, half-width at half-maximum, and Gauss/Lorentz ratio on pseudo-Voigt functions) among the two bands (free 1 and free 2) and (2) added a new band as a bound-FSA component at the higher frequency side. A typical result (c_{Li} = 1.0 mol dm^{-3}) is shown in **Figure 3.3b**. The experimental spectrum was successfully reproduced using the three bands; two of these (blue line: 745.3 and 758.2 cm^{-1}) corresponded to free FSA with one major band (red line: 768.5 cm^{-1}) corresponding to bound FSA. **Figure 3.4** shows the concentration ratio of bound FSA to the total FSA (c_{b_FSA}/c_{T_FSA}) vs. c_{Li}, where c_{T_FSA} is the total FSA concentration in the solutions (i.e., $c_{T\_FSA} = c_{f\_FSA} + c_{b\_FSA}$). A detailed procedure for calculating c_{f_FSA} and c_{b_FSA} from the IR data is given in the Supporting Information. The c_{b_FSA}/c_{T_FSA} value represents the proportion of the ion-pair complex, $Li^+\cdots FSA^-$, which

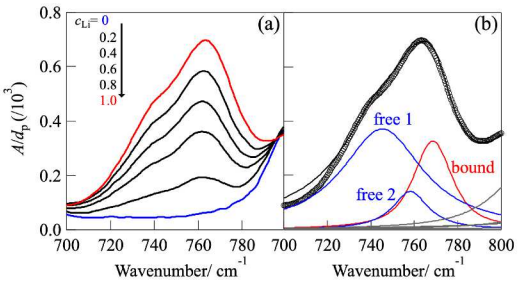

Figure 3.3 (a) IR spectra for LiFSA/TFEP solutions with varying c_{Li}. (b) A typical curve-fitting result for the c_{Li} = 1.0 mol dm^{-3} solution.

was estimated as ~0.8, irrespective of the c_{Li} examined here. This result suggested that approximately 80% of the total FSA anions coordinate with the Li-ions to form $Li^+\cdots FSA^-$ (1:1) ion pairs, even in dilute c_{Li} solutions below 1.0 mol dm^{-3}. Therefore, I concluded that in the LiFSA/TFEP solutions, Li-ions exist mainly as [Li(TFEP)$_2$(FSA)] complexes as the major species at equilibrium; these coexist with ion-pair-free minor species (20%). This result is consistent with that of the analogous LiTFSA/TFEP electrolyte described in our previous study;[6] (1) the Li-ions are coordinated with both TFEP (solvent) and TFSA (counter-anion) to form [Li(TFEP)$_2$(TFSA)] complexes as a major species (80%) in solution, which coexist with ion-pair-free Li-ions (minor species); (2) in the ion-pair complexes, the coordinated TFSA anion acts as a bidentate ligand (bi-TFSA) with two oxygen atoms per TFSA molecule. Consequently, the Li-ions are tetrahedrally coordinated with four oxygen atoms (i.e., two from bi-TFSA and two from the two solvated TFEP molecules). It is therefore feasible that in the current LiFSA/TFEP system, the ion-pair complexes comprise one bidentate FSA and two monodentate TFEP species to form [Li(TFEP)$_2$(bi-FSA)].

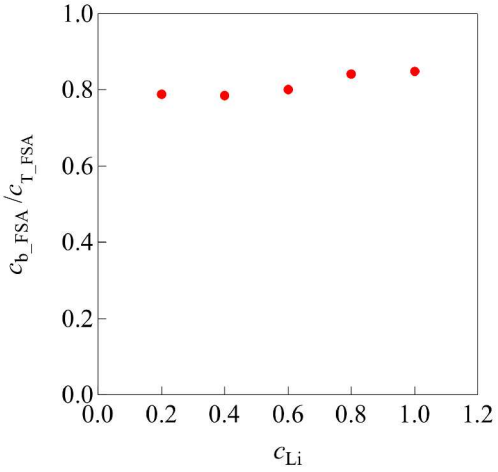

Figure 3.4 Concentration ratio of bound FSA to the total FSA (free + bound) in LiFSA/TFEP solutions with varying c_{Li}.

3.3.2 *Structural changes in the Li-ion complexes on adding AN*

To structurally control the ion-pair complexes formed in bulky TFEP solvent, a neutral ligand was added to the LiFSA/TFEP electrolytes. I selected acetonitrile (AN) as a neutral ligand additive for this system; this was because (1) AN is a small molecule compared with bulky TFEP and (2) the electron-pair donating ability, i.e., Gutman donor number (D_N) of AN is close to that of TFEP (AN: D_N = 14.1,[21] TFEP: D_N = 12.9[6]), which

emphasizes the solvation steric effect on the Li-ion complex structure without a solvent D_N effect. **Figure 3.5** shows IR spectra from 700–800 cm^{-1} (originating from the FSA anion) for c_{Li} = 1.0 mol dm^{-3} LiFSA/TFEP solutions with added AN [Li:AN (by mol.) = 1:0 (black), 1:1 (red), and 1:2 (green)]. The peak position at 768.5 cm^{-1} for the c_{Li} = 1.0 mol dm^{-3} solution (Li:AN = 1:0), which is attributed to the bound-FSA species (clearly seen by comparing with the IR spectrum of the free-FSA species: TFEP solution containing [C_2mIm][FSA], dashed gray line shown in **Figure 3.5**), gradually shifted to lower frequencies as AN was added, reaching 758.5 cm^{-1} for the Li:AN = 1:2 solution. Their peak deconvolution results are shown in **Figure A3.1**. As with the neat TFEP system, the IR spectra exhibited two free-FSA bands and one bound-FSA band; later, the peak positions were 768.5 cm^{-1} (Li:AN = 1:0), 767.0 cm^{-1} (1:1), and 764.9 cm^{-1} (1:2). As discussed above, in the LiFSA/TFEP solutions (without AN), the FSA anions coordinate to Li-ions in a bidentate manner, forming [Li(TFEP)$_2$(bi-FSA)] complexes to give a band at 768.5 cm^{-1}. Thus, the peak shift for bound FSA might suggest a structural change in the Li-ion complexes; i.e., the bi-FSA changed to another coordination mode [monodentate FSA (mono-FSA)] after AN addition to the LiFSA/TFEP solutions. Giffin et al. reported that in ionic liquid electrolytes, an amide-type anion exhibited different frequency positions due to its coordination mode around metal ions; in Mg(TFSA)$_2$/IL solutions, the frequency of the monodentate TFSA component was lower than that of bidentate TFSA according to Raman spectroscopy and DFT calculations.[22] This could be applied to the analogous FSA-based electrolyte system

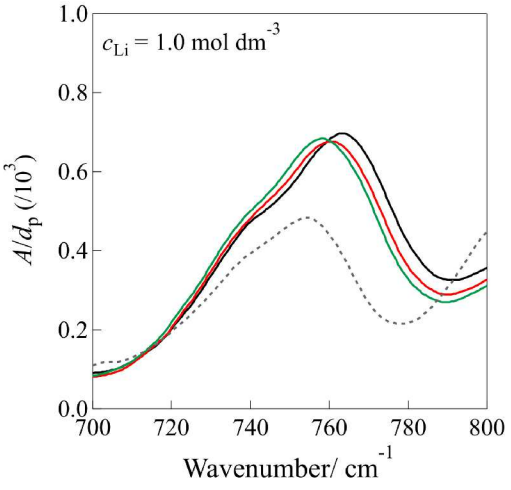

Figure 3.5 IR spectra for the LiFSA/TFEP solutions (c_{Li} = 1.0 mol dm^{-3}) with added AN [Li:AN (by mol.) = 1:0 (black), 1:1 (red), and 1:2 (green)], together with the TFEP solution containing 1.0 mol dm^{-3} [C_2mIm][FSA] (dashed gray line).

in this work, and I therefore proposed that the FSA-coordination structure could be controlled by adding a small amount of neutral ligand (in this case, AN), leading to Li^+···mono-FSA^- ion pairs in solution. To confirm "AN coordination" in the structurally altered Li-ion complexes, I recorded FT-Raman spectra from 2240–2300 cm^{-1} (N≡C symmetric stretching vibration of AN),[23-24] which are sensitive to metal ion···AN interactions, for LiFSA/TFEP solutions with varying AN contents (**Figure 3.6**). **Figure 3.6a and b** show Raman spectra for 1.0 M LiFSA/TFEP solution with Li:AN = 1:1 and 1:2 (by mol.), respectively, and for those without LiFSA salt (i.e., solvent mixtures of TFEP and AN). For both systems, the intensity of the free AN band at around 2265 cm^{-1} clearly weakened by adding Li salt, and a new band (bound AN) appeared at the higher frequency side (~2280 cm^{-1}). A fitting analysis (band deconvolution) was performed for the observed Raman spectra, shown in **Figure 3.6c** and d (Li:AN = 1:1 and 1:2, respectively). The Raman spectra were successfully represented by four components: two free (2261.0 and 2265.0 cm^{-1}, blue lines) and two bound (2277.5 and 2285.0 cm^{-1}, red lines) bands, and the fitting results (numbers of free/bound bands and their frequencies) were consistent with those reported for the other AN-based electrolyte system.[23-24] Based on the deconvoluted free bands, I estimated the individual solvation numbers of AN molecules (n_{AN}) around Li-ions in the present LiFSA/TFEP+AN electrolytes. Using the integrated intensities of the two free bands, I_f (= I_{2261} + I_{2265}), I could calculate the concentration of the free AN (c_{f_AN}) using the following relation: $I_f = J_{f\_AN}\, c_{f\_AN}$, where J_{f_AN} is the Raman scattering coefficient. In this work, J_{f_AN} was determined sepa- rately from the additional Raman experiments for the mixed solutions of TFEP and AN; this is described in detail in the **Appendix** (**Figure A3.4**). The n_{AN} (= $[c_{T\_AN} - (I_{f\_AN}/J_{f\_AN})]/c_{Li}$) values were 0.19 and 0.38 for Li:AN = 1:1 and 1:2 solutions, respectively.

3.3.3 *HEXTS experiments and MD simulations*

Figure 3.7 shows X-ray redial distribution functions obtained from HEXTS experiments and MD simulations [$G^{exp}(r)$ and $G^{MD}(r)$, respectively] performed on the 1.0 mol dm^{-3} LiFSA/TFEP solutions (a) without AN (Li:AN=1:0) and (b) with AN (Li:AN=1:2). The G(r) functions were calculated by Fourier transformation of the corresponding structure factors, $S(q)$s (**Figure A3.5**) and shown as an r-weighted difference form, $r^2[G(r) - 1]$ in the figure. It was clear that the $G^{MD}(r)$ functions successfully reproduced the $G^{exp}(r)$ functions from the short and long r range for both Li:AN = 1:0 and 1:2 systems. To discuss the detailed coordination structure in the Li-ion solvated complexes, I evaluated the atom

–atom pair correlation functions, $g^{MD}(r)$, particularly X–Y focusing on the local-scale structure; i.e., the Li^+–O_{tfep}, Li^+–O_{fsa}, and Li^+–N_{an} correlations for the Li^+–TFEP, Li^+–FSA, and Li^+–AN interactions, respectively. The resulting $g^{MD}_{Li\text{-}Otfep}(r)$, $g^{MD}_{Li\text{-}Ofsa}(r)$, and $g^{MD}_{Li\text{-}Nan}(r)$ are shown in **Figure A3.6**, together with the average coordination number $N_{X–Y}(r)$, calculated by integrating the corresponding $g^{MD}_{X\text{-}Y}(r)$ up to a given r. In the LiFSA/TFEP (Li:AN = 1:0) system, a major peak appeared at 1.98 Å in both $g^{MD}_{Li\text{-}Otfep}(r)$, $g^{MD}_{Li\text{-}Ofsa}(r)$. The $N_{Li–O}(r)$ values for the Li^+–O_{tfep} and Li^+–O_{fsa} interactions were estimated to be ~2.1 and ~2.5 (plateau in the $N_{X–Y}(r)$ at r = 2.5–3.0 Å), respectively, indicating that the Li-ions are coordinated with four O atoms including two of the monodentate-coordinated TFEP and two of the bidentate-coordinated FSA. This result was consistent with the result from the current IR study as described above: i.e., the n_{TFEP} and n_{FSA} are ~2.2 and ~0.8 to form $[Li(TFEP)_2(bi\text{-}FSA)_1]$ complexes as the major species. The $N_{Li–Otfep}(r)$ and The $N_{Li–Ofsa}(r)$ decreased by adding AN to ~0.60 (Li^+–TFEP interactions) and ~1.2 (Li^+–FSA interactions), instead, the $N_{Li–Nan}(r)$ for the Li^+–AN interaction was ~2.1. **Figure 3.8** shows the $g^{MD}(r)$ for the Li^+–FSA interactions in the LiFSA/TFEP solutions without and with AN. It has been established that in the FSA-based IL containing LiFSA salt, the correlation between Li^+ and N atom (FSA) is a good indicator to distinguish the

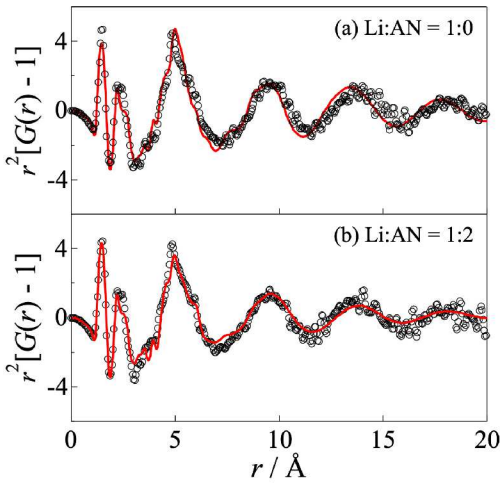

Figure 3.7 X-ray radial distribution functions derived from HEXTS experiments (open circles) and molecular dynamics (MD) simulations (solid lines) for the LiFSA/TFEP solutions (c_{Li} = 1.0 mol dm^{-3}) (a) without AN (Li:AN = 1:0) and (b) with added AN (Li:AN = 1:2).

bi-FSA and mono-FSA in the Li-ion complexes; i.e., a peak at ~3.7 Å is assigned to the bi-FSA and that at ~4.2 Å to the mono-FSA. In the $g^{MD}_{Li\text{-}Nfsa}(r)$ for the LiFSA/TFEP system (without AN), two intense peaks appeared at 3.7 Å (bi-FSA) and 4.2 Å (mono-FSA), and the intensity ratio of mono-FSA to bi-FSA species was

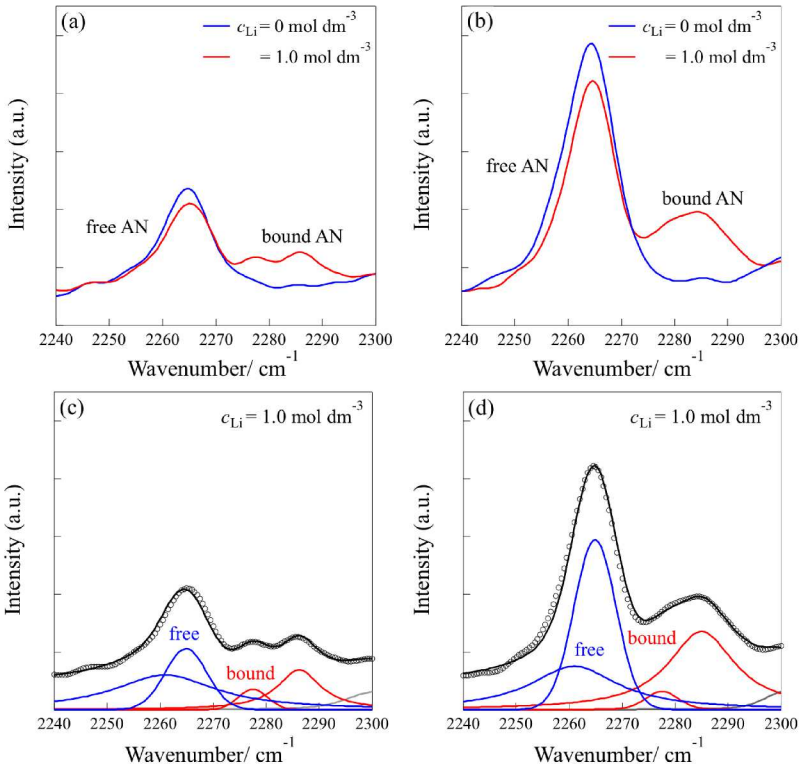

Figure 3.6 Raman spectra for the TFEP+AN solutions containing c_{Li} = 0 mol dm^{-3} (blue) and 1.0 mol dm^{-3} (red) with (a) Li:AN = 1:1 and (b) 1:2, and their band-deconvolution results (c and d, respectively).

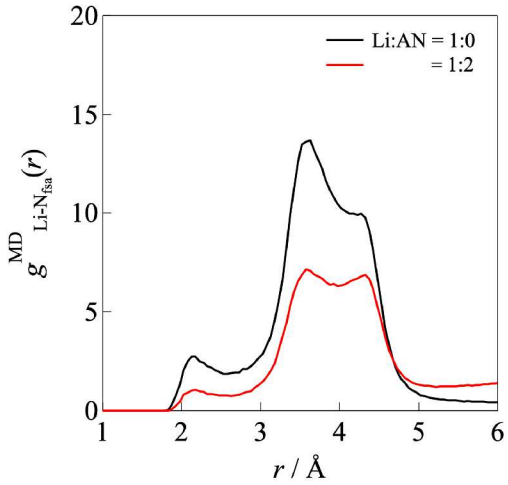

Figure 3.8 Atom-atom pair correlation functions [$g^{MD}_{Li\text{-}Nfsa}(r)$s] for the N atoms of FSA around the Li-ions for the LiFSA/TFEP solutions (c_{Li} = 1.0 mol dm^{-3}) without AN (Li:AN = 1:0, black) and with AN (Li:AN = 1:2, red).

estimated to be [mono-FSA]/[bi-FSA] = 0.32. The intensity ratio increased when adding AN (Li:AN = 1:2 system) to be [mono-FSA]/[bi-FSA] = 0.94. This suggested that a structural change from the bi-FSA to the mono-FSA in the Li-ion complexes evidently occurred by adding neutral ligand, AN.

Consequently, I therefore proposed that (1) Li-ions are coordinated with three components, TFEP and AN molecules, and FSA anions, to form intricate Li-ion complexes in the AN- containing electrolyte system and (2) AN coordination triggers structural changes in the coordinated FSA within the Li-ion complexes, from bi-FSA to mono-FSA.

3.3.4 *Electrode reaction: Li ion insertion/deinsertion in the graphite*

Figure 3.9 shows typical cyclic voltammograms (CVs) of a graphite anode in 1.0 mol dm3 LiFSA/TFEP+AN with Li:AN (by mol) = 1:0, 1:1, and 1:2. For the LiFSA/TFEP system (without AN), no significant redox current was observed from 0–2.0 V (vs. Li/Li+). This indicated that less reactive insertion/deinser- tion of Li ions into/from the graphite electrode occurred in the electrolyte without AN additive. Interestingly, adding AN to the inert LiFSA/TFEP electrolyte promoted the electrode reaction for the graphite: i.e., in the Li:AN = 1:1 system (**Figure 3.9b**), a considerable reductive current was observed from 0.4–0 V during the cathodic scan, due to Li-ion insertion into the graphite, and an oxidative current due to Li-ion deinsertion was observed from 0–0.5 V during the anodic scan. Further increasing the AN content (Li:AN = 1:2 system, **Figure 3.9c**) further increased the redox current to give a sharper CV profile. In the LiFSA/TFEP+AN system, the broad reductive current was observed from 1.0–0.2 V during the first cycle, which is a result of the decomposition of the AN in the solutions. Indeed, the concentration of the free AN, c_{f_AN} [= $c_{T\_AN} - c_{b\_AN}$], which is calculated based on the Raman data analysis described above, increases with increasing AN content (Li:AN = 1:1:0.81 mol dm^{-3}; Li:AN = 1:2:1.62 mol dm^{-3}). The reductive decomposition significantly decreased for subsequent cycles to observe stable and reversible CV profiles. This might be ascribed to a SEI formation on the graphite originated from decomposition of the FSA component. Indeed, the FSA-based SEI passivation film has previously been reported in conventional electrolytes containing LiFSA salt.[25, 9, 26]

Here, I note that the LiFSA/TFEP without AN (Li:AN = 1:0) electrolyte showed almost no or reduced Li-ion insertion/ deinsertion reaction, although the SEI was formed on the graphite electrode to suppress the electrolyte decomposition during subsequent cycles. In contrast, Li-ion insertion evidently occurred in the LiFSA/TFEP with AN. The ionic conductivity of the LiFSA/TFEP electrolytes gradually increased with increasing AN content due to decreasing the solution viscosity (**Figure 3.10a**); however, the values were significantly lower than those of the conventional organic electrolytes (1.0 mol dm^{-3} Li salt in carbonates, AN, and DMF as a solvent; σ = 12–51 mS cm^{-1}, listed in **Table A3.3**). This means that the ionic conductivity plays a minor role on the graphite electrode reaction in the TFEP-based electrolyte system; therefore, I expected that improving electrode/electrolyte interface with adding AN mainly contributes to the electrode reaction. To confirm it, electro- chemical impedance measurements for the three-electrode cell using graphite test electrode were performed. The results as a form of Nyquist plot are shown in Fig. 10b. It was clear that the electrode/electrolyte interfacial resistance (R_{int}), i.e., the diameter of the semicircle in the plots, appreciably decreased with increasing AN content. I thus concluded that in the LiFSA/TFEP+AN system, charge-transfer process at the electrode/ electrolyte interface is key to the graphite electrode reaction, rather than diffusion process in the bulk electrolyte.

As mentioned in the Introduction, specific Li-ion insertion into graphite in the FSA-based IL electrolytes was reported by Ishikawa et al. as follows:[10, 12] (1) in the Li-ion coordination sphere, the Li^+···FSA interactions are significantly weak relative to the Li^+···TFSA interactions in the TFSA-based ILs, and therefore, (2) decoordination (or liberation) of the FSA from the Li-ion coordination sphere occurs easily, which is a crucial factor in the insertion of Li-ions. From a structural viewpoint, I reported a Li-ion coordination structure in the FSA-based IL. Based on the Raman spectroscopy and HEXTS

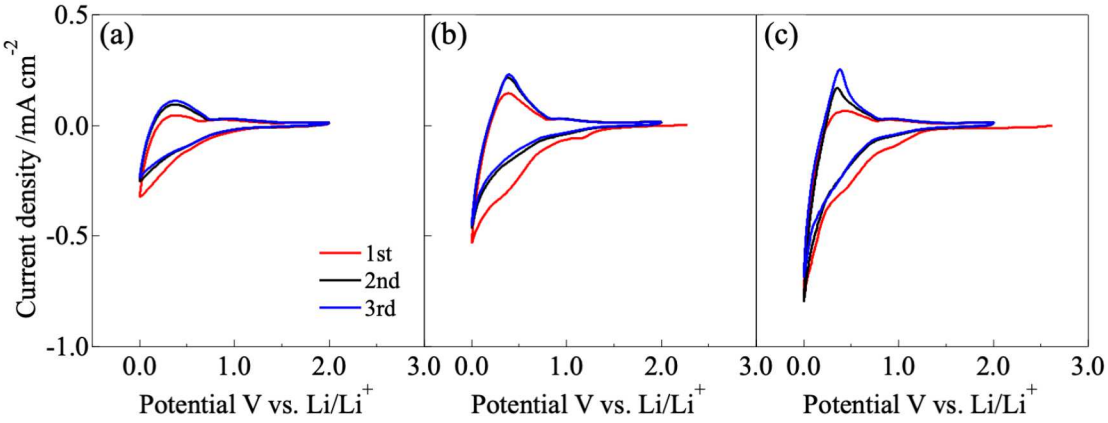

Figure 3.9 Cyclic voltammograms for the graphite electrode in the 1.0 mol dm^{-3} LiFSA/TFEP solutions with AN, Li:AN (by mol) = (a) 1:0 (without AN), (b) 1:1, and (c) 1:2.

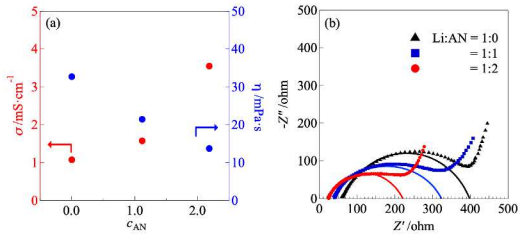

Figure 3.10 (a) Ionic conductivities (red, left axis) and viscosities (blue, right axis) for the 1.0 mol dm^{-3} LiFSA/TFEP + AN solutions with varying AN concentration (c_{AN}). (b) Nyquist plots for the three-electrode cells using graphite test electrode at open circuit potential.

study with the aid of theoretical calculations [DFT calculations and MD simulations],[27] I proposed that in LiFSA/[C_2mIm][FSA] electrolytes, Li ions favor mono-FSA over bi-FSA in the first coordination sphere, affording [Li(mono-FSA)$_2$(bi-FSA)$_1$] complexes as an average structure, and then the mono-FSA anions can easily decoordinate at the interaction energy rather than forming the corresponding bi-TFSA anions. These characteristics of the FSA anion as a ligand could be applied to the current LiFSA/TFEP+AN electrolyte system. Based on the vibrational spectroscopy and combined HEXTS experiments with MD simulations, I demonstrated herein that the FSA anion coordinated to the Li ion as ''bi-FSA'' in the LiFSA/TFEP electrolyte (without AN); however, the bound bi-FSA gradually changed its coordination structure to ''mono-FSA'' when AN was added to the TFEP electrolytes. I therefore concluded that controlled FSA coordination, i.e., designing weak Li-ion···mono-FSA interactions, is an approach to enabling Li-ion insertion/deinsertion in the graphite anode, contributing to decoordination (desolvation) at the electrode/electrolyte interface. This may control (1) the double-layer structure at the graphite interface during charging and (2) the rate-limiting step in the charge-transfer reaction,[28] in addition to the FSA-based SEI on the anode.

3.4 Conclusions

I performed research based on vibrational spectroscopy to characterize Li-ion complex structures in TFEP-based electrolyte solutions containing a LiFSA salt for LIBs. Based on quantitative data analysis of the observed IR/Raman spectra and HEXTS, I demonstrated that (1) [Li(TFEP)$_2$(bi-FSA)] complexes are formed as a major species in a binary LiFSA/TFEP system and (2) in LiFSA/TFEP containing AN, the coordinated bi-FSA changes its coordination mode to "mono-FSA" by solvating AN molecules to the Li ions. This change in the coordination structure triggers the Li-ion insertion/deinsertion in the graphite anode, although no reaction occurs in LiFSA/TFEP without AN. I therefore propose that designing a Li-ion complex with a controlled coordination structure is important in developing a carbonate-free LIB electrolyte system.

3.5 References

(1) Seki, S.; Kobayashi, Y.; Miyashiro, H.; Ohno, Y.; Mita, Y.; Terada, N. Compatibility of *N*-Methyl-*N*-propylpyrrolidinium Cation Room-Temperature Ionic Liquid Electrolytes and Graphite Electrodes. *J. Phys. Chem. C* **2008,** *112*, 16708-16713.

(2) Shobukawa, H.; Shin, J.; Alvarado, J.; Rustomji, C. S.; Meng, Y. S. Electrochemical reaction and surface chemistry for performance enhancement of a Si composite anode using a bis(fluorosulfonyl)imide-based ionic liquid. *J. Mater. Chem. A* **2016,** *4*, 15117-15125.

(3) Hirota, N.; Okuno, K.; Majima, M.; Hosoe, A.; Uchida, S.; Ishikawa, M. High-performance lithium-ion capacitor composed of electrodes with porous three-dimensional current collector and bis(fluorosulfonyl)imide-based ionic liquid electrolyte. *Electrochim. Acta* **2018**.

(4) Hirata, K.; Morita, Y.; Kawase, T.; Sumida, Y. Electrochemical performance of an ethylene carbonate-free electrolyte based on lithium bis(fluorosulfonyl)imide and sulfolane. *J. Power Sources* **2018,** *395*, 163-170.
(5) Shiga, T.; Kato, Y.; Kondo, H.; Okuda, C.-a. Self-extinguishing electrolytes using fluorinated alkyl phosphates for lithium batteries. *Journal of Materials Chemistry A* **2017,** *5*, 5156-5162.
(6) Handa, N.; Sugimoto, T.; Yamagata, M.; Kikuta, M.; Kono, M.; Ishikawa, M. A neat ionic liquid electrolyte based on FSI anion for electric double layer capacitor. *J. Power Sources* **2008,** *185*, 1585-1588.
(7) Hayamizu, K.; Tsuzuki, S.; Seki, S.; Fujii, K.; Suenaga, M.; Umebayashi, Y. Studies on the translational and rotational motions of ionic liquids composed of N-methyl-N-propyl-pyrrolidinium (P13) cation and bis(trifluoromethanesulfonyl)-amide and bis(fluorosulfonyl)amide anions and their binary systems including lithium salts. *J. Chem. Phys.* **2010,** *133*, 194505.
(8) Tsuzuki, S.; Hayamizu, K.; Seki, S. Origin of the Low-Viscosity of [emim][(FSO2)2N] Ionic Liquid and Its Lithium Salt Mixture: Experimental and Theoretical Study of Self-Diffusion Coefficients, Conductivities, and Intermolecular Interactions. *J. Phys. Chem. B* **2010,** *114*, 16329-16336.
(9) Neuhaus, J.; von Harbou, E.; Hasse, H. Physico-chemical properties of solutions of lithium bis(fluorosulfonyl)imide (LiFSI) in dimethyl carbonate, ethylene carbonate, and propylene carbonate. *J. Power Sources* **2018,** *394*, 148-159.
(10) Matsumoto, H.; Sakaebe, H.; Tatsumi, K.; Kikuta, M.; Ishiko, E.; Kono, M. Fast cycling of Li/$LiCoO_2$ cell with low-viscosity ionic liquids based on bis(fluorosulfonyl)imide $[FSI]^-$. *J. Power Sources* **2006,** *160*, 1308-1313.
(11) Fujii, K.; Seki, S.; Fukuda, S.; Kanzaki, R.; Takamuku, T.; Umebayashi, Y.; Ishiguro, S.-i. Anion Conformation of Low-Viscosity Room-Temperature Ionic Liquid 1-Ethyl-3-methylimidazolium Bis(fluorosulfonyl) Imide. *J. Phys. Chem. B* **2007,** *111*, 12829-12833.
(12) Lopes, J. N. C.; Shimizu, K.; Pádua, A. A. H.; Umebayashi, Y.; Fukuda, S.; Fujii, K.; Ishiguro, S. Potential Energy Landscape of Bis(fluorosulfonyl)amide. *J. Phys. Chem. B* **2008,** *112*, 9449-9455.
(13) Fujii, K.; Seki, S.; Ohara, K.; Kameda, Y.; Doi, H.; Umebayashi, Y. High-Energy X-ray Diffraction and MD Simulation Study on the Ion-Ion Interactions in 1-Ethyl-3- methylimidazolium Bis(fluorosulfonyl)amide. *J. Solution Chem* **2014,** *43*, 1655-1688.
(14) Fujii, K.; Seki, S.; Fukuda, S.; Takamuku, T.; Kohara, S.; Kameda, Y.; Umebayashi, Y.; Ishiguro, S.-i. Liquid structure and conformation of a low-viscosity ionic liquid, N-methyl-N-propyl-pyrrolidinium bis(fluorosulfonyl) imide studied by high-energy X-ray scattering. *J. Mol. Liq.* **2008,** *143*, 64-69.
(15) Aurbach, D.; Zaban, A.; Ein-Eli, Y.; Weissman, I. Recent studies on the correlation between surface chemistry, morphology, three-dimensional structures and performance of Li and Li-C intercalation anodes in several important electrolyte systems. *J. Power Sources* **1997,** *68*, 91-98.
(16) Fong, R.; Sacken, U. v.; Dahn, J. R. Studies of Lithium Intercalation into Carbons Using Nonaqueous Electrochemical Cells. *J. Electrochem. Soc.* **1990,** *137*, 2009-2013.
(17) Peled, E. The electrochemical behavior of alkali and alkaline earth metals in nonaqueous battery systems—the solid electrolyte interphase model. *J. Electrochem. Soc.* **1979,** *126*, 2047-2051.
(18) Guerfi, A.; Duchesne, S.; Kobayashi, Y.; Vijh, A.; Zaghib, K. LiFePO4 and graphite electrodes with ionic liquids based on bis(fluorosulfonyl)imide (FSI)− for Li-ion batteries. *J. Power Sources* **2008,** *175*, 866-873.
(19) Sugimoto, T.; Atsumi, Y.; Kikuta, M.; Ishiko, E.; Kono, M.; Ishikawa, M. Ionic liquid electrolyte systems based on bis(fluorosulfonyl)imide for lithium-ion batteries. *J. Power Sources* **2009,** *189*, 802-805.
(20) Ishikawa, M.; Sugimoto, T.; Kikuta, M.; Ishiko, E.; Kono, M. Pure ionic liquid electrolytes compatible with a graphitized carbon negative electrode in rechargeable lithium-ion batteries. *J. Power Sources* **2006,** *162*, 658-662.
(21) Matsui, Y.; Yamagata, M.; Murakami, S.; Saito, Y.; Higashizaki, T.; Ishiko, E.; Kono, M.; Ishikawa, M. Design of an electrolyte composition for stable and rapid charging–discharging of a graphite negative electrode in a bis(fluorosulfonyl)imide-based ionic liquid. *J. Power Sources* **2015,** *279*, 766-773.
(22) Yamagata, M.; Nishigaki, N.; Nishishita, S.; Matsui, Y.; Sugimoto, T.; Kikuta, M.; Higashizaki, T.; Kono, M.; Ishikawa, M. Charge–discharge behavior of graphite negative electrodes in bis(fluorosulfonyl)imide-based ionic liquid and structural aspects of their electrode/electrolyte interfaces. *Electrochimica Acta* **2013,** *110*, 181-190.
(23) Lu, D.; Tao, J.; Yan, P.; Henderson, W. A.; Li, Q.; Shao, Y.; Helm, M. L.; Borodin, O.; Graff, G. L.; Polzin, B.; Wang, C. M.; Engelhard, M.; Zhang, J. G.; De Yoreo, J. J.; Liu, J.; Xiao, J. Formation of Reversible Solid Electrolyte Interface on Graphite Surface from Concentrated Electrolytes. *Nano Lett.* **2017,** *17*, 1602-1609.

(24) Ming, J.; Cao, Z.; Wahyudi, W.; Li, M.; Kumar, P.; Wu, Y.; Hwang, J.-Y.; Hedhili, M. N.; Cavallo, L.; Sun, Y.-K.; Li, L.-J. New Insights on Graphite Anode Stability in Rechargeable Batteries: Li Ion Coordination Structures Prevail over Solid Electrolyte Interphases. *ACS Energy Lett.* **2018**, 335-340.
(25) Zhang, T.; Paillard, E. Recent advances toward high voltage, EC-free electrolytes for graphite-based Li-ion battery. *Front. Chem. Sci. Eng.* **2018,** *12*, 577-591.
(26) Fujii, K.; Hamano, H.; Doi, H.; Song, X.; Tsuzuki, S.; Hayamizu, K.; Seki, S.; Kameda, Y.; Dokko, K.; Watanabe, M.; Umebayashi, Y. Unusual Li^+ Ion Solvation Structure in Bis(fluorosulfonyl)amide Based Ionic Liquid. *J. Phys. Chem. C* **2013,** *117*, 19314-19324.
(27) Xu, K.; Ding, M. S.; Zhang, S.; Allen, J. L.; Jow, T. R. Evaluation of Fluorinated Alkyl Phosphates as Flame Retardants in Electrolytes for Li-Ion Batteries. *J. Electrochem. Soc.* **2003,** *150*, A161-A169.
(28) Xu, K.; Zhang, S.; Allen, J. L.; Jow, T. R. Evaluation of Fluorinated Alkyl Phosphates as Flame Retardants in Electrolytes for Li-Ion Batteries: II. Performance in Cell. *J. Electrochem. Soc.* **2003,** *150*, A170-A175.
(29) Zhang, S. S.; Xu, K.; Jow, T. R. Tris(2,2,2-trifluoroethyl)phoshite as a co-solvent for nonflammable electrolyte in Li-ion batteries.pdf. *J. Power Souces* **2003,** *113*, 166-172.
(30) Sogawa, M.; Todorov, Y. M.; Hirayama, D.; Mimura, H.; Yoshimoto, N.; Morita, M.; Fujii, K. Role of Solvent Bulkiness on Lithium-Ion Solvation in Fluorinated Alkyl Phosphate-Based Electrolytes: Structural Study for Designing Nonflammable Lithium-Ion Batteries. *J. Phys. Chem. C* **2017,** *121*, 19112-19119.
(31) Sogawa, M.; Kawanoue, H.; Todorov, Y. M.; Hirayama, D.; Mimura, H.; Yoshimoto, N.; Morita, M.; Fujii, K. Solvation-controlled lithium-ion complexes in a nonflammable solvent containing ethylene carbonate: structural and electrochemical aspects. *Phys. Chem. Chem. Phys.* **2018,** *20*, 6480-6486.
(32) Ohtaki, H.; Radnai, T. Structure and dynamics of hydrated ions. *Chem. Rev.* **1993,** *93*, 1157-1204.
(33) Burgess, J. *Ions in Solution, 2nd ed.*, Horwood Publishing: 1999.
(34) Marcus, Y. *The Properties of Solvents*, John Wiley & Sons Ltd.: New York, 1998.
(35) Giffin, G. A.; Moretti, A.; Jeong, S.; Passerini, S. Complex Nature of Ionic Coordination in Magnesium Ionic Liquid-Based Electrolytes: Solvates with Mobile Mg^{2+} Cations. *J. Phys. Chem. C* **2014,** *118*, 9966-9973.
(36) Xuan, X.; Zhang, H.; Wang, J.; Wang, H. Vibrational Spectroscopic and Density Functional Studies on Ion Solvation and Association of Lithium Tetrafluorobrate in Acetonitrile. *J. Phys. Chem. A* **2004,** *108*, 7513-7521.
(37) Sai, R.; Ueno, K.; Fujii, K.; Nakano, Y.; Shigaki, N.; Tsutsumi, H. Role of polar side chains in Li^+ coordination and transport properties of polyoxetane-based polymer electrolytes. *Phys. Chem. Chem. Phys.* **2017,** *19*, 5185-5194.
(38) Shkrob, I. A.; Marin, T. W.; Zhu, Y.; Abraham, D. P. Why Bis(fluorosulfonyl)imide Is a "Magic Anion" for Electrochemistry. *J. Phys. Chem. C* **2014,** *118*, 19661-19671.
(39) Budi, A.; Basile, A.; Opletal, G.; Hollenkamp, A. F.; Best, A. S.; Rees, R. J.; Bhatt, A. I.; O'Mullane, A. P.; Russo, S. P. Study of the Initial Stage of Solid Electrolyte Interphase Formation upon Chemical Reaction of Lithium Metal and N-Methyl-N-Propyl-Pyrrolidinium-Bis(Fluorosulfonyl)Imide. *J. Phys. Chem. C* **2012,** *116*, 19789-19797.
(40) Abe, T.; Fukuda, H.; Iriyama, Y.; Ogumi, Z. Solvated Li-Ion Transfer at Interface Between Graphite and Electrolyte. *J. Electrochem. Soc.* **2004,** *151*, A1120.

3.6 Appendix

Modified partial charges (MD simulation).

In our previous study (LiTFSA/TFEP and LiTFSA/AN systems),[29] we examined to modify partial charges (q^+ and q^-: original values are shown in **Figure A3.1**) by weighting a factor (f), resulting in a successful agreement of experimental and simulation-derived radial distribution functions [$G^{exp}(r)$ and $G^{MD}(r)$, respectivily]. The optimum value, $f = 0.6$ (i.e., 60% of the original q^+ and q^-) for the TFEP and Li-TFSA ion-pair and $f = 1.0$ for the AN. In this work (LiFSA/TFEP and LiFSA/TFEP+AN systems), I thus used (1) $f = 0.6$ for the TFEP and Li-FSA and (2) $f = 1.0$ for the AN in the current MD simulations.The $G^{MD}(r)$ using the fq^+ and fq^- in Coulombic term successfully reproduced the corresponding experimental $G^{exp}(r)$, as shown in Fig. 7.

Estimation of c_{f_FSA} and c_{b_FSA} values.

I measured separately IR spectra of [C_2mIm][FSA]/TFEP system (without LiFSA salt) with $c_{C2mImFSA}$ = 0, 0.5, and 1.0 mol dm^{-3} (**Figure A3.2a**). The peak (from 700 to 780 cm^{-1}, S-N-S symmetric stretching mode of the FSA component) increased in intensity with $c_{C2mImFSA}$, which could be assigned to the free FSA. The observed spectra were represented using two free FSA bands (typical result for $c_{C2mImFSA}$ = 1.0 mol dm^{-3}, **Figure A3.2b**), which is consistent with the current LiFSA/TFEP system described in the manuscript. The integrated intensities of the two free FSA bands, I_{f_FSA} ($= I_{745} + I_{758}$) were plotted against c_{FSA} ($=c_{C2mImFSA}$) (**Figure A3.2c**) and the slope corresponds to the ε_{f_FSA} value according to the following relation: $I_{f\_FSA} = \varepsilon_{f\_FSA}\, c_{f\_FSA}$.

The ε_{b_FSA} value was also estimated based on the following relations: $I_{b\_FSA} = \varepsilon_{b\_FSA}\, c_{b\_FSA}$ and $c_{b\_FSA} = n_{FSA}\, c_{Li}$. Consequently, the ratio of molar absorption coefficients ($\varepsilon_{f\_FSA}/\varepsilon_{b\_FSA}$) was determined to be 1.72. Appling the ε_{f_FSA} value to the LiFSA/TFEP system, I can estimate c_{f_FSA} value ($= I_{f\_FSA}/\varepsilon_{f\_FSA}$) and c_{b_FSA} ($=c_{T\_FSA} - c_{f\_FSA}$).

Estimation of J_{f_AN} value.

To determine J_{f_AN} value, I measured separately Raman spectra of TFEP+AN mixed solution (without LiFSA salt) with c_{AN} = 0, 1.0, and 2.0 mol dm^{-3} (**Figure A3.4a**). The peak (2265 cm^{-1}, N≡C symmetric stretching mode of AN) increased linearly in intensity with c_{AN}, which could be assigned to the free AN owing to very weak intermolecular interactions between TFEP and AN. The observed spectra were represented using two free AN bands (typical result for c_{AN} = 2.0 mol dm^{-3}, **Figure A3.4b**), which is consistent with the current LiFSA/TFEP+AN system described in the manuscript. The integrated intensities of the two free AN bands, I_{f_AN} ($= I_{2261} + I_{2265}$) were plotted against c_{AN} (**Figure A3.4c**) and the slope corresponds to the J_{f_AN} value according to the following relation: $I_{f\_AN} = J_{f\_AN}\, c_{f\_AN}$.

The J_{b_AN} value was also estimated based on the following relations: $I_{b\_AN} = J_{b\_AN}\, c_{b\_AN}$ and $c_{b\_AN} = n_{AN}\, c_{Li}$. Consequently, the ratio of Raman scattering coefficients (J_{f_AN}/J_{b_AN}) was determined to be 0.57.

Table A3.1 Molar ratio (salt:solvent), concentrations of LiFSA salt (c_{Li}), TFEP (c_{TFEP}), and AN (c_{AN}), density (d), refractive index (n_2) for binary LiFSA/TFEP and ternary LiFSA/TFEP+AN solutions.

binary LiFSA/TFEP system				
LiFSA : TFEP	c_{Li} / mol dm^{-3}	c_{TFEP} / mol dm^{-3}	d / g cm^{-3}	n_2
-	0	4.60	1.450	1.329
1 : 22.7	0.20	4.53	1.596	1.329
1 : 11.2	0.40	4.46	1.611	1.329
1 : 7.32	0.60	4.39	1.625	1.329
1 : 5.38	0.80	4.30	1.633	1.332
1 : 4.24	1.00	4.24	1.648	1.332

ternary LiFSA/TFEP+AN system					
LiFSA : TFEP:AN	c_{Li} /mol dm^{-3}	c_{TFEP} /mol dm^{-3}	c_{AN} /mol dm^{-3}	d / g cm^{-3}	n_2
1 : 3.96 : 1.02	1.00	3.96	1.02	1.599	1.334
1 : 3.70 : 2.04	1.00	3.70	2.04	1.552	1.336

Table A3.2 c_{Li}, c_{AN}, d and compositions (number of ion-pairs and solvents) for the MD simulations (1.0 mol dm^{-3} LiFSA/TFEP solutions with AN, Li:AN (by mol.) = 1:0 and 1:2).

c_{Li} / mol dm^{-3}	c_{AN} / mol dm^{-3}	d / g cm^{-3}		Li-FSA	TFEP	AN
		Exp.[a]	MD[b]			
1.0	-	1.648	1.678	133	567	-
1.0	2.0	1.552	1.578	145	538	317

[a] Value obtained from the present MD simulations. [b] Experimental values.

Table A3.3 Ionic conductivities of c_{Li} = 1.0 mol dm^{-3} solutions at 298K.

Sample	σ /mS·cm^{-1} (at 298K)
LiTFSA/EC+DMC [30, 6]	51.0
LiTFSA/AN [31]	38.0 (at 303K)
LiTFSA/H_2O [6]	36.8
LiTFSA/DMF [32, 6]	15.1
$LiPF_6$/EC+DMC [30, 6]	12.1
LiFSA/TFEP (Li:AN = 1:0)	1.1
LiFSA/TFEP (Li:AN = 1:1)	1.6
LiFSA/TFEP (Li:AN = 1:2)	3.5

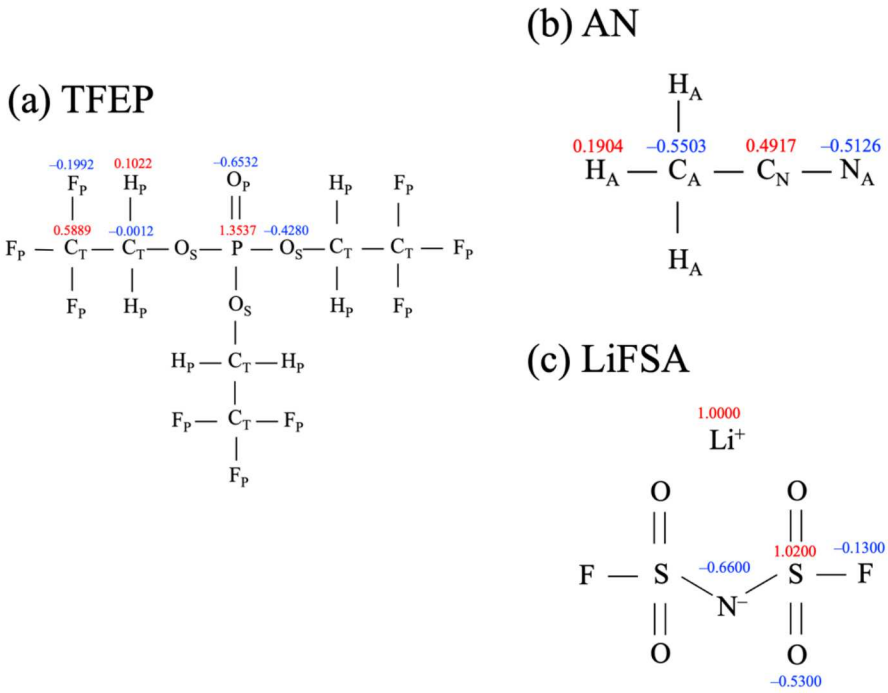

Figure A3.1 The original partial charge values of (a) TFEP, (b) AN,[33] and (c) LiFSA[34]. The values of TFEP were calculated based on ChelpG method (MP2/cc-pVTZ(-f) calculation).[29]

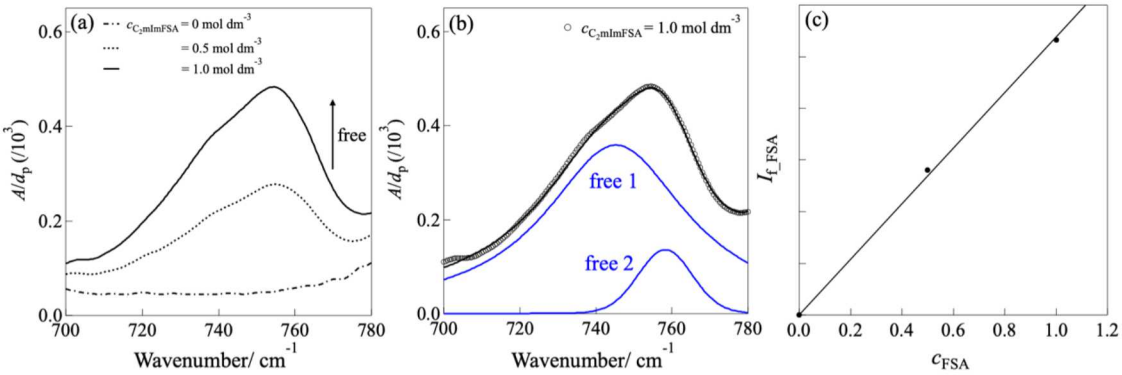

Figure A3.2 (a) FT-IR spectra for the TFEP solution with varying $c_{C2mImFSA}$, (b) A curve-fitting result for the $c_{C2mImFSA}$ = 1.0 mol dm^{-3} solution, and (c) The integrated intensities of the two free FSA bands, I_{f_FSA} (= I_{745} + I_{758}) plotted against FSA concentration (c_{FSA}).

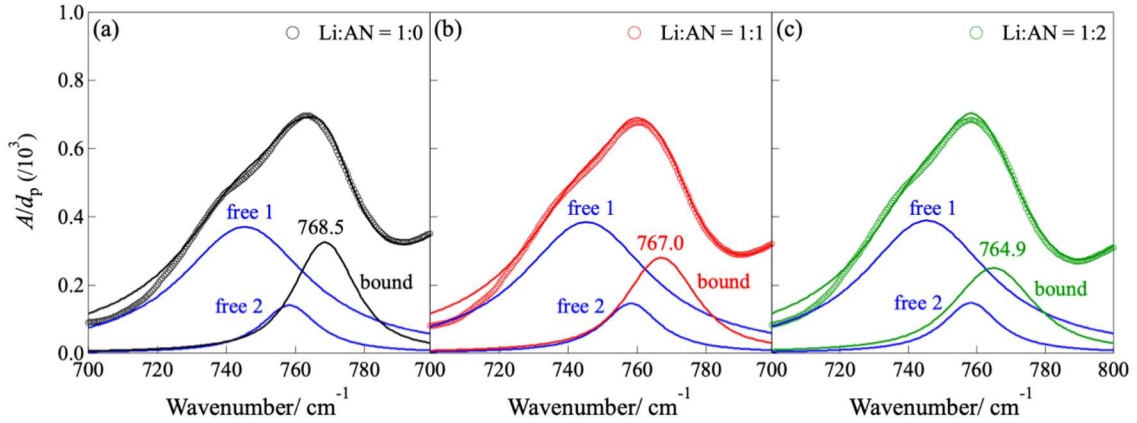

Figure A3.3 Curve fitting results of the IR spectra observed for the 1.0 mol dm^{-3} LiFSA/TFEP solutions with added AN: (a) Li:AN (by mol.) = 1:0, (b) 1:1, and (c) 1:2.

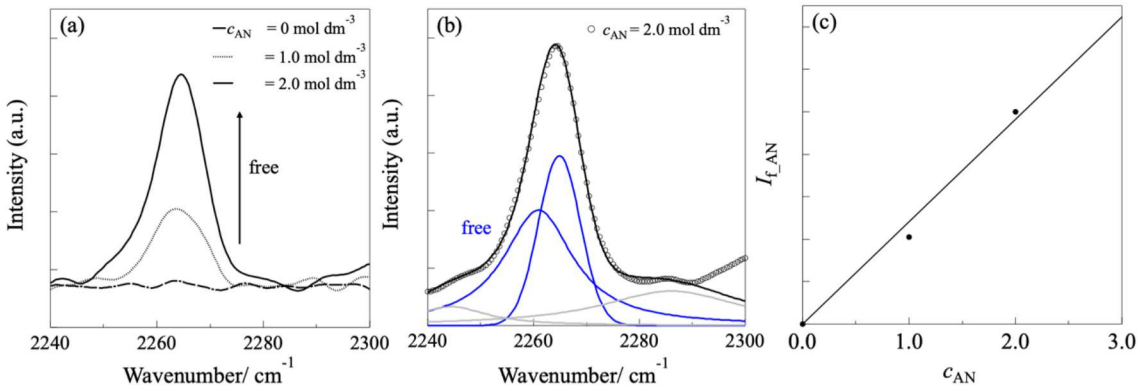

Figure A3.4 (a) Raman spectra for the TFEP+AN mixed solutions (without LiFSA salt) with c_{AN} = 0, 1.0, and 2.0 mol dm^{-3}, (b) A curve-fitting result for 1.0 mol dm^{-3} LiFSA/TFEP with c_{AN} = 2.0 mol dm^{-3} and (c) The integrated intensities of the two free AN bands, I_{f_AN} (= I_{2261} + I_{2265}) plotted against c_{AN}.

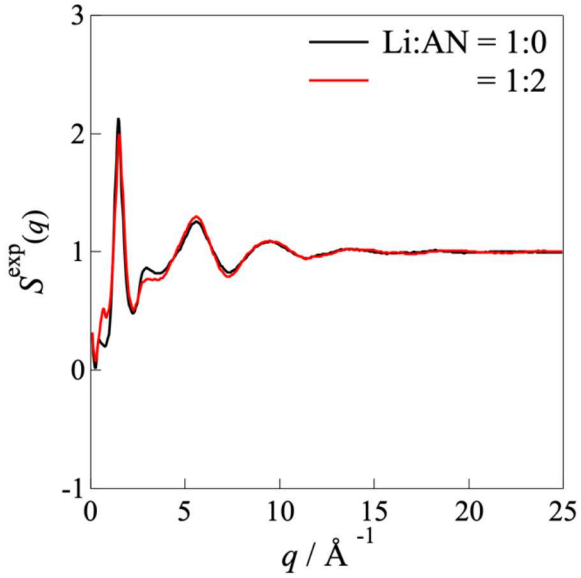

Figure A3.5 $S^{exp}(q)$ profiles obtained from HEXTS measurements for 2.5 mol dm^{-3} LiFSA/TFEP +AN solutions (Li:AN = 1:0 and 1:2).

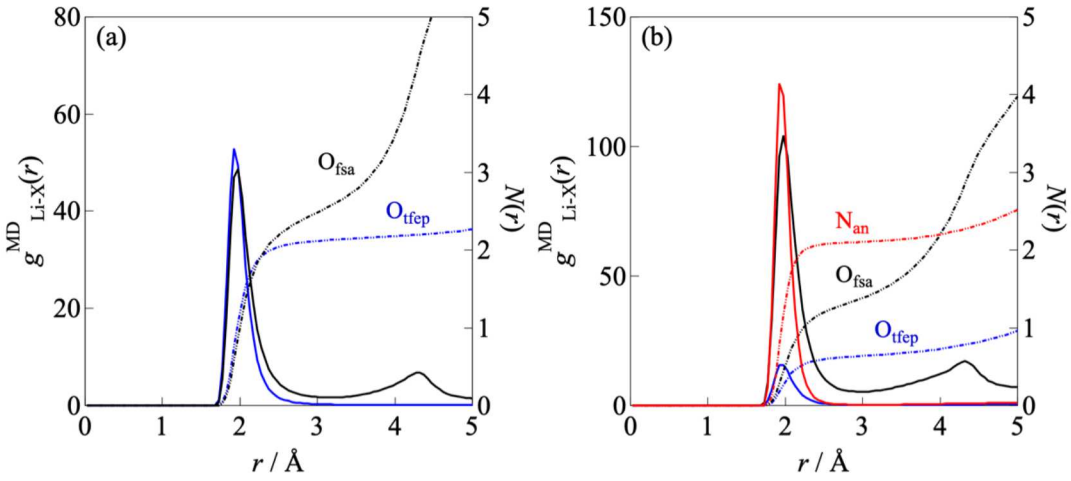

Figure A3.6 Atom-atom pair correlation functions [$g^{MD}_{Li-X}(r)$: left axis, solid lines] for the O atoms of TFEP (blue), the O atoms of FSA (black) and the N atoms of AN (red) around the Li-ions and their integrated profiles [coordination number $N(r)$: right axis, dashed lines] for (a) 1.0 mol dm^{-3} LiFSA/TFEP solution and (b) that with AN (Li:AN = 1:2).

References

(1) Xu, K.; Ding, M. S.; Zhang, S.; Allen, J. L.; Jow, T. R. Evaluation of Fluorinated Alkyl Phosphates as Flame Retardants in Electrolytes for Li-Ion Batteries. *J. Electrochem. Soc.* **2003,** *150*, A161-A169.
(2) Xu, K.; Zhang, S.; Allen, J. L.; Jow, T. R. Evaluation of Fluorinated Alkyl Phosphates as Flame Retardants in Electrolytes for Li-Ion Batteries: II. Performance in Cell. *J. Electrochem. Soc.* **2003,** *150*, A170-A175.
(3) Hazama, T.; Fujii, K.; Sakai, T.; Aoki, M.; Mimura, H.; Eguchi, H.; Todorov, Y.; Yoshimoto, N.; Morita, M. High-performance gel electrolytes with tetra-armed polymer network for Li ion batteries. *J. Power Sources* **2015,** *286*, 470-474.

(4) Todorov, Y. M.; Aoki, M.; Mimura, H.; Fujii, K.; Yoshimoto, N.; Morita, M. Thermal and electrochemical properties of nonflammable electrolyte solutions containing fluorinated alkylphosphates for lithium-ion batteries. *J. Power Sources* **2016,** *332*, 322-329.
(5) Todorov, Y. M.; Fujii, K.; Yoshimoto, N.; Hirayama, D.; Aoki, M.; Mimura, H.; Morita, M. Ion-solvation structure and battery electrode characteristics of nonflammable organic electrolytes based on tris(trifluoroethyl)phosphate dissolving lithium salts. *Phys. Chem. Chem. Phys.* **2017,** *19*, 31085-31093.
(6) Sogawa, M.; Todorov, Y. M.; Hirayama, D.; Mimura, H.; Yoshimoto, N.; Morita, M.; Fujii, K. Role of Solvent Bulkiness on Lithium-Ion Solvation in Fluorinated Alkyl Phosphate-Based Electrolytes: Structural Study for Designing Nonflammable Lithium-Ion Batteries. *J. Phys. Chem. C* **2017,** *121*, 19112-19119.
(7) Guerfi, A.; Duchesne, S.; Kobayashi, Y.; Vijh, A.; Zaghib, K. $LiFePO_4$ and graphite electrodes with ionic liquids based on bis(fluorosulfonyl)imide $(FSI)^-$ for Li-ion batteries. *J. Power Sources* **2008,** *175*, 866-873.
(8) Hirata, K.; Morita, Y.; Kawase, T.; Sumida, Y. Electrochemical performance of an ethylene carbonate-free electrolyte based on lithium bis(fluorosulfonyl)imide and sulfolane. *J. Power Sources* **2018,** *395*, 163-170.
(9) Shiga, T.; Kato, Y.; Kondo, H.; Okuda, C.-a. Self-extinguishing electrolytes using fluorinated alkyl phosphates for lithium batteries. *J. Mater. Chem. A* **2017,** *5*, 5156-5162.
(10) Ishikawa, M.; Sugimoto, T.; Kikuta, M.; Ishiko, E.; Kono, M. Pure ionic liquid electrolytes compatible with a graphitized carbon negative electrode in rechargeable lithium-ion batteries. *J. Power Sources* **2006,** *162*, 658-662.
(11) Matsui, Y.; Yamagata, M.; Murakami, S.; Saito, Y.; Higashizaki, T.; Ishiko, E.; Kono, M.; Ishikawa, M. Design of an electrolyte composition for stable and rapid charging–discharging of a graphite negative electrode in a bis(fluorosulfonyl)imide-based ionic liquid. *J. Power Sources* **2015,** *279*, 766-773.
(12) Sugimoto, T.; Atsumi, Y.; Kikuta, M.; Ishiko, E.; Kono, M.; Ishikawa, M. Ionic liquid electrolyte systems based on bis(fluorosulfonyl)imide for lithium-ion batteries. *J. Power Sources* **2009,** *189*, 802-805.
(13) Yamagata, M.; Nishigaki, N.; Nishishita, S.; Matsui, Y.; Sugimoto, T.; Kikuta, M.; Higashizaki, T.; Kono, M.; Ishikawa, M. Charge–discharge behavior of graphite negative electrodes in bis(fluorosulfonyl)imide-based ionic liquid and structural aspects of their electrode/electrolyte interfaces. *Electrochimica Acta* **2013,** *110*, 181-190.
(14) Zhang, S. S.; Xu, K.; Jow, T. R. Tris(2,2,2-trifluoroethyl) phoshite as a co-solvent for nonflammable electrolytes in Li-ion batteries. *J. Power Souces* **2003,** *113*, 166-172.
(15) Sogawa, M.; Kawanoue, H.; Todorov, Y. M.; Hirayama, D.; Mimura, H.; Yoshimoto, N.; Morita, M.; Fujii, K. Solvation-controlled lithium-ion complexes in a nonflammable solvent containing ethylene carbonate: structural and electrochemical aspects. *Phys. Chem. Chem. Phys.* **2018,** *20*, 6480-6486.
(16) Burgess, J. *Ions in Solution, 2nd ed.*, Horwood Publishing: 1999.
(17) Ohtaki, H.; Radnai, T. Structure and dynamics of hydrated ions. *Chem. Rev.* **1993,** *93*, 1157-1204.
(18) Fujii, K.; Seki, S.; Fukuda, S.; Kanzaki, R.; Takamuku, T.; Umebayashi, Y.; Ishiguro, S.-i. Anion Conformation of Low-Viscosity Room-Temperature Ionic Liquid 1-Ethyl-3-methylimidazolium Bis(fluorosulfonyl) Imide. *J. Phys. Chem. B* **2007,** *111*, 12829-12833.
(19) Fujii, K.; Seki, S.; Ohara, K.; Kameda, Y.; Doi, H.; Umebayashi, Y. High-Energy X-ray Diffraction and MD Simulation Study on the Ion-Ion Interactions in 1-Ethyl-3-methylimidazolium Bis(fluorosulfonyl)amide. *J. Solution Chem* **2014,** *43*, 1655-1688.
(20) Lopes, J. N. C.; Shimizu, K.; Pádua, A. A. H.; Umebayashi, Y.; Fukuda, S.; Fujii, K.; Ishiguro, S. Potential Energy Landscape of Bis(fluorosulfonyl)amide. *J. Phys. Chem. B* **2008,** *112*, 9449-9455.
(21) MARCUS, Y. *The Properties of Solvents*, John Wiley & Sons Ltd.: New York, 1998.
(22) Giffin, G. A.; Moretti, A.; Jeong, S.; Passerini, S. Complex Nature of Ionic Coordination in Magnesium Ionic Liquid-Based Electrolytes: Solvates with Mobile Mg^{2+} Cations. *J. Phys. Chem. C* **2014,** *118*, 9966-9973.
(23) Sai, R.; Ueno, K.; Fujii, K.; Nakano, Y.; Shigaki, N.; Tsutsumi, H. Role of polar side chains in Li^+ coordination and transport properties of polyoxetane-based polymer electrolytes. *Phys. Chem. Chem. Phys.* **2017,** *19*, 5185-5194.
(24) Xuan, X.; Zhang, H.; Wang, J.; Wang, H. Vibrational Spectroscopic and Density Functional Studies on Ion Solvation and Association of Lithium Tetrafluorobrate in Acetonitrile. *J. Phys. Chem. A* **2004,** *108*, 7513-7521.
(25) Budi, A.; Basile, A.; Opletal, G.; Hollenkamp, A. F.; Best, A. S.; Rees, R. J.; Bhatt, A. I.; O'Mullane, A. P.; Russo, S. P. Study of the Initial Stage of Solid Electrolyte Interphase Formation upon Chemical Reaction of Lithium Metal and *N*-Methyl-*N*-Propyl-Pyrrolidinium-Bis(Fluorosulfonyl)Imide. *J. Phys. Chem. C* **2012,** *116*, 19789-19797.
(26) Shkrob, I. A.; Marin, T. W.; Zhu, Y.; Abraham, D. P. Why Bis(fluorosulfonyl)imide Is a "Magic Anion" for Electrochemistry. *J. Phys. Chem. C* **2014,** *118*, 19661-19671.

(27) Fujii, K.; Hamano, H.; Doi, H.; Song, X.; Tsuzuki, S.; Hayamizu, K.; Seki, S.; Kameda, Y.; Dokko, K.; Watanabe, M.; Umebayashi, Y. Unusual Li^+ Ion Solvation Structure in Bis(fluorosulfonyl)amide Based Ionic Liquid. *J. Phys. Chem. C* **2013,** *117*, 19314-19324.
(28) Abe, T.; Fukuda, H.; Iriyama, Y.; Ogumi, Z. Solvated Li-Ion Transfer at Interface Between Graphite and Electrolyte. *J. Electrochem. Soc.* **2004,** *151*, A1120.
(29) Sogawa, M.; Sawayama, S.; Han, J.; Satou, C.; Ohara, K.; Matsugami, M.; Mimura, H.; Morita, M.; Fujii, K. Role of Solvent Size in Ordered Ionic Structure Formation in Concentrated Electrolytes for Lithium-Ion Batteries. *J. Phys. Chem. C* **2019**.
(30) Dahbi, M.; Ghamouss, F.; Tran-Van, F.; Lemordant, D.; Anouti, M. Comparative study of EC/DMC LiTFSI and $LiPF_6$ electrolytes for electrochemical storage. *J. Power Sources* **2011,** *196*, 9743-9750.
(31) Yamada, Y.; Furukawa, K.; Sodeyama, K.; Kikuchi, K.; Yaegashi, M.; Tateyama, Y.; Yamada, A. Unusual stability of acetonitrile-based superconcentrated electrolytes for fast-charging lithium-ion batteries. *J. Am. Chem. Soc.* **2014,** *136*, 5039-5046.
(32) Fujii, K.; Wakamatsu, H.; Todorov, Y.; Yoshimoto, N.; Morita, M. Structural and Electrochemical Properties of Li Ion Solvation Complexes in the Salt-Concentrated Electrolytes Using an Aprotic Donor Solvent, *N,N*-Dimethylformamide. *J. Phys. Chem. C* **2016,** *120*, 17196-17204.
(33) Nikitin, A. M.; Lyubartsev, A. P. New six-site acetonitrile model for simulations of liquid acetonitrile and its aqueous mixtures. *J Comput Chem* **2007,** *28*, 2020-2026.
(34) Lopes, J. N. A. C.; Pádua, A. A. H. Molecular Force Field for Ionic Liquids III: Imidazolium, Pyridinium, and Phosphonium Cations; Chloride, Bromide, and Dicyanamide Anions. *J. Phys. Chem. B* **2006,** *110*, 19586-19592.

Chapter 4

Fluorophosphate-Based Nonflammable Concentrated Electrolytes with a Designed Lithium-Ion-Ordered Structure: Relationship between the Bulk Electrolyte and Electrode Interface Structures

4.1 Introduction

In our previous work, we have reported both dilute and concentrated LIB electrolytes using TFEP (main solvent) and LiTFSA or LiFSA;[1-4] however, limited electrode reaction (i.e., no to little Li-ion insertion into the graphite negative electrode) has been observed in TFEP-based electrolytes. By performing a structural study based on both experimental and theoretical techniques, we demonstrated that there was no specific ionic structure in the concentrated TFEP electrolyte and that the Li ions exist as a mononuclear complex. This is due to the solvation steric effect around Li ions arising from the size of bulky TFEP molecules, which suppresses specific liquid structure formation based on multiple ion pair complexes.[2] In the case of smaller organic solvents (e.g., carbonate solvents such as EC and DMC, AN, dimethyl sulfoxide (DMSO), or *N*,*N*-dimethylformamide (DMF), etc.), multiple ion pairs, i.e., the ordered Li-ion complexes bridged through anions, are evidently formed in all systems, leading to successful LIB electrode reactions.[5-9] Thus, the structural modification of Li-ion complexes in concentrated TFEP electrolytes is required to produce nonflammable organic electrolytes that encourage excellent LIB performance. Herein, I propose a method to design the molecular level features of Li-ion-ordered structures in concentrated TFEP electrolyte systems, thereby producing a small molecular additive in TFEP solutions to trigger drastic structural changes in Li-ion complexes. This can lead to nano-scale Li-ion-ordered structure enhancing LIB performance. I used LiFSA salt and TFEP solvent to prepare nonflammable concentrated electrolytes, while AN was used as an additive to modify the Li-ion complex. The Li-ion structures were investigated in the bulk electrolyte system *via* high-energy X-ray total scattering (HEXTS) aided by computational techniques. Furthermore, *in situ* surface-enhanced infrared absorption spectroscopy (SEIRAS) was conducted to elucidate the structure of the electrode/electrolyte interface and enable a discussion of the relationship between the bulk electrolyte and electrode interface structures.

4.2 Experimental

4.2.1 Materials

I prepared ternary LiFSA/TFEP+AN solutions at fixed c_{Li} = 2.5 mol dm^{-3} and varied the ratio of Li salt to AN (by mol.), i.e., Li:AN = 1:0, 1:1, and 1:2 (termed the 1:0, 1:1, and 1:2 solutions). The 1:0 solution corresponds to the binary LiFSA/TFEP solution. Sample electrolyte solutions were prepared by weighing the solvent and Li salt to the required molar ratio (Li salt:solvent) in an Ar-filled glovebox; the corresponding molarities (Li salt concentration, c_{Li}) were then calculated using the solution density (g cm^{-3}) are listed in **Table A4.1** (in **Appendix**). For all solutions examined, we demonstrated "nonflammability" upon adding AN (a flammable solvent) to TFEP (**Figure A4.1**). The composition (i.e., number of LiFSA salts and solvent molecules) of the MD simulation box is listed in **Table A4.2**. The resulting density values were in good agreement with the corresponding experimental density values. Flame tests were conducted by using a glass filter soaked with each electrolyte close to gas burner flame in a draft chamber.

4.3 Results and Discussion

4.3.1 *Electrochemical properties*

Figure A4.2 shows the electrochemical windows obtained from LSV measurements for 2.5 mol dm^{-3} LiFSA/TFEP+AN solutions (Li:AN = 1:0, 1:1, and 1:2). In all examined solutions, almost no current was present between −0.2 and 5.3 V (vs. Li/Li$^+$). Slight reductive currents were observed in the range of 0.1−1.0 V for the 1:1 and 1:2 solutions, which could be ascribed to the reductive decomposition of free AN in the bulk. These details are discussed based on Raman spectral data in an **Appendix** (**Figure A4.3**). **Figures 4.1a, b, and c** show

the cyclic voltammograms (CVs) for the graphite electrode in the Li:AN = 1:0 (without AN), 1:1, and 1:2 solutions, respectively. In the binary LiFSA/TFEP solution (1:0), no significant redox current was observed in the range of 0–2.5 V, indicating limited reactive insertion/deinsertion of containing AN as a result of the decomposition of their FSA component (discussed in detail in a later section). This resulted in further suppressed electrolyte decomposition during subsequent cycles. The reactivity of the graphite electrode strongly depended on AN content, i.e., larger and sharper currents were found in the CV profile for the 1:2 solution than in those of the 1:1 solution. Furthermore, in the 1:2 solution, the observed redox peaks in the range of 0–0.5 V were split into several peaks, which is characteristic of the sequential formation of multi-stage structures of Li–graphite intercalation compounds (Li–GIC).[10-13] We concluded that the Li:AN = 1:2 solution provides the optimal composition in the LiFSA/TFEP+AN electrolyte examined herein; thus, we performed a charge–discharge test for the 1:2 solution. Figure 1d shows the charge–discharge curves obtained using a graphite/Li half-cell containing the Li:AN = 1:2 solution. Several voltage plateaus appeared across the range of 0.05−0.25 V, which corresponds to the formation of Li–GIC.[11] The discharge capacity during the first cycle (~370 mAh g^{-1}) was comparable to the theoretical capacity of fully lithiated LiC_6 (~372 mAh g^{-1}).[12-13] Capacity degradation gradually occurred up to the tenth cycle and was more significant in subsequent cycles (**Figure 4.1e**; red, left axis). This degradation may have originated from the reductive decomposition of free AN molecules in the 1:2 solution. Indeed, based on Raman spectra, the concentration of free AN (C≡N stretching mode, c_{f_AN}) in the solution was estimated to be c_{f_AN} = 1.1 mol dm^{-3} (22% of the total AN concentration). The detailed procedure is described in an **Appendix** (**Figure A4.3**). The coulomb efficiency remained approximately 98.0% unchanged over all cycles examined (**Figure 4.1e**; blue, right axis), with the exception of the first cycle which was influenced by irreversible reduction from SEI formation.

Ionic conductivity (σ) increased upon the addition of AN to the concentrated LiFSA/TFEP electrolyte, as shown in **Figure A4.4**; however, the absolute σ value was one order of magnitude lower than that of conventional carbonate-based organic electrolytes.[14-17] Thus, we suggest that ion-conducting properties are responsible for only a minor contribution to the graphite electrode reaction in this system, i.e., by adding AN, a substantial improvement in the electrode/electrolyte interface may occur. Indeed, electrode/electrolyte interface resistance gradually decreased with increasing AN content according to electrochemical impedance measurements for the three-electrode cell using a graphite electrode (Nyquist plot, **Figure A4.5**). This implies that the graphite electrode reaction undergoes charge transfer processes primarily at the electrode/electrolyte interface, rather than diffusion processes in the bulk electrolyte. Based on these results, we suggest that improvements in the graphite electrode reaction when adding AN are related to changes of the

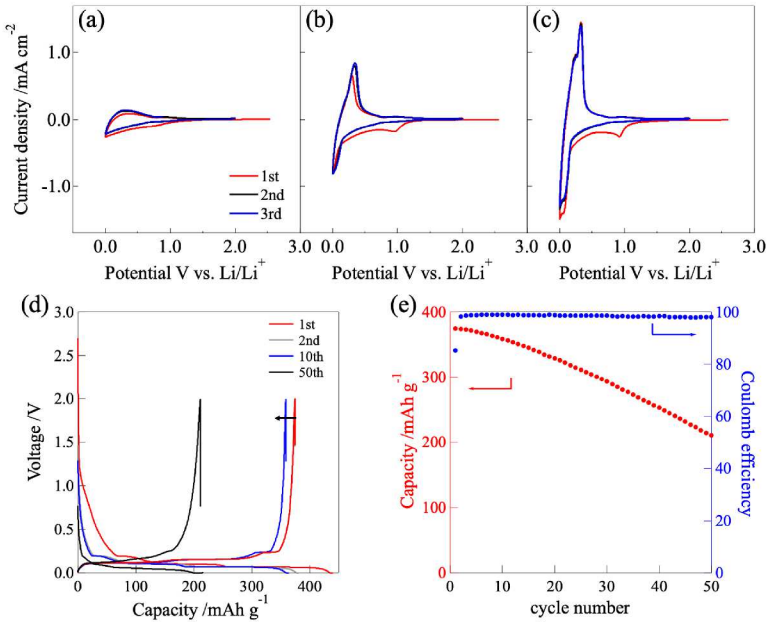

Figure 4.1 CV profiles for graphite electrodes in concentrated LiFSA/TFEP+AN solutions (Li:AN = (a) 1:0, (b) 1:1, and (c) 1:2 (scan rate: 0.2 mV s^{-1}). (d) Charge–discharge curves for the graphite electrode in the concentrated LiFSA/TFEP+AN solution with Li:AN = 1:2 at a 0.1 C rate. (e) Cycling performance (red, left axis) and coulomb efficiency (blue, right axis) of the same solution.

specific solution structure in concentrated TFEP-based electrolytes, resulting in a modified electrode/electrolyte interface. Consequently, we performed a structural study based on combined HEXTS experiments with all-atom MD simulations.

4.3.2 *Bulk electrolyte structures*

Figure 4.2 shows typical results for the X-ray structure factor, $S(q)$, and the X-ray radial distribution function, $G(r)$ (shown in its r-weighted difference form, $r^2[G(r) - 1]$), obtained from HEXTS experiments and MD simulations for the 2.5 mol dm^{-3} LiFSA/TFEP+AN solution with Li:AN = 1:2. The $S(q)$ and $G(r)$ values obtained for the binary LiFSA/TFEP solution (Li:AN = 1:0) are shown in **Figures A4.6a and b**. Here, we examined to measure Raman and attenuated total reflection infrared (ATR-IR) spectra for the LiFSA/TFEP solutions. However, no c_{Li} dependence of the Raman band [O-P-O asymmetric stretching mode of TFEP[17]] was observed (see **Figure A4.7**). This indicated that Raman spectra were not suitable to investigate the TFEP-based solutions. This is because the Raman bands of TFEP are less sensitive to Li ion solvation, i.e., no observation of the peak shift originating from "free TFEP" to "bound TFEP". We further tried to obtain experimental support and measure the IR spectra since we successfully determined the Li- ion complex structure by IR technique in our previous work (dilute system, c_{Li} <1.0 mol dm^{-3}). However, the IR spectra originating from the TFEP (860-930 cm^{-1}) turned out to be overlapped with many bands.[17] Furthermore, increasing c_{Li} made the spectra broader and more complicated, making it unable to analyze using a conventional peak-deconvolution based on a least-squares fitting in the concentrated system. It is thus difficult to determine the Li ion complex structure via Raman and IR investigations. The MD-derived theoretical $S^{MD}(q)$ accurately reproduced the HEXTS-derived experimental $S^{exp}(q)$ (**Figure 4.2a**). A good agreement in the $G^{MD}(r)$ and $G^{exp}(r)$ values was also confirmed (**Figure 4.2b**), suggesting that the parameters used in the MD simulations examined herein were valid, enabling us to analyze the solution structure at the molecular level based on simulation data. To discuss the detailed coordination structure of Li-ion complexes, we separated the total $G^{MD}(r)$ into its intramolecular and the intermolecular components, i.e., $G^{MD}_{total}(r) = G^{MD}_{intra}(r) + G^{MD}_{inter}(r)$. The resulting $G^{MD}_{intra}(r)$ and $G^{MD}_{inter}(r)$ for the Li:AN = 1:2 system are shown in **Figures 4.2c and d**, respectively, and those for the Li:AN = 1:0 system are shown in **Figures A4.6c and d**. $G^{MD}_{inter}(r)$ comprises several intermolecular interactions involving the Li$^+$–solvent, Li$^+$–FSA$^-$, Li$^+$–Li$^+$, solvent–FSA$^-$, FSA$^-$–FSA$^-$, and solvent–solvent correlations. Here, we focus on Li-ion coordination. We extracted the atom–atom pair

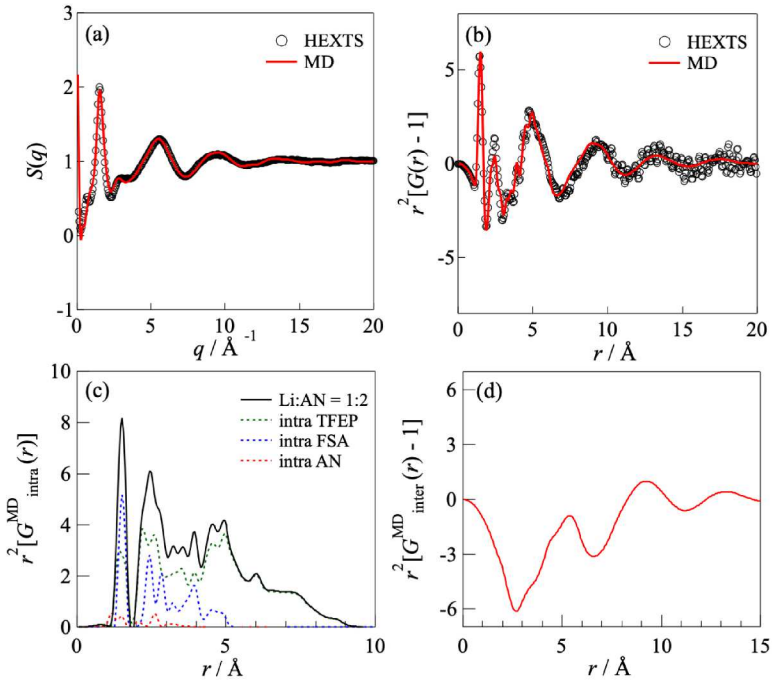

Figure 4.2 (a) X-ray structure factor, $S(q)$, and (b) X-ray radial distribution function in the $r^2[G(r) - 1]$ form obtained from HEXTS experiments (open circles) and MD simulations (solid lines) for the concentrated LiFSA/TFEP+AN solution (Li:AN = 1:2). Partial $G^{MD}(r)$s for the (c) intramolecular and (d) intermolecular contributions.

correlation functions, $g^{MD}_{X\text{-}Y}(r)$, for the Li^+–O_{tfep}, Li^+–O_{fsa}, and Li^+–N_{an} correlations for the Li^+–TFEP, Li^+–FSA^-, and Li^+–AN interactions, respectively, from the total $G^{MD}_{inter}(r)$. The resulting $g^{MD}_{Li–Otfep}(r)$, $g^{MD}_{Li–Ofsa}(r)$, and $g^{MD}_{Li–Nan}(r)$ values are shown in **Figures 4.3a and b**, together with the average coordination number, $N_{X\text{-}Y}(r)$, which was calculated by integrating the corresponding $g^{MD}_{X\text{-}Y}(r)$ up to a given value of r. In the binary LiFSA/TFEP solution (Li:AN = 1:0, **Figure 4.3a**), a major peak appeared at approximately 1.9 Å for both $g^{MD}_{Li–Otfep}(r)$ and $g^{MD}_{Li–Ofsa}(r)$. This was attributed to nearest neighbor Li^+–TFEP and Li^+–FSA interactions *via* O atoms in the first coordination sphere of the Li-ion. The corresponding $N_{Li\text{-}O}(r)$ values for the Li^+–O_{tfep} and Li^+–O_{fsa} interactions were estimated to be ~1.5 and ~3.0 (the plateau in $N_{X\text{-}Y}(r)$ at approximately r ~ 2.5 Å), respectively. However, no peak was observed during the Li^+–F_{tfep} and Li^+–F_{fsa} interactions ($g^{MD}_{Li–Ftfep}(r)$ and $g^{MD}_{Li–Ffsa}(r)$ in **Figures A4.8a and b**, respectively). This indicates that Li ions are coordinated with four or five O atoms, including one or two monodentate-coordinated TFEP and one or two bidentate-coordinated FSA, to form tetrahedral-type and/or specific five-coordinated Li-ion complexes with no F coordination as an averaged structure. A possible Li-ion complex is shown in **Figure 4.3c** (typical snapshot confirmed in the MD simulation box). As shown in this snapshot, Li ions are coordinated with two TFEP molecules and one FSA anion (bidentate formed by two O atoms) to form a mononuclear $[Li(TFEP)_2(FSA)_1]$ complex similar to the Li-ion complex in the corresponding dilute system (1.0 mol dm^{-3} LiFSA/TFEP), as reported in our previous study.[1] We thus conclude that it is difficult for Li ions to form an ionic-ordered structure based on multiple Li-ion complexes (or Li-ion aggregates) in the concentrated LiFSA/TFEP system; this differs from several concentrated electrolyte systems using conventional solvents.[18-21] Such unusual behavior is attributed to a "solvation steric effect" originating from the molecular size of TFEP;[3] i.e., steric repulsion between solvated TFEP molecules occurs within the solvation sphere of the Li-ion, preventing the formation of a packed multinuclear Li-ion complex. In the ternary LiFSA/TFEP+AN solution (Li:AN = 1:2, **Figure 4.3b**), the $N_{Li\text{-}Otfep}(r)$ decreased from 1.5 to 0.3 when a small-sized molecule, AN, was added to the LiFSA/TFEP solution. A major peak originating from Li^+–N (AN) interactions appeared at approximately 1.9 Å to yield a $N_{Li\text{-}Nan}(r)$ of 2.0. This suggests that the preferential solvation of Li ions with AN, rather than TFEP, occurred despite their similar Gutmann donor number (D_N), which is 14.1 in AN and 12.9 in TFEP.[2-3] Thus, most of the solvated TFEP molecules surrounding the Li-ion were desolvated and replaced with AN molecules to

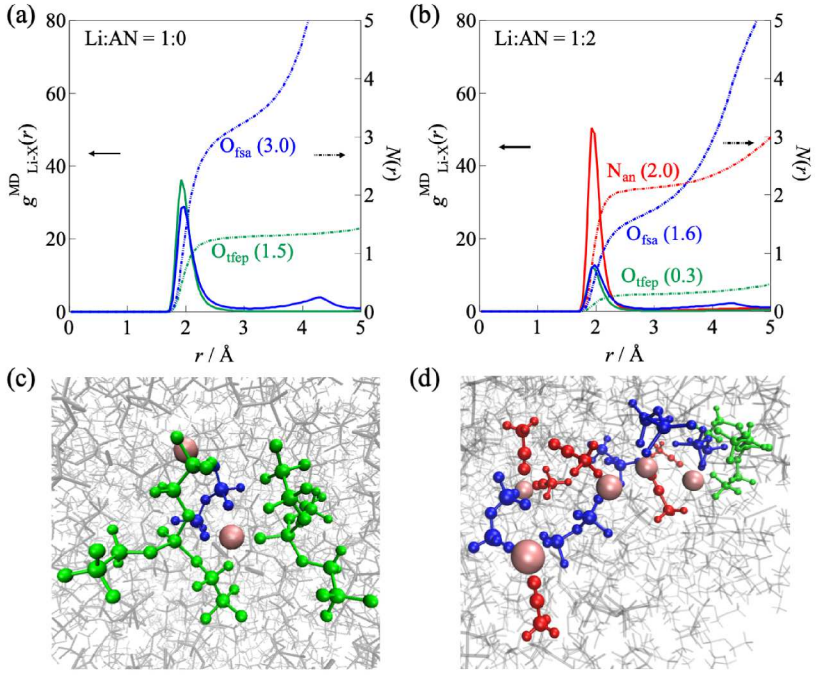

Figure 4.3 Atom–atom pair correlation functions [$g^{MD}_{Li\text{-}X}(r)$: left axis, solid lines] for O atoms of TFEP (green), O atoms of FSA (blue), and N atoms of AN (red) around Li ions, together with their integrated profiles (coordination number $N(r)$: right axis, dashed lines) for concentrated LiFSA/TFEP+AN solutions with Li:AN = (a) 1:0 and (b) 1:2. Typical snapshots confirmed in the MD simulation box for (c) 1:0 and (d) 1:2; pink: Li^+, blue: FSA^-, green: TFEP, and red: AN.

reduce steric repulsion between solvated TFEP molecules in Li-ion complexes. A similar decrease in $N(r)$ was also found in $N_{\text{Li-Ofsa}}(r)$; however, the coordinated FSA remained at $N_{\text{Li-Ofsa}}(r) = 1.6$ in the 1:2 solution, i.e., approximately half of the value for the 1:0 system (3.0). This can be explained by the ordering of Li ions *via* FSA and AN coordination to form packed multinuclear Li-ion complexes, as shown in **Figure 4.3d**. The multinuclear Li-ion complexes can be confirmed in the $g^{\text{MD}}_{\text{Li–Li}}(r)$ corresponding to Li^+-Li^+ correlations (**Figure A4.9**). In the Li:AN = 1:2 system, multiple sharp peaks appeared in the $g^{\text{MD}}_{\text{Li–Li}}(r)$ over relatively long distance (~20 Å); a clear peak was found at 3.4 Å (closest Li-Li correlation) and subsequent peaks continued at 6.33, 8.18, 11.1, and 16.8 Å. This strongly suggests that continuous Li ion-ordered structure is formed in the solution. The resulting ionic-ordered complex has a similar structure to that formed in concentrated binary LiTFSA/AN solutions with excellent LIB performance.[2, 8] Thus, we propose that (1) the formation of ionic-ordered structures is key to enabling LIB electrode reactions, and (2) the size of the solvent molecule (i.e., solvent bulkiness) is one of the most important factors for controlling this ordered structure in a concentrated electrolyte system.

To discuss the reductive/oxidative stability of the concentrated LiFSA/TFEP+AN solutions (Li:AN = 1:0 and 1:2), we performed DFT calculations on several Li^+-FSA^- complexes to evaluate their LUMO and HOMO energies. The Li^+–FSA^- complexes examined (complexes **2–5** in **Figure 4.4**) were units of multinuclear Li-ion complexes as confirmed in the MD simulation box. **Figure 4.4** shows the difference between the LUMO energies of Li–FSA complexes (**2–5**) and isolated FSA (**1**), i.e., $\Delta E_{\text{LUMO}} = E_{\text{LUMO\_complex}} - E_{\text{LUMO\_isoFSA}}$. The geometries of complexes **2** and **3–5** were chosen from MD snapshots of the Li:AN = 1:0 and 1:2 solutions, respectively, following optimization of their geometries *via* DFT calculations. The geometry of **1** originated from the geometrical optimization of the isolated FSA form.[22] ΔE_{LUMO} significantly decreased with increasing numbers of Li ions (n_{Li}) coordinated around a central FSA: **2** ($n_{\text{Li}} = 1$) > **3**, **4**, **5** ($n_{\text{Li}} = 2$), suggesting that the LUMO energy levels of FSA were further stabilized by the formation of multinuclear complexes (or aggregates) with larger values of n_{Li}. The ΔE_{LUMO} values for **3–5** (found for the Li:AN = 1:2 solution) are appreciably lower than those of the Li^+-solvent complexes (i.e., Li^+-TFEP and Li^+-AN complexes), as shown in **Figure A4.10**. These lower LUMO values result in the preferential reductive decomposition of FSA anions, rather than solvent components (TFEP and AN), during the charging process. Indeed, in the CV profiles of the LiFSA/TFEP+AN system (**Figure 4.1b and c**), we observed a small reductive current at approximately 1.0 V during the first cycle, which can be assigned to FSA decomposition and the consequent formation of FSA-based SEI on the graphite electrode. In contrast, the ΔE_{LUMO} value for complex **2** (for the binary LiFSA/TFEP solution) was similar to that of Li^+-solvent complexes, implying no preferential decomposition of the FSA component and no SEI formation in the binary solution (**Figure 4.1a**). A similar trend was found for HOMO energy levels (**Figure A4.11**), i.e., ΔE_{HOMO} decreased with increasing n_{Li}, resulting in wider experimental oxidative stability (**Figure A4.2**, ~5.5 V) in the concentrated LiFSA/TFEP+AN solution. Thus, we conclude that the formation of ionic-ordered complexes, i.e., ionic aggregates including several Li and FSA ions, plays a crucial role in the electrode reaction. In this study, this is reflected by the Li-ion insertion/deinsertion reaction on the graphite electrode.

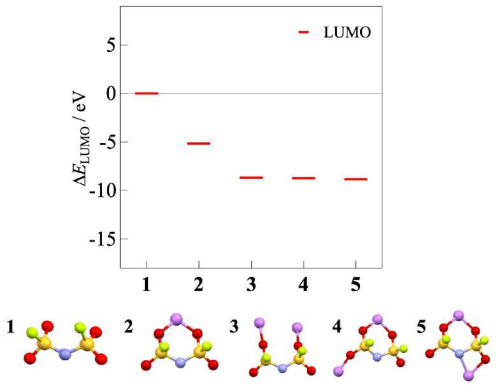

Figure 4.4 ΔE_{LUMO} values for the Li^+–FSA^- complexes calculated using DFT calculations.

4.3.3 *Electrode/electrolyte interface structures*

Finally, we performed *in situ* SEIRAS to discuss the relationships between ionic-ordered structures in the bulk electrolyte and at the electrode/electrolyte interface. *In situ* SEIRAS revealed that the Li-ion complex structure in the bulk electrolyte dictates the reaction at the electrode/electrolyte interface, including the formation of SEI *via* the reductive decomposition of electrolyte components. **Figures 4.5a and b** show typical SEIRA spectra obtained during LSV in the potential range of 3.0–0.5 V vs. Li/Li^+, obtained from the concentrated LiFSA/TFEP+AN solutions with Li:AN = 1:0 and 1:2. The corresponding LSV profiles are shown in **Figure 4.5c**. The SEIRAS spectra shown herein correspond to the difference spectra obtained by subtracting the reference spectrum at 3.0 V from that measured at a given potential (E).

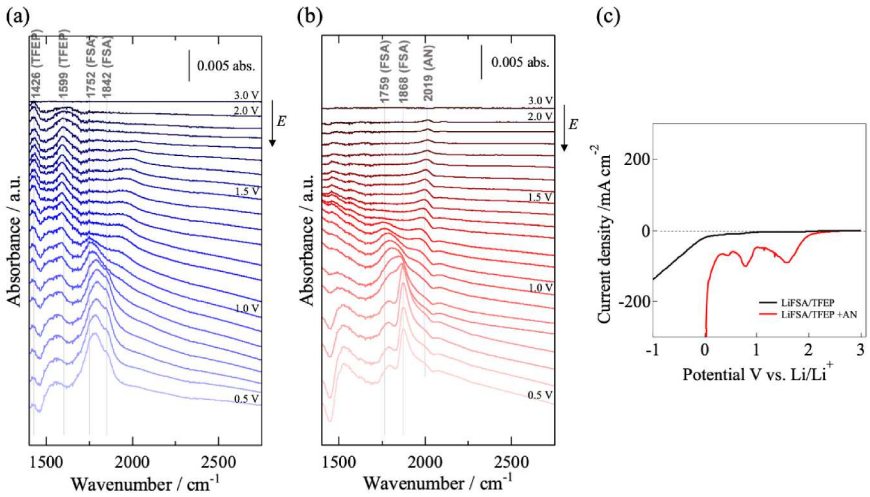

Figure 4.5 Typical *in situ* SEIRAS obtained during linear sweep voltammetry (LSV) in a potential *E* range of 3.0 V to 0.5 V in the concentrated LiFSA/TFEP+AN solutions with (a) Li:AN = 1:0 and (b) 1:2., together with (c) the corresponding LSV profiles (scan rate: 0.2 mV s^{-1}).

In the Li:AN = 1:0 solution (LiFSA/TFEP without AN), a small peak was observed at 1426 cm^{-1} when *E* was decreased, the intensity of which remained unchanged down to a potential of around 0.5 V. This peak can be assigned to a partially decomposed TFEP component in the vicinity of the electrode for the reason that our ATR-IR spectra for the bulk LiFSA/TFEP electrolyte and neat TFEP (**Figure A4.12a**) showed a sharp IR peak at 1424 cm^{-1}, assigned to TFEP molecules. The 1599 cm^{-1} peak showed similar potential-dependence to the 1426 cm^{-1} peak. We thus tentatively assign the 1599 cm^{-1} peak to the reductive decomposition product of TFEP, since no corresponding peak was observed in the ATR-IR spectra of the bulk components (**Figure A4.12a**). The small reductive current observed from 2.0 to 0 V in the LSV of the Li:AN = 1:0 solution (**Figure A4.12c**, black line) further supports the reductive decomposition of TFEP. At potentials below ~1.2 V, a small peak appeared at 1752 cm^{-1}, which is attributed to the FSA anion according to the ATR-IR spectra for the bulk system (**Figure A4.12**; LiFSA/TFEP+AN and FSA-based ionic liquid). This observation indicates the approach of the FSA anion to the electrode/electrolyte interface below ~1.2 V. We note the clear blueshift of the peak to 1842 cm^{-1} at *E* = 1.0 V and the increase in peak intensity when *E* is further lowered to 0.5 V. This observation may also indicate the reductive decomposition of FSA anions at the electrode surface.

In the Li:AN = 1:2 solution (LiFSA/TFEP+AN, **Figure 4.5b**), we found no peak from TFEP molecules around 1426 and 1599 cm^{-1} throughout the potential range examined, which is notably different from the Li:AN = 1:0 solution. This strongly suggests that no TFEP molecules are present near the electrode/electrolyte interface in the Li:AN = 1:2 system. Based on HEXTS and MD results, Li ions form ordered Li-ion complexes composed of both FSA and AN in the concentrated LiFSA/TFEP+AN solution; in other words, the complexes include very few TFEP molecules in their coordination sphere following the addition of AN. This result indicates a strong relationship between the electrode/electrolyte interface structure and Li-ion complex structures in the bulk electrolyte. The small peak appearing at 2019 cm^{-1} at 2.0 V can be attributed to the C≡N stretching vibration of AN (see **Figure A4.12**); this remained until ~1.5 V. Its peak wavenumber gradually redshifted to 1973 cm^{-1} when the potential was decreased from 1.5 V to 1.0 V, suggesting the decomposition of AN. A reductive current was identified in LSV within the potential range of 2.0–1.0 V (**Figure 4.5c**, red line); we thus assign the 1973 cm^{-1} peak to the decomposition products of AN, such as $H_2C{=}C{=}NH$,[23] which form at the electrode surface.

A small peak around 1759 cm^{-1} appeared at 1.3 V, and split into two peaks (1759 cm^{-1} and 1868 cm^{-1}) as the potential decreased to 1.0 V. This observation was similar to that of the Li:AN = 1:0 solution (**Figure 4.5a**), suggesting that a similar reductive decomposition of FSA anions occurred in the Li:AN = 1:2 solution. A notable difference was observed at potentials below 1.0 V, where a sharp peak appeared at 1868 cm^{-1} in the AN-contained system. We assign this peak, at 1868 cm^{-1}, to further decomposed FSA products, which can only form in the presence of AN. As discussed above, a similar reductive current is seen in this *E* range (1.0–0.5 V) for the CV profile shown in **Figure 4.1c**, which is due to the decomposition of the FSA component in the electrolytes, i.e., FSA-derived SEI formation. A similar reduction was noted in LSV (1.0–0.5 V; **Figure 4.5c**, red line);

hence, we conclude that the 1759 cm^{-1} peak corresponds to the pre-decomposition product of FSA formed on the electrode, whereas the 1868 cm^{-1} peak (1.0–0.5 V) reflect FSA after further decomposition, resulting in a stable FSA-derived SEI.

4.4 Conclusions

We designed a Li-ion-ordered structure in nonflammable concentrated electrolytes in order to facilitate the LIB electrode reaction. By adding a small molecular additive (AN) into the concentrated LiFSA electrolytes using a large-molecule TFEP solvent, the electrode reaction drastically improved, exhibiting reversible charge/discharge behavior. Based on combined HEXTS experiments using all-atom MD simulations, we demonstrated a structural change from a mononuclear Li-ion complex structure (without AN) to a Li-ion-ordered structure linked *via* FSA anions as a function of the addition of AN. The formation of this ordered structure reduced the LUMO energy of FSA, resulting in FSA-derived stable SEI formation at the negative graphite electrode. *In situ* SEIRAS spectra demonstrated that (1) the electrode/electrolyte interface structure in the binary LiFSA/TFEP system significantly changed with the addition of AN, and (2) the interface environment reflects the Li-ion complex structure in the bulk phase. Furthermore, we confirmed changes in the reductive decomposition of the electrolyte; FSA anions decomposed in two steps in AN-contained systems, whereas only the first step was observed in the situation without AN. This change can be attributed to differences in the preceding electrode reaction, including the decomposition of TFEP, derived from the change in the Li-ion complex structure in the bulk phase following the addition of AN.

4.5 References

(1) Sawayama, S.; Todorov, Y. M.; Mimura, H.; Morita, M.; Fujii, K. Fluorinated alkyl-phosphate-based electrolytes with controlled lithium-ion coordination structure. *Phys. Chem. Chem. Phys.* **2019,** *21*, 11435-11443.

(2) Sogawa, M.; Sawayama, S.; Han, J.; Satou, C.; Ohara, K.; Matsugami, M.; Mimura, H.; Morita, M.; Fujii, K. Role of Solvent Size in Ordered Ionic Structure Formation in Concentrated Electrolytes for Lithium-Ion Batteries. *J. Phys. Chem. C* **2019,** *123*, 8699-8708.

(3) Sogawa, M.; Todorov, Y. M.; Hirayama, D.; Mimura, H.; Yoshimoto, N.; Morita, M.; Fujii, K. Role of Solvent Bulkiness on Lithium-Ion Solvation in Fluorinated Alkyl Phosphate-Based Electrolytes: Structural Study for Designing Nonflammable Lithium-Ion Batteries. *J. Phys. Chem. C* **2017,** *121*, 19112-19119.

(4) Todorov, Y. M.; Aoki, M.; Mimura, H.; Fujii, K.; Yoshimoto, N.; Morita, M. Thermal and electrochemical properties of nonflammable electrolyte solutions containing fluorinated alkylphosphates for lithium-ion batteries. *J. Power Sources* **2016,** *332*, 322-329.

(5) Fujii, K.; Wakamatsu, H.; Todorov, Y.; Yoshimoto, N.; Morita, M. Structural and Electrochemical Properties of Li Ion Solvation Complexes in the Salt-Concentrated Electrolytes Using an Aprotic Donor Solvent, *N,N*-Dimethylformamide. *J. Phys. Chem. C* **2016,** *120*, 17196-17204.

(6) McOwen, D. W.; Seo, D. M.; Borodin, O.; Vatamanu, J.; Boyle, P. D.; Henderson, W. A. Concentrated electrolytes: decrypting electrolyte properties and reassessing Al corrosion mechanisms. *Energy Environ. Sci.* **2014,** *7*, 416-426.

(7) Wang, J.; Yamada, Y.; Sodeyama, K.; Chiang, C. H.; Tateyama, Y.; Yamada, A. Superconcentrated electrolytes for a high-voltage lithium-ion battery. *Nat. Commun.* **2016,** *7*, 12032-12040.

(8) Yamada, Y.; Furukawa, K.; Sodeyama, K.; Kikuchi, K.; Yaegashi, M.; Tateyama, Y.; Yamada, A. Unusual Stability of Acetonitrile-Based Superconcentrated Electrolytes for Fast-Charging Lithium-ion Batteries. *J. Am. Chem. Soc.* **2014,** *136*, 5039-5046.

(9) Yamada, Y.; Usui, K.; Chiang, C. H.; Kikuchi, K.; Furukawa, K.; Yamada, A. General observation of lithium intercalation into graphite in ethylene-carbonate-free superconcentrated electrolytes. *ACS Apppl. Mater. Interfaces* **2014,** *6*, 10892-10899.

(10) Aurbach, D. Review of selected electrode–solution interactions which determine the performance of Li and Li ion batteries. *J. Power Sources* **2000,** *89*, 206-218.

(11) Aurbach, D.; Zaban, A.; Ein-Eli, Y.; Weissman, I. Recent studies on the correlation between surface chemistry, morphology, three-dimensional structures and performance of Li and Li-C intercalation anodes in several important electrolyte systems. *J. Power Sources* **1997,** *68*, 91-98.

(12) Dahn, J. R. Phase diagram of Li_xC_6. *Phys. Rev. B* **1991,** *44*, 9170-9177.

(13) Ohzuku, T.; Iwakoshi, Y.; Sawai, K. Formation of Lithium-Graphite Intercalation Compounds in Nonaqueous Electrolytes and Their Application as a Negative Electrode for a Lithium Ion (Shuttlecock) Cell. *J. Electrochem. Soc.* **1993,** *140*, 2490-2498.

(14) Dahbi, M.; Ghamouss, F.; Tran-Van, F.; Lemordant, D.; Anouti, M. Comparative study of EC/DMC LiTFSI and $LiPF_6$ electrolytes for electrochemical storage. *J. Power Sources* **2011,** *196*, 9743-9750.

(15) Li, L.; Zhou, S.; Han, H.; Li, H.; Nie, J.; Armand, M.; Zhou, Z.; Huang, X. Transport and Electrochemical

Properties and Spectral Features of Non- Aqueous Electrolytes Containing LiFSI in Linear Carbonate Solvents. *J. Electrochem. Soc.* **2011,** *158*, A74-A82.
(16) Takekawa, T.; Kamiguchi, K.; Imai, H.; Hatano, M. Physicochemical and Electrochemical Properties of the Organic Solvent Electrolyte with Lithium Bis(fluorosulfonyl)Imide (LiFSI) As Lithium-Ion Conducting Salt for Lithium-Ion Batteries. *ECS Trans.* **2015,** *64*, 11-16.
(17) Uchida, S.; Ishikawa, M. Lithium bis(fluorosulfonyl)imide based low ethylene carbonate content electrolyte with unusual solvation state. *J. Power Sources* **2017,** *359*, 480-486.
(18) Fujii, K.; Matsugami, M.; Ueno, K.; Ohara, K.; Sogawa, M.; Utsunomiya, T.; Morita, M. Long-Range Ion-Ordering in Salt-Concentrated Lithium-Ion Battery Electrolytes: A Combined High-Energy X-ray Total Scattering and Molecular Dynamics Simulation Study. *J. Phys. Chem. C* **2017,** *121*, 22720-22726.
(19) Miyazaki, K.; Takenaka, N.; Watanabe, E.; Iizuka, S.; Yamada, Y.; Tateyama, Y.; Yamada, A. First-Principles Study on the Peculiar Water Environment in a Hydrate-Melt Electrolyte. *J. Phys. Chem. Lett.* **2019,** *10*, 6301-6305.
(20) Sodeyama, K.; Yamada, Y.; Aikawa, K.; Yamada, A.; Tateyama, Y. Sacrificial Anion Reduction Mechanism for Electrochemical Stability Improvement in Highly Concentrated Li-Salt Electrolyte. *J. Phys. Chem. C* **2014,** *118*, 14091-14097.
(21) Yamada, Y.; Yamada, A. Superconcentrated Electrolytes to Create New Interfacial Chemistry in Non-aqueous and Aqueous Rechargeable Batteries. *Chemistry Letters* **2017,** *46*, 1065-1073.
(22) Fujii, K.; Seki, S.; Fukuda, S.; Kanzaki, R.; Takamuku, T.; Umebayashi, Y.; Ishiguro, S.-i. Anion Conformation of Low-Viscosity Room-Temperature Ionic Liquid 1-Ethyl-3-methylimidazolium Bis(fluorosulfonyl) Imide. *J. Phys. Chem. B* **2007,** *111*, 12829-12833.
(23) Ito, F.; Nakanaga, T.; Sugawara, K.-i.; Takeo, H.; Sugie, M.; Matsumura, C. Observation of the High-Resolution Infrared Spectrum of the ν_4 Band of Ketenimine, CH_2CNH. *J. Mol. Spectrosc.* **1990,** *140*, 177-184.

4.6 Appendix

Table A4.1 Molar ratio (Li salt:solvent), molarities (LiFSA concentration, c_{Li}), and density (d) for binary LiFSA/TFEP and ternary LiFSA/TFEP+AN solutions.

LiFSA/TFEP system		
LiFSA:TFEP	c_{Li} / mol dm^{-3}	d / g cm^{-3}
1:1.5	2.50	1.704

LiFSA/TFEP system		
LiFSA:TFEP:AN	c_{Li} / mol dm^{-3}	d / g cm^{-3}
1:1.1:1.0	2.50	1.530
1:0.9:2.0	2.50	1.484

Table A4.2 Compositions (number of ion-pairs and solvents) and calculated densities (d) for the MD simulations (concentrated LiFSA/TFEP+AN with Li/AN (by mol.) = 1:0 and 1:2).

Li:AN	Li-FSA	TFEP	AN	d / g cm^{-3}	
				MD	Exp.
1:0	304	496	–	1.761	1.704
1:2	338	324	689	1.417	1.484

[a] Value obtained from the present MD simulations. [b] Experimental values.

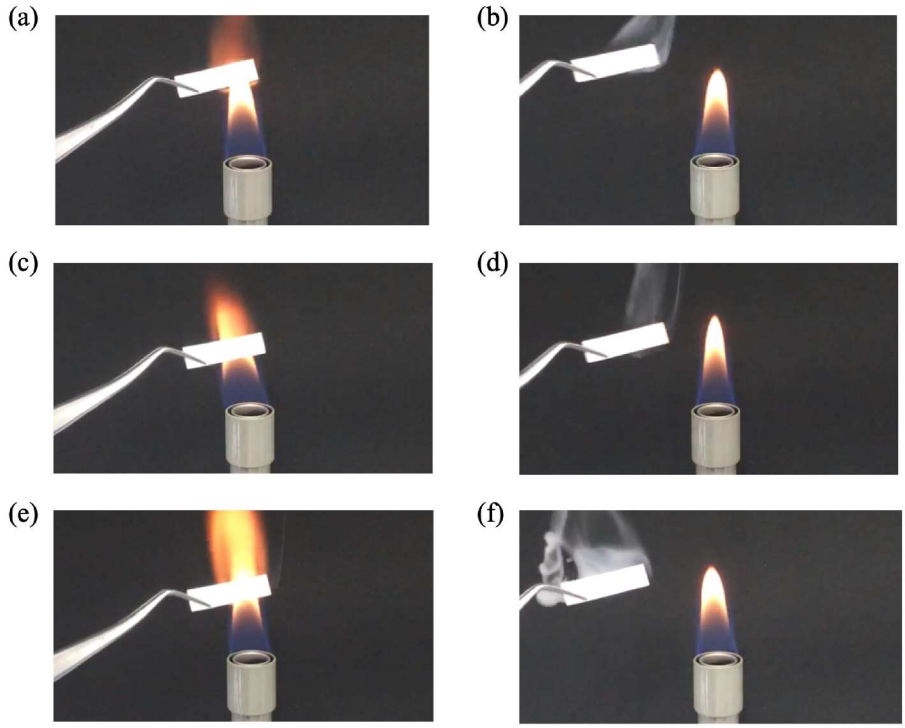

Figure A4.1 Flame tests of the concentrated LiFSA/TFEP+AN solutions with Li/AN (by mol.) = (a, b) 1:0, (c, d) 1:1, and (e, f) 1:2, before and after exposing to flame.

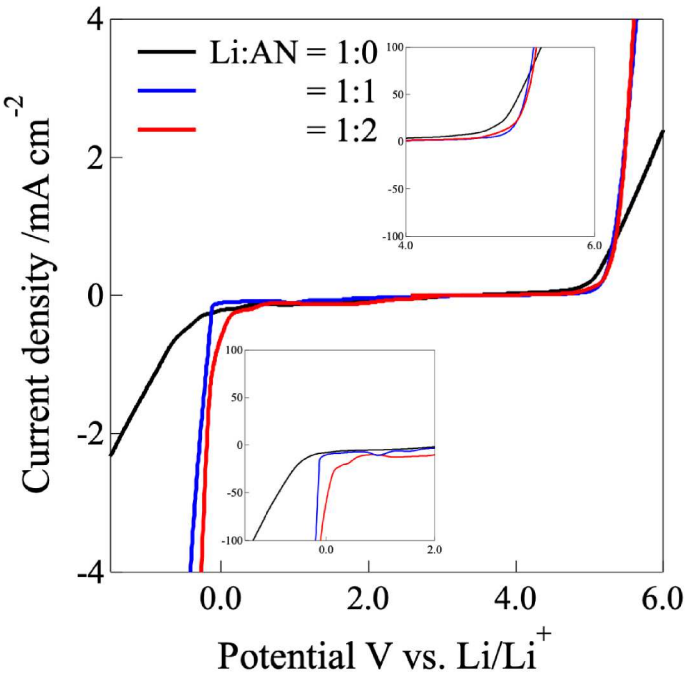

Figure A4.2 Electrochemical windows for the concentrated LiFSA/TFEP+AN solutions (Li:AN = 1:0, 1:1, and 1:2) at a scan rate of 5.0 mV s^{-1} (298 K).

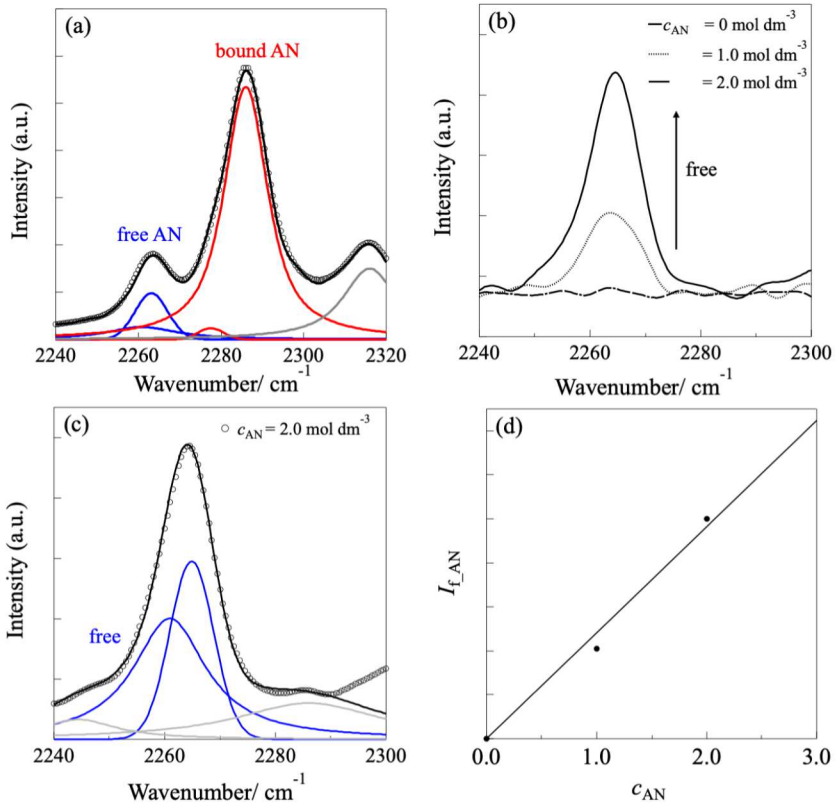

Figure A4.3 (a) Peak deconvolution (free AN: blue, bound AN: red) of the observed Raman spectrum for the concentrated LiFSA/TFEP+AN solution (Li/AN = 1:2). (b) Raman spectra for the TFEP+AN mixed solutions (without LiFSA salt) with c_{AN} = 0, 1.0, and 2.0 mol dm^{-3} and (c) the typical peak deconvolution for c_{AN} = 2.0 mol dm^{-3} solution. (d) The integrated intensities of the two free AN bands, I_{f_AN} (= I_{2261} + I_{2265}) plotted against c_{AN}.

Determination of free AN concentration (c_{f_AN}): To determine the concentration of free AN (c_{f_AN}) in concentrated electrolytes, we measured Raman spectrum of the 2.5 mol dm^{-3} LiFSA/TFEP+AN (Li/AN = 1:2) and performed a least-squares curve fitting analysis[13-14] (**Figure A4.3a**). The Raman spectrum were represented mainly by four components: two bands at 2261.0 and 2265.0 cm^{-1} (blue lines) corresponding to the free AN (C≡N stretching mode) and two bands at 2277.5 and 2285.0 cm^{-1} (red lines) to the AN bound to Li ion (i.e., bound AN).[15-16] Using the integrated intensities of the two free bands, I_f (= I_{2261} + I_{2265}), we could calculate the concentration of the free AN (c_{f_AN}) based on the following relation: $I_f = J_{f\_AN}\, c_{f\_AN}$, where J_{f_AN} is the Raman scattering coefficient. In this work, the J_{f_AN} was determined separately as 0.48 from the additional Raman experiments for the mixed solutions of TFEP and AN, which is described below. The c_{f_AN} (=I_{f_AN} / J_{f_AN} (= 0.48)) values were 1.1 mol dm^{-3} and 22% of the total AN concentration.

Determination of J_{f_AN} value: To determine J_{f_AN} value, we measured separately Raman spectra of TFEP+AN mixed solutions (without LiFSA salt) with c_{AN} = 0, 1.0, and 2.0 mol dm^{-3} (**Figure A4.3b**). The 2265 cm^{-2}-peak (C≡N stretching) increased linearly in intensity with c_{AN}, which could be assigned to the free AN owing to very weak intermolecular interactions between TFEP and AN. The observed spectra were represented using two free AN bands (typical result for c_{AN} = 2.0 mol dm^{-3}, **Figure A4.3c**). The integrated intensities of the two free AN bands, I_{f_AN} (= I_{2261} + I_{2265}) were plotted against c_{AN} (**Figure A4.3d**)) to be linear relation; then, we determined the J_{f_AN} value from the slope according to the following relation: $I_{f\_AN} = J_{f\_AN}\, c_{f\_AN}$. The J_{f_AN} value was determined to be 0.48.

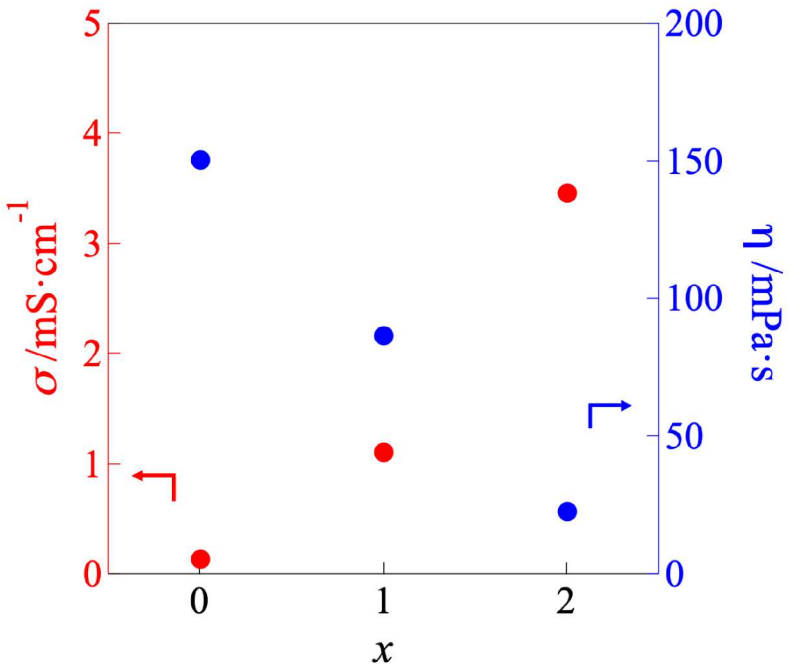

Figure A4.4 CV profiles for graphite electrodes in concentrated LiFSA/TFEP+AN solutions (Li:AN = (a) 1:0, (b) 1:1, and (c) 1:2 (scan rate: 0.2 mV s^{-1}). (d) Charge–discharge curves for the graphite electrode in the concentrated LiFSA/TFEP+AN solution with Li:AN = 1:2 at a 0.1 C rate. (e) Cycling performance (red, left axis) and coulomb efficiency (blue, right axis) of the same solution.

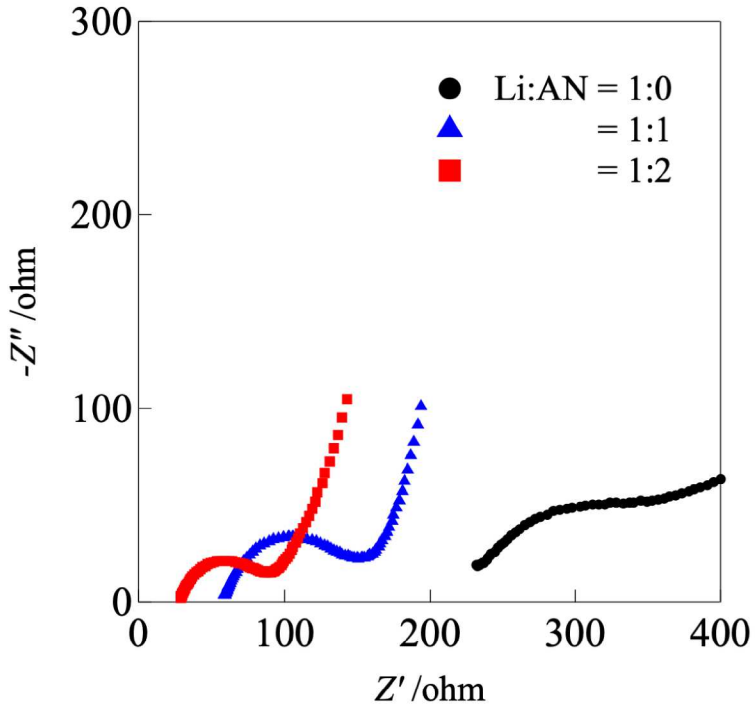

Figure A4.5 Nyquist plots for the three-electrode cells using graphite test electrode (at open circuit potential) in the concentrated LiFSA/TFEP + AN solutions (Li/AN = 1:0, 1:1, and 1:2).

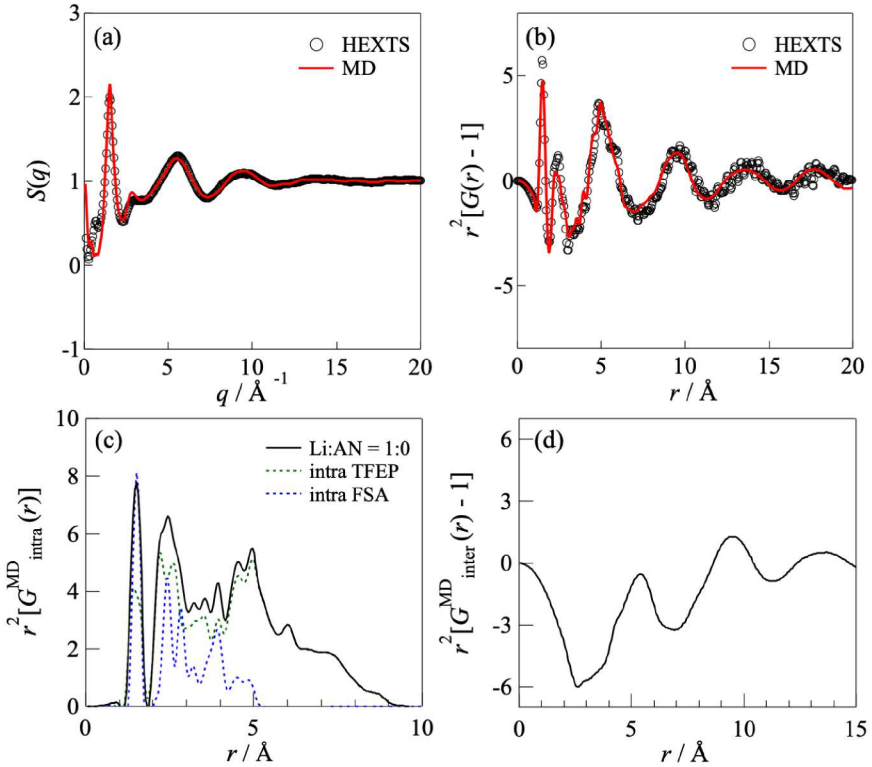

Figure A4.6 (a) $S(q)$, and (b) X-ray radial distribution function in the $r^2[G(r) - 1]$ form obtained from HEXTS experiments (open circles) and MD simulations (solid lines) for the concentrated LiFSA/TFEP solution (Li:AN = 1:0). Partial $G^{MD}(r)$s for the (c) intramolecular and (d) intermolecular contributions.

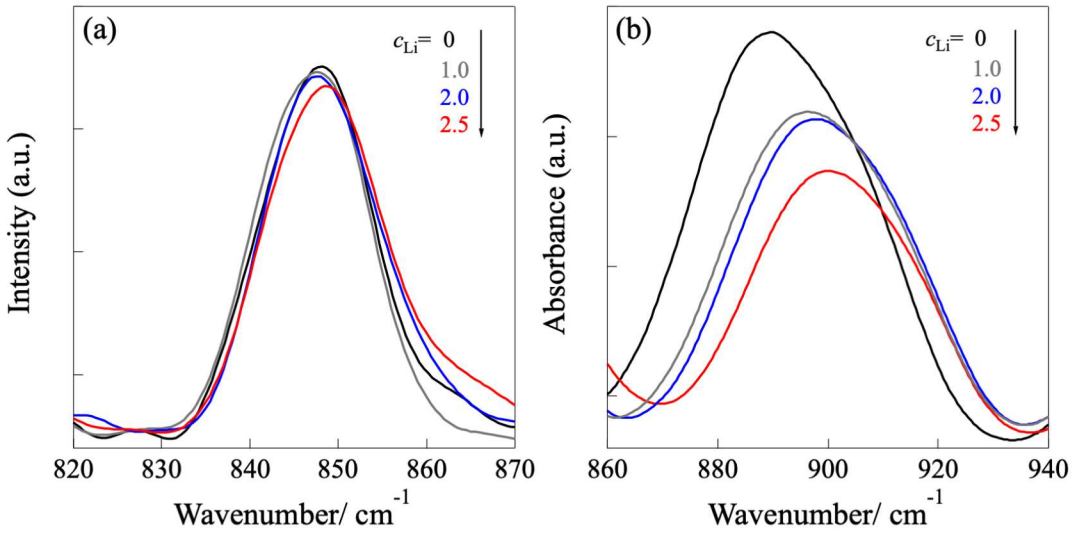

Figure A4.7 (a) Raman and (b) IR spectra observed for concentrated LiFSA/TFEP solutions with *c*Li = 0, 1.0, 2.0, and 2.5 mol dm^{-3}.

No c_{Li} dependence of the Raman band [O-P-O asymmetric stretching mode of TFEP] was observed. This indicated that Raman spectra were not suitable to investigate the TFEP-based solutions. This is because the Raman bands of TFEP are less sensitive to Li-ion solvation, i.e., no observation of the peak shift originating from "free TFEP" to "bound TFEP". We further tried to obtain experimental support and measure the IR spectra since we successfully determined the Li-ion complex structure by IR technique in our previous work (dilute system, c_{Li} <1.0 mol dm^{-3}). However, the IR spectra originating from the TFEP (860-930 cm^{-1}) turned out to be overlapped with many bands. Furthermore, increasing c_{Li} made the spectra broader and more complicated, making it unable to analyze using a conventional peak-deconvolution based on a least-squares fitting in the concentrated system. It is thus difficult to determine the Li ion complex structure via Raman and IR investigations.

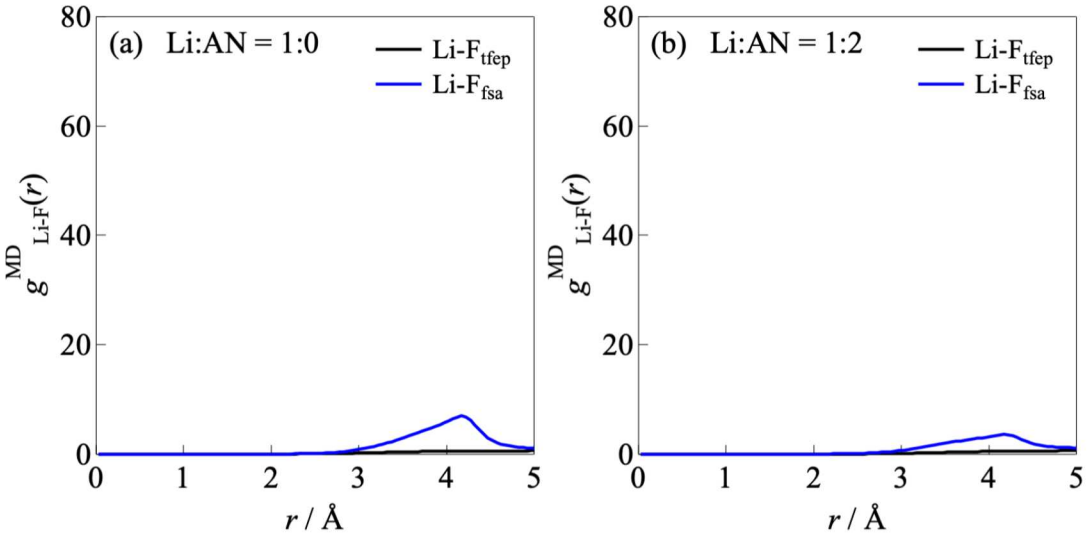

Figure A4.8 Atom-atom pair correlation functions [$g^{MD}_{Li-F}(r)$, solid lines] for the F atoms of TFEP (black) and the F atoms of FSA (blue) around the Li ions for the concentrated LiFSA/TFEP+AN solutions with (a) Li/AN = 1:0 and (b) Li/AN = 1:2.

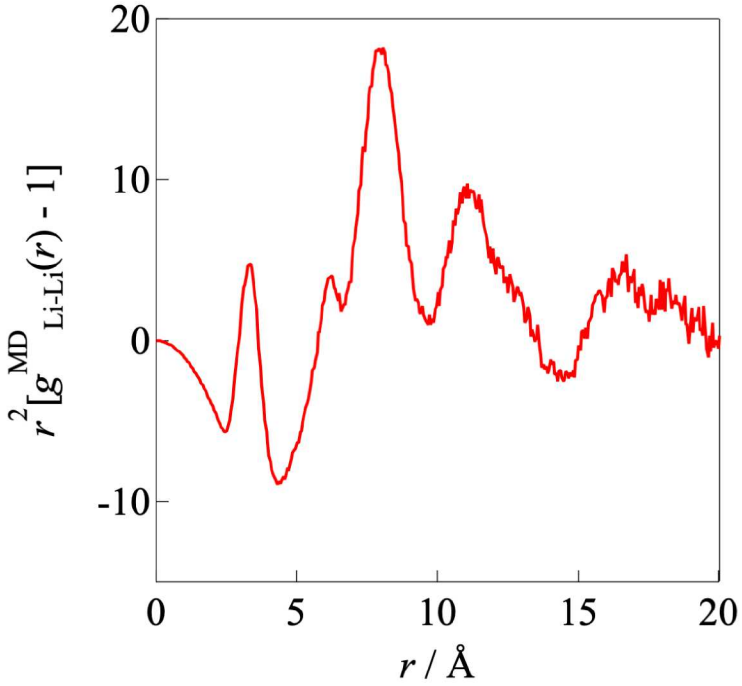

Figure A4.9 Atom-atom pair correlation functions between Li ions, $r^2[g^{MD}_{Li\text{-}Li}(r) - 1]$ for the concentrated LiFSA/TFEP+AN solution with Li/AN = 1:2.

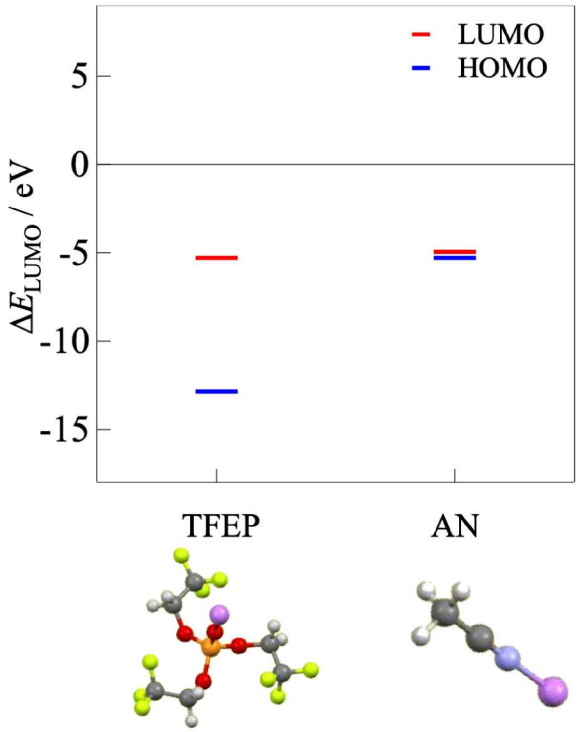

Figure A4.10 ΔE_{LUMO} values for the Li^+–FSA^- complexes calculated using DFT calculations.

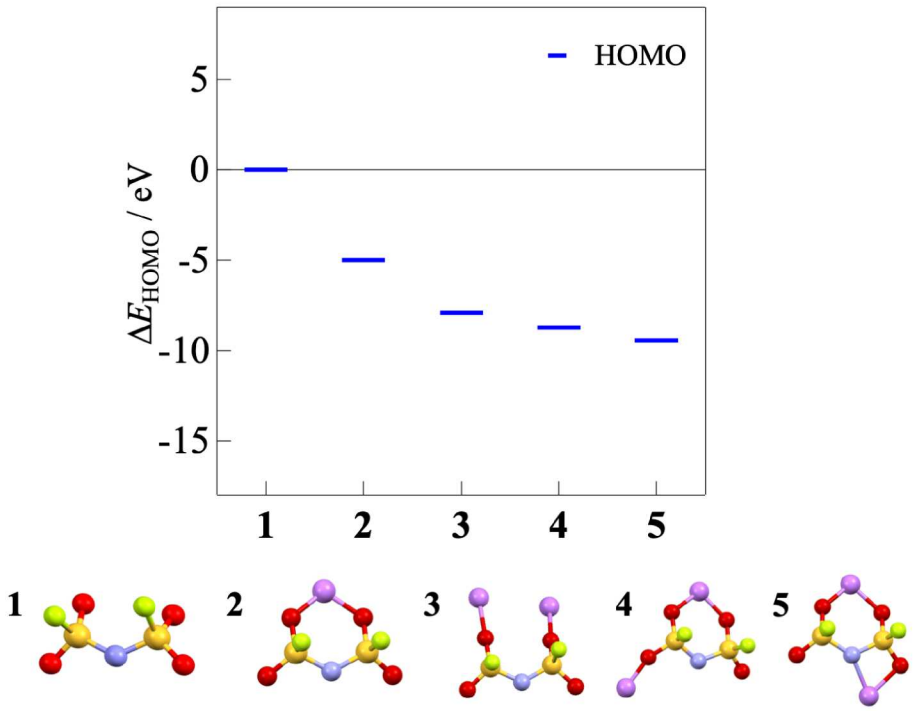

Figure A4.11 ΔE_{HOMO} values for the Li^+–FSA^- complexes calculated using DFT calculations.

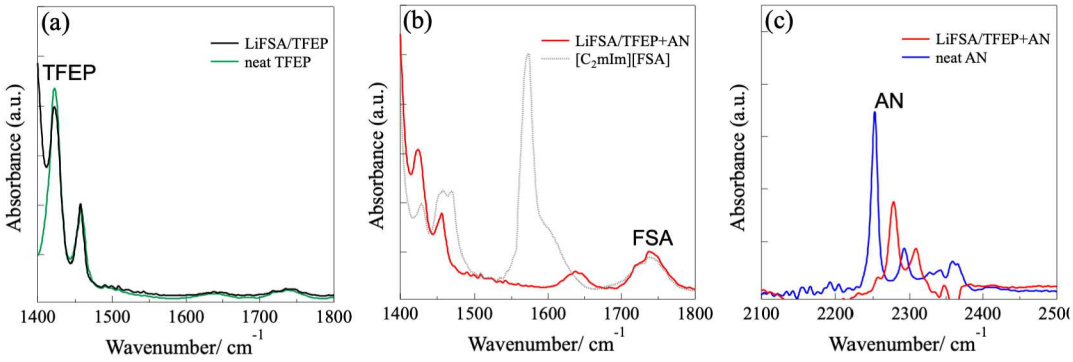

Figure A4.12 Typical *in situ* SEIRAS obtained during linear sweep voltammetry (LSV) in a potential *E* range of 3.0 V to 0.5 V in the concentrated LiFSA/TFEP+AN solutions with (a) Li:AN = 1:0 and (b) 1:2., together with (c) the corresponding LSV profiles (scan rate: 0.2 mV s^{-1}).

Chapter 5

2,2,2-Trifluoroethyl Acetate as an Electrolyte Solvent for Lithium-Ion Batteries: Effect of Weak Solvation on Electrochemical and Structural Characteristics

5.1 Introduction

Ion–solvent interaction (i.e., solvation) directly affects the solubility and dissociativity of salts in solution to control the ion transport and electrochemical properties of energy storage devices, such as LIBs. In general, solvent properties, such as permittivity, viscosity, and hydrophobicity/hydrophilicity, are useful for designing the ionic conductivity of electrolyte solutions. Particularly, the Gutmann donor number (D_N), which corresponds to the electron-pair donating ability to metal ions, and the Gutmann acceptor number (A_N), which indicates affinity to anions,[1-3] play a key role in electrolyte design for battery applications. Solvents with higher D_N values lead to full ion dissociation to yield successfully solvated metal ions and counter-anions, whereas solvents with lower D_N values cause ions to form contact ion-pairs due to low solvation power, resulting in poor ionic conductivity and battery performance. Furthermore, I pointed out in Chapters 3 and 4 that solvent bulkiness (molecular size of the solvent) is an important factor in controlling ion solvation; specifically, a bulky solvent tends to reduce the solvation number of the metal ion to induce ion-pair formation in the electrolyte solution.[4-8]

In conventional LIB systems, carbonate-based organic solvents are necessary to achieve stable and reversible working LIBs with a graphite negative electrode, as mentioned in Introduction.[9-10] This is because the carbonate components (particularly, EC) form a SEI via their reductive decomposition during the first charging process, allowing reversible Li-ion insertion into the graphite electrode and suppressing further decomposition of the electrolytes.[11-14] SEI formation on negative electrodes is also compassable in other organic solvents and ionic liquids when a small amount of EC or vinylene carbonate is added into their electrolyte solutions.[15-16] In this case, the EC component with low content acts as an SEI additive; in contrast, Li ions are solvated primarily by main solvents (organic solvents or ionic liquids) to form solvated Li-ion complexes in the bulk. In solvents yielding weak solvation (i.e., lower D_N value), Li-X ion pairs (X: counter-anion) are formed, which reduce the ionic conductivity. In contrast, desolvation of Li ions at the electrode/electrolyte interface, which has been proposed as a rate-controlling process of charge transfer of the graphite insertion reaction,[17-19] easily occurs. The reverse may occur in higher-D_N solvents exhibiting strong Li-ion solvation.

In this work, among fluorinated solvents, 2,2,2-trifluoroethyl acetate (TFEAc), which has the small molecular size (147.5 Å^3) relative to the TFEP solvent (Chapter 3 and 4), and weak coordination power was selected as a main solvent to investigate the effects of these solvent properties on ion solvation and electrode reaction characteristics. Doi et al. reported that the highly concentrated electrolytes using TFEAc exhibited superior charge/discharge performance for a certain positive electrode (i.e., $LiNi_{0.8}Co_{0.1}Mn_{0.1}O_2$) for LIBs.[20] In this work, I demonstrated that the TFEAc-based electrolyte solutions containing Li salts (c_{Li} <1.0 mol dm^{-3}) exhibited poor ion conduction and electrode reaction properties due to ion-pair formation caused by weak solvation; however, the graphite electrode reaction with high-rate performance was successfully achieved when a small amount of EC additive was used. I discussed the relationship between the solvation and electrode reaction from structural and electrochemical aspects.

5.2 Experimental

5.2.1 *Materials*

I prepared binary LiTFSA/TFEAc solutions and ternary LiTFSA/TFEAc+EC solutions (mole fraction of EC to TFEAc-EC mixture, x_{EC} = 0.02, 0.1, and 0.5) with varying c_{Li} (0–1.0 mol dm^{-3}). The x_{EC} = 0.02, 0.1, and 0.5 correspond to 1 wt%, 5 wt%, and 30 wt% EC in the solutions.

5.2.2 *Experimental*

The binding energy ΔE_{bind} was calculated as the SCF energy difference between the Li-TFEAc (1:1) complex and its individual components (Li^+ and TFEAc) according to $\Delta E_{bind} = E_{SCF}$ (complex) $- E_{SCF}$ (Li^+) $- E_{SCF}$ (TFEAc) and then corrected by the basis set superposition error using the counterpoise method,[21] which is described in detail in **Appendix** (**Figure A5.1**).

5.3 Results and Discussion

5.3.1 *Electrochemical properties*

As is well known, an ion–solvent interaction (i.e., solvation) plays a crucial role in designing the electrochemical and ion-conducting properties of electrolytes. The Gutmann donor number D_N of solvents, which corresponds to the electron-pair donating ability to bind to a metal ion, is an effective measure to predict ion–solvent interactions and solvation power. In previous work, I proposed a simple D_N prediction method using the binding energy ΔE_{bind} obtained from DFT calculations for the Li^+-solvent (1:1) complex. To verify the electron-pair donating ability of a new solvent, TFEAc, I first performed DFT calculations for the Li^+-TFEAc (1:1) complex, and the optimized complex geometry and ΔE_{bind} value are displayed in **Appendix**, **Figure A5.1** I can observe that the TFEAc molecule binds to the Li ion via the O atom (O=CH_2 moiety), resulting in ΔE_{bind} = 161.1 kJ mol^{-1}. Using the linear relation between D_N and ΔE_{bind}, the D_N value of TFEAc was estimated to be 9.1. This value is the lowest among those of O-donor solvents, such as water, alcohols, amides, and carbonates,[2] indicating that Li-ion solvation with TFEAc has lower stabilization energy than that using common organic solvents for energy storage devices, such as LIBs.

Figure 5.1 displays typical CV results for the graphite anode in the 1.0 mol dm^{-3} LiTFSA/TFEAc solution. Clear redox peaks were observed during the first cycle, that is, reductive peaks due to Li-ion insertion into the graphite electrode from 0.2 to 0 V (vs. Li/Li^+), and oxidative peaks due to Li-ion deinsertion from 0 to 0.4 V. A small reductive current was detected at approximately 0.5 V during the first cycle, which may be ascribed to the decomposition of the TFEAc component in the electrolyte. It should be noted that this 0.5 V-peak became pronounced during subsequent cycles. This is because no SEI formation occurred on the graphite electrode, resulting in no suppression of electrolyte decomposition. In popularly used carbonate-based electrolytes using EC, a small reductive peak is commonly observed due to EC decomposition in the first charging process; however it completely disappears due to the formation of stable EC-based passivation film (i.e., SEI), resulting in the suppression of further electrolyte decomposition and reversible Li-ion insertion/deinsertion (major current at around 0 V), even in subsequent cycles.[11, 22]

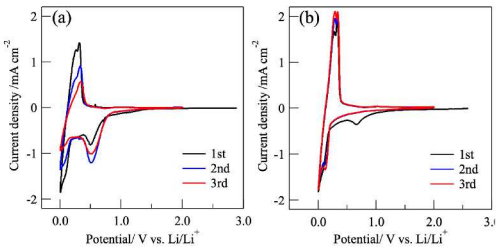

Figure 5.1 Cyclic voltammograms for the graphite electrode in 1.0 mol dm^{-3} (a) LiTFSA/TFEAc and (b) LiTFSA/TFEAc+EC solutions (x_{EC} = 0.1).

In the current TFEAc system, the major redox current observed in the first cycle gradually decreased with the cycle number, which is ascribable to the accumulated TFEAc decomposition products (no SEI formation) on the graphite electrode. To eliminate this problem, I investigated the addition of EC as an SEI additive into the TFEAc electrolyte (mole fraction of EC to TFEAc-EC mixture, x_{EC} = 0.1), and the results are presented in **Figure 5.1b**. It is clear that addition of EC allowed for an improved Li-ion insertion/deinsertion reaction. Focusing on the SEI formation, a small reductive current (0.7 V, first cycle) indicated the decomposition of the EC component, leading to EC-based SEI, as is well established, followed by a complete disappearance of the current during subsequent cycles. Therefore, a significant and reversible insertion/deinsertion reaction (major currents at around 0 V) occurred in the LiTFSA/TFEAc+EC solution. In detail, the observed peaks in the range of 0–0.3 V split into several peaks, which is typical for the sequential formation of several-stage structures of Li–graphite intercalation compounds.[10-11, 23-24] The reactivity of Li-ion insertion/deinsertion in the x_{EC} = 0.1 solution remained unchanged when EC was further added up to x_{EC} = 0.5 (**Figure A5.2a**). When reduced the EC content to x_{EC} = 0.02 (i.e., 1 wt% EC solution; **Figure A5.2b**), the redox current was slightly decreased, and a further reductive decomposition was observed at approximately 1.0 V. Based on the CV results, I conducted the charge-discharge test for 1.0 mol dm^{-3} LiTFSA/TFEAc+EC solution with x_{EC} = 0.1 to obtain further insight into the electrochemical properties for LIBs.

Figure 5.2 presents the discharge rate performance of the graphite/Li metal half-cell using 1.0 mol dm^{-3} LiTFSA/TFEAc with and without the EC additive (x_{EC} = 0.1). The observed charge/discharge curves with various C-rates are presented in **Figure A5.3**. At 0.1C (lowest C-rate examined in this study), the

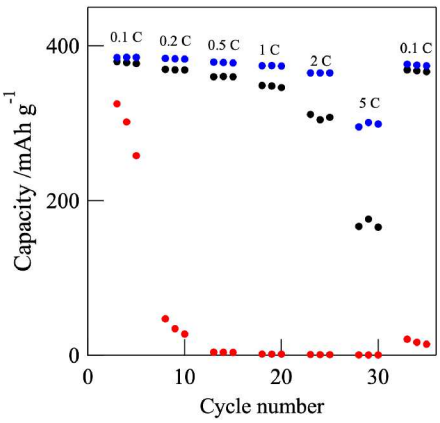

Figure 5.2 Discharge capacity of the graphite electrode in 1.0 mol dm^{-3} LiTFSA/TFEAc (red) and 1.0 mol dm^{-3} LiTFSA/TFEAc+EC (x_{EC} = 0.1, blue) at various C-rates, together with that in 1.0 mol dm^{-3} $LiPF_6$/EC+DMC (1:2 by volume, black). The 1 C rate corresponds to ~1.6 m cm^{-2}.

LiTFSA/TFEAc electrolyte (without EC) displayed a discharge capacity of 325 mAh g^{-1}, which is considerably lower than the theoretical capacity of graphite (372 mAh g^{-1}), and gradually decreased with the cycle number. This is due to no SEI formation on the graphite electrode and continuous electrolyte decomposition, which is consistent with the CV result in binary LiTFSA/TFEAc system (**Figure 5.1a**). Hence, with an increase in the C-rate, the capacity rapidly decreased to be almost not higher than 0.2 C. I found that the C-rate dependence of the capacity was markedly improved when adding EC. Surprisingly, the rate performance was superior to that of conventional carbonate-based electrolytes (1.0 mol dm^{-3} $LiPF_6$/EC+DMC, 1:2 by volume), even though the ionic conductivity is much lower in LiTFSA/TFEAc+EC (3.61 mS cm^{-1} at 298 K) than in $LiPF_6$/EC+DMC.[4, 25] The ionic conductivity and viscosity data are summarized in **Table A5.1**. At a C-rate lower than 0.5 C, all cells demonstrated a discharge capacity of ~372 mAh g^{-1} to exhibit almost no degradation even with an increase in the discharge density. With a further increase in the C-rate, the capacity slightly decreased; however, the values were greater than those for the carbonate-based electrolyte even at 2 C and 5 C. **Figure A5.4a** presents the cycle performance of the discharge capacity (up to 50 cycles) at the 0.1 C rate for the LiTFSA/TFEAc+EC electrolyte with x_{EC} = 0.1. The corresponding charge–discharge curves are presented in **Figure A5.4b**. No or less capacity degradation occurred up to 50 cycles, and the coulombic efficiency remained unchanged at approximately 99%, except for cycles 1 to 5 (~96%). In contrast, the cycle performance was very poor in LiTFSA/TFEAc without EC; specifically, significant capacity degradation was observed in the early cycle stage (**Figures A5.4c and d**). I thus concluded that adding EC (i.e., SEI additive) into a TFEAc-based electrolyte is key to achieving practical LIBs with high-rate performance.

5.3.2 *Li-ion solvation structure*

To characterize the solvation behavior of Li ions in a weaker coordination solvent, TFEAc, I performed Raman spectroscopy measurements and their quantitative spectral analysis. **Figure 5.3a** presents the Raman spectra in the range of 880–980 cm^{-1} for LiTFSA/TFEAc solutions with varying c_{Li} (0–1.0 mol dm^{-3}). A major peak at ~917 cm^{-1} gradually decreased in intensity as c_{Li} increased; conversely, a new peak appeared at ~937 cm^{-1} and intensified as c_{Li} increased. According to DFT calculations (theoretical Raman bands, **Figure A5.5**), the former 917 cm^{-1} peak was assigned to the TFEAc molecules in the bulk (called free TFEAc); specifically, the C–C–H bending vibration coupled with the C–O–C asymmetric stretching vibration, whereas the latter 937 cm^{-1} peak was assigned to the TFEAc bound to the Li ion (called bound TFEAc). I performed a least-squares curve-fitting analysis to deconvolute the observed spectra into individual bands. A typical fitting result for the c_{Li} = 0.75 mol dm^{-3} solution is presented in **Figure 5.3b**. The Raman spectrum could be successfully deconvoluted into five components in this frequency range, which was applied to the spectra for every c_{Li}. Consequently, I extracted the individual band for free TFEAc (centered at 916.9 cm^{-1}, blue line in the figure) and that for bound TFEAc (centered at 937.0 cm^{-1}, red line). According to the current DFT calculations (**Figure A5.5**), the 970 cm^{-1}-band (gray line) was assigned to the TFEAc (CH_2 asymmetric vending mode); on the other hand, the 880 cm^{-1}- and 898 cm^{-1}-band (gray) are unknown at the present stage. I confirmed no contribution of these three bands on the analysis of solvation number, which is described in detail in **Appendix** (**Figure A5.6**).

To estimate the average solvation number (n_{TFEAc}) of TFEAc molecules around a Li ion, I calculated the integrated intensities of the free TFEAc band and plotted them as a function of c_{Li} (**Figure 5.3c**) according to Eq. (7) described in the Experimental section. The resulting I_f/c_T versus c_{Li}/c_T plots fell on a straight line with slope $-nJ_f$ and intercept J_f to yield n_{TFEAc} = 1.9 ± 0.1. This indicated that Li ions were solvated with approximately two TFEAc molecules. It should be noted that in conventional aprotic solvents, a Li ion is four-coordinated with solvent molecules to form a tetrahedral $[Li(solvent)_4]^+$ complex;[26-27] however, this was not the case in the current TFEAc system. I thus expected that the Li ions would be coordinated with both TFEAc and $TFSA^-$ components, resulting in the formation of an ion-

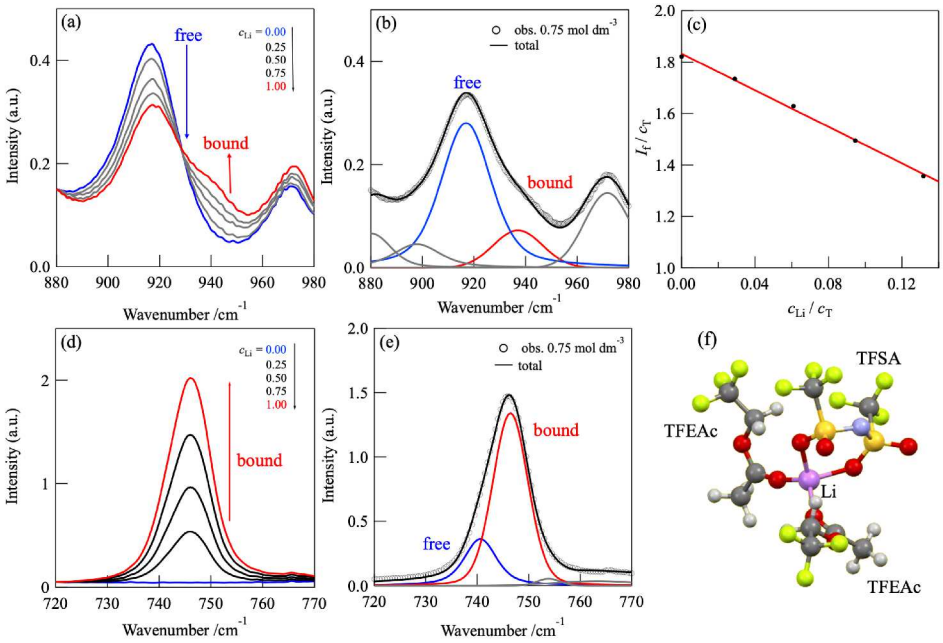

Figure 5.3 (a) Raman spectra in the range of 880–980 cm^{-1} observed for LiTFSA/TFEAc with various c_{Li}, (b) a typical curve fitting result for the c_{Li} = 0.75 mol dm^{-3} solution, (c) I_f/c_T vs. c_{Li}/c_T plots using the free TFEAc-band, (d) Raman spectra in the range of 720–770 cm^{-1} for the same solutions, (e) a typical curve fitting result (c_{Li} = 0.75 mol dm^{-3}), (f) optimized geometry of [Li(TFEAc)$_2$(TFSA)] complex by DFT calculations.

pair complex, such as [Li(TFEAc)$_2$(TFSA)$_m$]. To verify the TFSA coordination, further analysis of the observed Raman spectra was performed.

Figure 5.3d presents Raman spectra in the range of 720–770 cm^{-1} for LiTFSA/TFEAc solutions with varying c_{Li}. A peak appeared at ~746 cm^{-1}, which was assigned to the CF_3 bending vibration coupled with the S–N–S stretching vibration of the TFSA,[28-29] and increased in intensity as c_{Li} increased. Using fitting analysis in a similar manner as described above, peak deconvolution of the observed spectra was performed to extract sole peaks corresponding to free TFSA and bound TFSA (see **Figure 5.3e**), resulting in the 740.6 cm^{-1} band and 746.5 cm^{-1} band, respectively. Using the integrated intensities of these bands, I estimated the concentration ratio of free and bound TFSA species in the solutions; the procedure is described in detail in the Supporting Information. As a result, c_b/c_T (the concentration ratio of the bound TFSA to the total TFSA) was determined to be approximately 0.8 for all c_{Li} solutions examined (**Table A5.2**). These results indicate that 80% of the total TFSA anions coordinated with Li ions to form $Li^+\cdots TFSA^-$ (1:1) ion pairs even in dilute c_{Li} solutions (< 1.0 mol dm^{-3}). Thus, I concluded that in the LiTFSA/TFEAc solutions, Li ions mainly existed as [Li(TFEAc)$_2$(TFSA)] complexes as the major species (the optimized geometry obtained from DFT calculations is presented in **Figure 5.3f**), which coexisted with ion-pair-free species as the minor species (20%). **Figure 5.3f** demonstrates that the bound TFSA acted as a bidentate ligand to coordinate with an Li ion via two O atoms within a molecule. This feature is consistent with that of TFSA-based ionic liquids and organic solvents with lower solvation ability.[4, 28, 30]

Figure 5.4a presents the Raman spectra observed for LiTFSA/TFEAc+EC solutions (x_{EC} = 0.1) with different c_{Li} (0–1.0 mol dm^{-3}). In the range of 910–950 cm^{-1}, similar c_{Li} dependence to that of the binary LiTFSA/TFEAc system was observed; that is, the free TFEAc peak (at ~ 917 cm^{-1}) decreased in intensity with increasing c_{Li}, and the bound TFEAc peak (at ~ 937 cm^{-1}) intensified with increasing c_{Li}. Furthermore, I observed a significant c_{Li} dependence of the EC-derived peak in the range of 880–910 cm^{-1}. The peak at ~ 892 cm^{-1} corresponding to the C=O bending vibration of EC in the bulk (called free EC) considerably decreased in intensity as c_{Li} increased to yield a new intense peak at ~ 905 cm^{-1}.[31] This new band was assigned to the EC bound to the Li ion (called bound EC) according to the DFT calculations (see **Figure A5.5**). The peak variations observed for the TFEAc and EC components indicated that Li ions were solvated with both TFEAc and EC molecules to form cosolvated Li-ion complexes.

To estimate the individual solvation numbers of TFEAc (n_{TFEAc}) and EC (n_{EC}) around a Li ion, peak deconvolution was performed for the observed Raman spectra, and a typical result (c_{Li} = 0.75 mol dm^{-3}) is presented in **Figure 5.4b**. The Raman spectrum in the

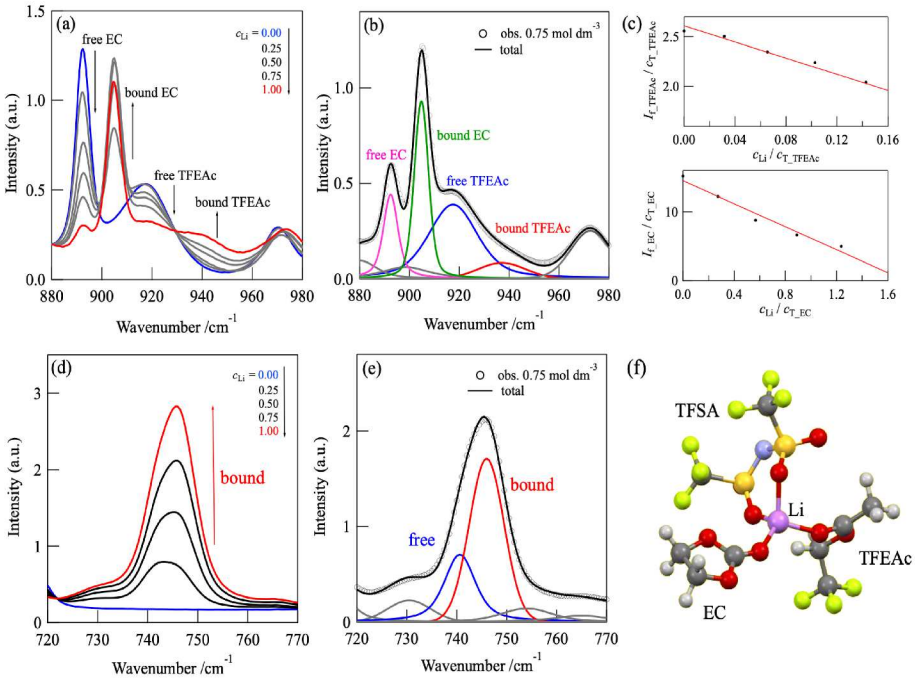

Figure 5.4 (a) Raman spectra in the range of 880–980 cm^{-1} observed for the 1.0 mol dm^{-3} LiTFSA/TFEAc+EC mixtures (x_{EC} = 0.1) with various c_{Li}, (b) a typical curve fitting result for the c_{Li} = 0.75 mol dm^{-3} solution, (c) I_f/c_T vs. c_{Li}/c_T plots using the free TFEAc band (top) and free EC band (bottom), (d) Raman spectra in the range of 720–770 cm^{-1} for the same solutions, (e) a typical curve fitting result (c_{Li} = 0.75 mol dm^{-3}), (f) optimized geometry of the [Li(TFEAc)(EC)(TFSA)] complex by DFT calculations.

range of 880–980 cm^{-1} was well reproduced using seven contributions, including mainly 892.2 cm^{-1} (free EC), 904.7 cm^{-1} (bound EC), 917 cm^{-1} (free TFEAc), and 937 cm^{-1} (bound TFEAc). The I_f/c_T versus c_{Li}/c_T plot (**Figure 5.4c**) displays a linear relation for both TFEAc and EC bands; thus, I successfully determined the individual solvation numbers to be n_{TFEAc} = 1.4 ± 0.2 and n_{EC} = 0.6 ± 0.1. With regard to the Raman band for TFSA anions, I also performed peak deconvolution, and c_b/c_T was determined in a similar way to that described above (see **Table A5.3**). The resulting c_b/c_T value was approximately 0.7, implying that the Li ions existed as 70% ion-pair and 30% ion-pair-free species. Based on these results, I concluded that adding EC into LiTFSA/TFEAc solution triggered a structural change in the Li-ion complexes. That is, bound TFEAc was replaced with EC to form [Li(TFEAc)(EC)(TFSA)] as an average structure in LiTFSA/TFEAc+EC solution (x_{EC} = 0.1). In addition, [Li(TFEAc)(EC)(TFSA)] coexisted with [Li(TFEAc)$_2$(TFSA)] in the solution, resulting in an average solvation number of 1.4 for TFEAc and 0.6 for EC. This result may be due to a larger D_N value of EC (16.4) than that of TFEAc (9.1); thus, EC molecules could successfully solvate Li ions even with lower EC content (x_{EC} = 0.1).

Based on the electrochemical and structural results, I discuss the relationship between the electrode reaction and solvation of Li ions in the TFEAc-based solution. The graphite electrode reaction was significantly improved when EC was added into the LiTFSA/TFEAc solution. In the structural aspect, Li ion structures were largely changed by the added EC to yield EC-solvated Li ions (i.e., [Li(TFEAc)(EC)(TFSA)]) as the major species and ion-pair-free Li ions as the minor species. During the first charging process, the EC-solvated Li-ion complexes may have been located at the electrode/electrolyte interface; thereafter, the solvated EC molecules were reductively decomposed to form an EC-derived passivation film (i.e., SEI) on the graphite electrode. Indeed, the LUMO energy of the solvated EC molecule (i.e., Li$^+$-EC complex) is appreciably stable than that of the free EC according to DFT calculations (**Figure A5.8**: optimized geometries of EC molecule and Li$^+$-EC complex), implying preferential reductive decomposition of the solvated EC, rather than free EC, on graphite electrode.

In addition, the TFEAc molecule had much weaker electron-pair donating ability, leading to weaker Li$^+$···TFEAc interactions. This may have induced favorable desolvation of the solvated Li-ion complexes at the electrode/electrolyte interface during the charge transfer process, which has been established as a key process in the graphite electrode reaction,[17-18] leading to high-rate charging/discharging in the TFEAc+EC

system. In contrast, without EC, Li ions mainly formed the [Li(TFEAc)$_2$(TFSA)] complex. The Li-ion complex located at the electrode interface was also decomposed during the charging process, and significant reductive current was observed at 0.5 V in the CV profile for the LiTFSA/TFEAc solution (**Figure 5.1a**). However, no SEI formation occurred due to the absence of EC, followed by only TFEAc-decomposed products accumulating on the graphite electrode. This resulted in the significant degradation of the electrode reaction with repeating charge/discharge cycles.

5.4 Conclusions

In this study, I characterized a new fluorinated solvent, TFEAc, as an electrolyte solvent for LIBs by electrochemical and structural investigations. The binding energy for the Li^+-TFEAc (1:1) complex using DFT calculations indicated that the TFEAc molecule had much lower solvation power among organic solvents corresponding to the Gutmann donor number D_N = 9.1. In the LiTFSA/TFEAc electrolyte solution, a clear Li-ion insertion reaction was observed for the graphite negative electrode during the first charging process; however, the reaction decreased quickly in subsequent cycles. I found that adding a small amount of EC (x_{EC} = 0.1) into the TFEAc electrolyte greatly improved the graphite electrode reaction to exhibit reversible charge/discharge behavior with high-rate performance that was superior to that of commercial carbonate electrolytes. Structural investigations using Raman spectra and their quantitative analysis revealed that in binary LiTFSA/TFEAc, Li ions formed a contact ion pair, [Li(TFEAc)$_2$(TFSA)], as the major species even in dilute solution (< 1.0 mol dm^{-3}). When EC was added, the TFEAc molecules bound to the Li ions were partially replaced with EC molecules, resulting in EC-coordinated ion-pair complexes. The bound EC molecules played a key role in the graphite electrode reaction, namely, preferential reductive decomposition of the bound EC near the electrode interface during the first charging, followed by the formation of EC-derived SEI passivation film on the graphite electrode.

5.5 References

(1) Gutmann, V. *The Donor-Acceptor Approach to Molecular Interactions*, Plenum: New York, 1978.

(2) Marcus, Y. *The Properties of Solvents*, John Wiley & Sons Ltd.: New York, 1998.

(3) Fujii, K.; Wakamatsu, H.; Todorov, Y.; Yoshimoto, N.; Morita, M. Structural and Electrochemical Properties of Li Ion Solvation Complexes in the Salt-Concentrated Electrolytes Using an Aprotic Donor Solvent, *N*,*N*-Dimethylformamide. *J. Phys. Chem. C* **2016,** *120*, 17196-17204.

(4) Sogawa, M.; Todorov, Y. M.; Hirayama, D.; Mimura, H.; Yoshimoto, N.; Morita, M.; Fujii, K. Role of Solvent Bulkiness on Lithium-Ion Solvation in Fluorinated Alkyl Phosphate-Based Electrolytes: Structural Study for Designing Nonflammable Lithium-Ion Batteries. *J. Phys. Chem. C* **2017,** *121*, 19112-19119.

(5) Sogawa, M.; Sawayama, S.; Han, J.; Satou, C.; Ohara, K.; Matsugami, M.; Mimura, H.; Morita, M.; Fujii, K. Role of Solvent Size in Ordered Ionic Structure Formation in Concentrated Electrolytes for Lithium-Ion Batteries. *J. Phys. Chem. C* **2019,** *123*, 8699-8708.

(6) Sawayama, S.; Todorov, Y. M.; Mimura, H.; Morita, M.; Fujii, K. Fluorinated alkyl-phosphate-based electrolytes with controlled lithium-ion coordination structure. *Phys. Chem. Chem. Phys.* **2019,** *21*, 11435-11443.

(7) Umebayashi, Y.; Mroz, B.; Asada, M.; Fujii, K.; Matsumoto, K.; Mune, Y.; Probst, M.; Ishiguro, S. Conformation of solvent *N*,*N*-dimethylpropionamide in the coordination sphere of the zinc(II) ion studied by Raman spectroscopy and DFT calculations. *J. Phys. Chem. A* **2005,** *109*, 4862-4868.

(8) Ishiguro, S.-i.; Umebayashi, Y.; Fujii, K.; Kanzaki, R. Solvent conformation and ion solvation: From molecular to ionic liquids. *Pure Appl. Chem.* **2006,** *78*, 1595-1609.

(9) Etacheri, V.; Marom, R.; Elazari, R.; Salitra, G.; Aurbach, D. Challenges in the development of advanced Li-ion batteries: a review. *Energy Environ. Sci.* **2011,** *4*, 3243.

(10) Aurbach, D. Review of selected electrode–solution interactions which determine the performance of Li and Li ion batteries. *J. Power Sources* **2000,** *89*, 206-218.

(11) Aurbach, D.; Zaban, A.; Ein-Eli, Y.; Weissman, I. Recent studies on the correlation between surface chemistry, morphology, three-dimensional structures and performance of Li and Li-C intercalation anodes in several important electrolyte systems. *J. Power Sources* **1997,** *68*, 91-98.

(12) Peled, E. The electrochemical behavior of alkali and alkaline earth metals in nonaqueous battery systems—the solid electrolyte interphase model. *J. Electrochem. Soc.* **1979,** *126*, 2047-2051.

(13) Fong, R.; Sacken, U. v.; Dahn, J. R. Studies of Lithium Intercalation into Carbons Using Nonaqueous Electrochemical Cells. *J. Electrochem. Soc.* **1990,** *137*, 2009-2013.

(14) Ushirogata, K.; Sodeyama, K.; Okuno, Y.; Tateyama, Y. Additive effect on reductive decomposition and binding of carbonate-based solvent toward solid electrolyte interphase formation in lithium-ion battery. *J. Am. Chem. Soc.* **2013,** *135*, 11967-74.

(15) Sogawa, M.; Kawanoue, H.; Todorov, Y. M.; Hirayama, D.; Mimura, H.; Yoshimoto, N.; Morita, M.; Fujii, K. Solvation-controlled lithium-ion complexes in a nonflammable solvent containing ethylene carbonate: structural and electrochemical aspects. *Phys. Chem. Chem. Phys.* **2018,** *20*, 6480-6486.
(16) Sato, T.; Maruo, T.; Marukane, S.; Takagi, K. Ionic liquids containing carbonate solvent as electrolytes for lithium ion cells. *J. Power Sources* **2004,** *138*, 253-261.
(17) Abe, T.; Fukuda, H.; Iriyama, Y.; Ogumi, Z. Solvated Li-Ion Transfer at Interface Between Graphite and Electrolyte. *J. Electrochem. Soc.* **2004,** *151*, A1120.
(18) Abe, T.; Sagane, F.; Ohtsuka, M.; Iriyama, Y.; Ogumi, Z. Lithium-Ion Transfer at the Interface Between Lithium-Ion Conductive Ceramic Electrolyte and Liquid Electrolyte-A Key to Enhancing the Rate Capability of Lithium-Ion Batteries. *J. Electrochem. Soc.* **2005,** *152*.
(19) Okoshi, M.; Yamada, Y.; Yamada, A.; Nakai, H. Theoretical Analysis on De-Solvation of Lithium, Sodium, and Magnesium Cations to Organic Electrolyte Solvents. *J. Electrochem. Soc.* **2013,** *160*, A2160-A2165.
(20) Doi, T.; Fujii, R.; Aoki, Y.; Nagashima, T.; Takehara, K.; Inaba, M. Physicochemical Features of Fluorinated Ethyl Acetate-Based Highly Concentrated Electrolyte Solutions and Their Effects on Electrochemical Properties of $LiNi_{0.8}Co_{0.1}Mn_{0.1}O_2$ Positive Electrodes. *J. Phys. Chem. C* **2021,** *125*, 12578-12584.
(21) Asada, M.; Fujimori, T.; Fujii, K.; Kanzaki, R.; Umebayashi, Y.; Ishiguro, S. Solvation structure of magnesium, zinc, and alkaline earth metal ions in *N,N*-dimethylformamide, *N,N*-dimethylacetamide, and their mixtures studied by means of Raman spectroscopy and DFT calculations –Ionic size and electronic effects on steric congestion–. *J. Raman Spectrosc.* **2007,** *38*, 417-426.
(22) Hazama, T.; Fujii, K.; Sakai, T.; Aoki, M.; Mimura, H.; Eguchi, H.; Todorov, Y.; Yoshimoto, N.; Morita, M. High-performance gel electrolytes with tetra-armed polymer network for Li ion batteries. *J. Power Sources* **2015,** *286*, 470-474.
(23) Dahn, J. R. Phase diagram of Li_xC_6. *Phys. Rev. B* **1991,** *44*, 9170-9177.
(24) Ohzuku, T.; Iwakoshi, Y.; Sawai, K. Formation of Lithium-Graphite Intercalation Compounds in Nonaqueous Electrolytes and Their Application as a Negative Electrode for a Lithium Ion (Shuttlecock) Cell. *J. Electrochem. Soc.* **1993,** *140*, 2490-2498.
(25) Dahbi, M.; Ghamouss, F.; Tran-Van, F.; Lemordant, D.; Anouti, M. Comparative study of EC/DMC LiTFSI and $LiPF_6$ electrolytes for electrochemical storage. *J. Power Sources* **2011,** *196*, 9743-9750.
(26) Ohtaki, H.; Radnai, T. Structure and dynamics of hydrated ions. *Chem. Rev.* **1993,** *93*, 1157-1204.
(27) Burgess, J. *Ions in Solution, 2nd ed.*, Horwood Publishing: 1999.
(28) Umebayashi, Y.; Mitsugi, T.; Fukuda, S.; Fujimori, T.; Fujii, K.; Kanzaki, R.; Takeuchi, M.; Ishiguro, S. Lithium-ion Solvation in Room Temperature Ionic Liquids Involving Bis-(trifluorosulfonyl) Imide Anion Studied by Raman Spectroscopy and DFT Calculations. *J. Phys. Chem. B* **2007,** *111*, 13028-13032.
(29) Kamiyama, Y.; Shibata, M.; Kanzaki, R.; Fujii, K. Lithium-ion coordination-induced conformational change of PEG chains in ionic-liquid-based electrolytes. *Phys. Chem. Chem. Phys.* **2020,** *22*, 5561-5567.
(30) Fujii, K.; Nonaka, T.; Akimoto, Y.; Umebayashi, Y.; Ishiguro, S.-i. Solvation Structures of Some Transition Metal(II) Ions in a Room-Temperature Ionic Liquid, 1-Ethyl-3-methylimidazolium Bis(trifluoromethanesulfonyl)amide. *Analytical Sciences* **2008,** *24*, 1377-1380.
(31) Morita, M.; Asai, Y.; Yoshimoto, N.; Ishikawa, M. A Raman spectroscopic study of organic electrolyte solutions based on binary solvent systems of ethylene carbonate with low viscosity solvents which dissolve different lithium salts. *J. Chem. Soc., Faraday trans* **1998,** *94*, 3451-3456.
(32) Sai, R.; Ueno, K.; Fujii, K.; Nakano, Y.; Shigaki, N.; Tsutsumi, H. Role of polar side chains in Li^+ coordination and transport properties of polyoxetane-based polymer electrolytes. *Phys. Chem. Chem. Phys.* **2017,** *19*, 5185-5194.

5.6 Appendix

Estimation of c_f/c_b ratio for TFSA anion.

The integrated intensities of the free and bound TFSA anions are given as $I_f = J_f c_f$ and $I_b = J_b c_b$, respectively, where J_f and J_b are the Raman scattering coefficients and c_f and c_b are the concentrations of the free and bound TFSA anions in the solution. The ratio of free TFSA to bound TFSA (c_f/c_b) is thus represented by the following equation: $c_f/c_b = (I_b/I_f)(J_f/J_b)$. Here, note that the J_f/J_b value is approximately constant (~0.9) in various electrolytes containing LiTFSA (i.e., ionic liquid, organic solvent, and polymer electrolytes) when TFSA anions act as a bidentate-type ligand in the Li-ion complexes.[4, 28, 32] Using (1) $J_f/J_b = 0.9$ and (2) I_b/I_f value obtained from the observed Raman data, we calculated the c_f/c_b value to estimate the concentration ratio of bound TFSA to total TFSA, c_b/c_T (listed in **Table A5.2 and S5.3**).

Table A5.1 Ionic conductivities (σ) and viscosity (η) of 1.0 mol dm^{-3} LiTFSA/TFEAc and LiTFSA/TFEAc+EC solutions ($x_{EC} = 0.1$) at 298 K.

Sample	σ / mS cm^{-1}	η / mPa·s
LiTFSA/TFEAc	2.47	2.09
LiTFSA/TFEAc+EC	3.61	2.42

Table A5.2 The integrated intensity (I) ratio of bound TFSA to free TFSA(I_b/I_f), and the concentration ratio of bound TFSA to total TFSA (c_b/c_T) for LiTFSA/TFEAc solutions with various c_{Li}.

c_{Li} / mol dm^{-3}	I_b/I_f	c_b/c_T
0	-	-
0.25	5.04	0.82
0.50	4.77	0.81
0.75	4.64	0.81
1.0	4.89	0.81
1.4	5.79	0.84
		Avg. 0.82

Table A5.3 The integrated intensity (I) ratio of bound TFSA to free TFSA(I_b/I_f), and the concentration ratio of bound TFSA to total TFSA (c_b/c_T) for LiTFSA/TFEAc+EC solutions ($x_{EC} = 0.1$) with various c_{Li}.

c_{Li} / mol dm^{-3}	I_b/I_f	c_b/c_T
0	-	-
0.25	1.51	0.58
0.50	2.51	0.69
0.75	3.22	0.74
1.0	3.48	0.76
1.5	3.39	0.64
		Avg. 0.68

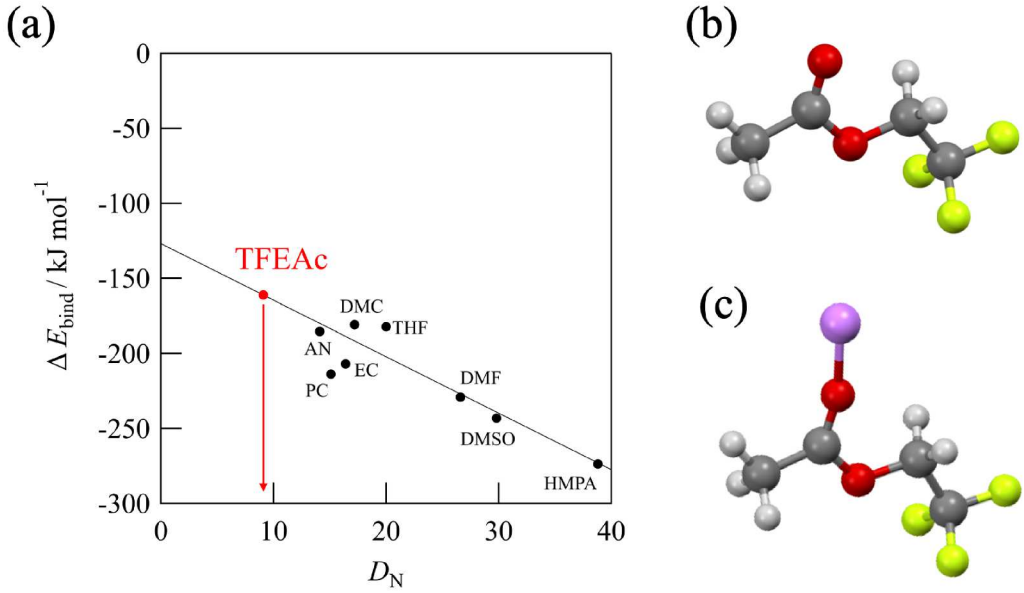

Figure A5.1 (a) Binding energy ΔE_{bind} values calculated for the Li^+-solvent (1:1) complexes plotted against the corresponding Gutmann's donor number D_N values for acetonitrile (AN), ethylene carbonate (EC), dimethyl carbonate (DMC), propylene carbonate (PC), tetrahydro- furan (THF), *N,N*-dimethylformamide (DMF), dimethyl sulfoxide (DMSO), and hexamethylphosphoric triamide (HMPA).[2]

The ΔE_{bind} value for the Li^+-TFEAc (1:1) complex obtained from the following equation: $\Delta E_{bind} = E_{SCF}(complex) - E_{SCF}(Li^+) - E_{SCF}(TFEAc)$, was 161.1 kJ mol^{-1}. The value corresponds to D_N = 9.1 according to the linear relation (i.e., $\Delta E_{bind} = -3.36 \cdot D_N - 139.6$) based on ΔE_{bind} vs D_N plots.[4] The E_{SCF}(TFEAc) and E_{SCF}(complex) values were evaluated from their optimized geometries of (b) sole TFEAc molecule and (c) Li^+-TFEAc (1:1) complex.

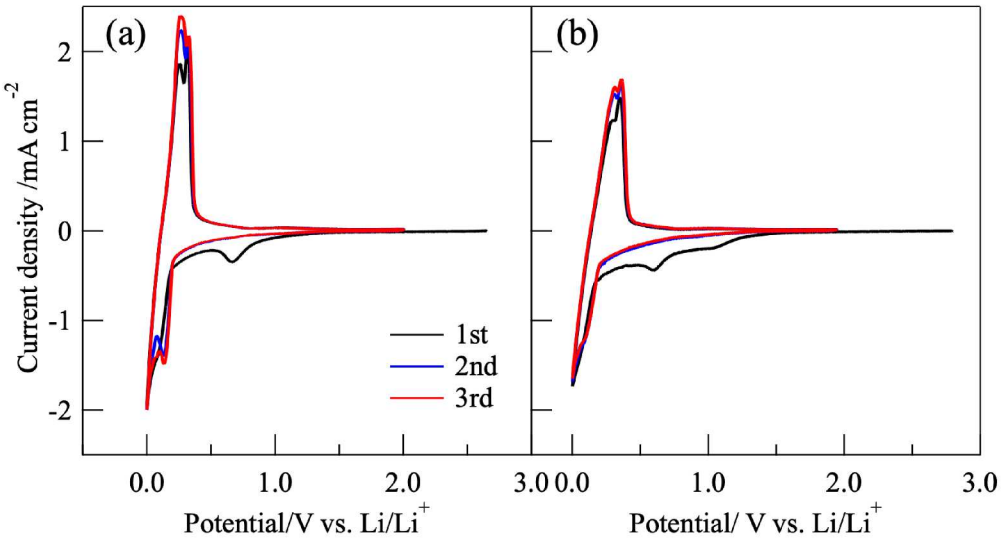

Figure A5.2 Cyclic voltammograms for the graphite electrode in 1.0 mol dm^{-3} LiTFSA/TFEAc+EC solutions (a) x_{EC} = 0.5 and (b) 0.02.

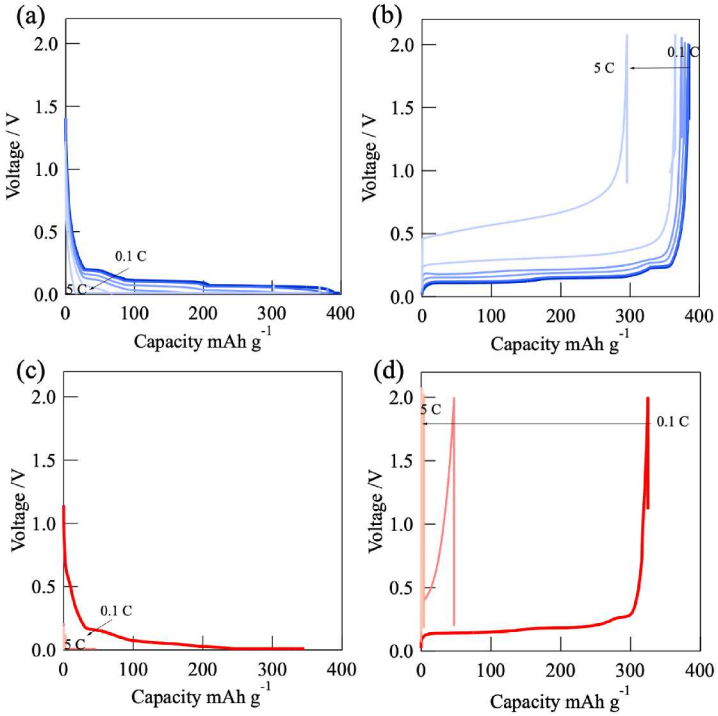

Figure A5.3 Charge and discharge curves for the graphite electrode in the (a, b) 1.0 mol dm^{-3} LiTFSA/TFEAc+EC solution (x_{EC} = 0.1), and (c, d) 1.0 mol dm^{-3} LiTFSA/TFEAc solution (without EC) measured at various C-rates.

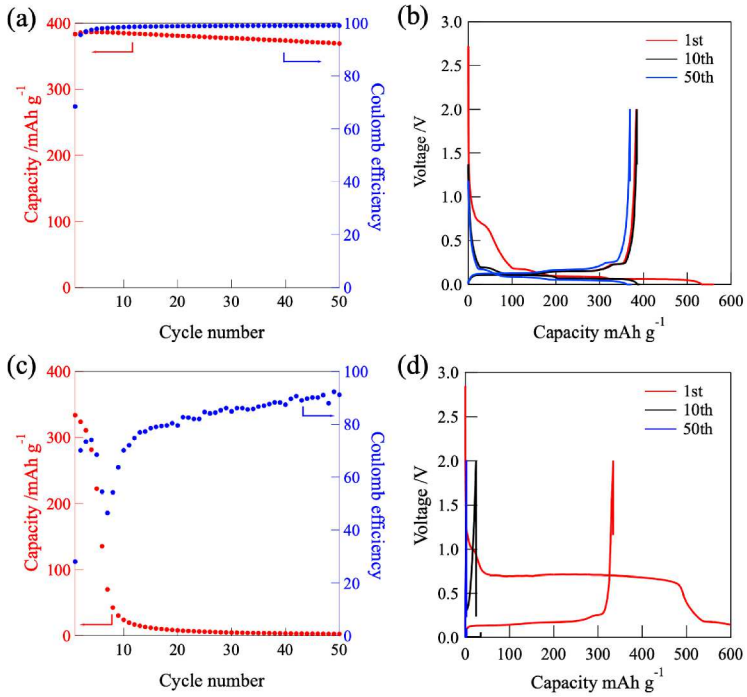

Figure A5.4 Cycling performance (red, left axis) and coulomb efficiency (blue, right axis) of the (a) 1.0 mol dm^{-3} LiTFSA/TFEAc+EC solution (x_{EC} = 0.1) and (c) 1.0 mol dm^{-3} LiTFSA/TFEAc solution. Charge–discharge curves for the graphite electrode in the (b) 1.0 mol dm^{-3} LiTFSA/TFEAc+EC solution (x_{EC} = 0.1) and (d) 1.0 mol dm^{-3} LiTFSA/TFEAc solution (without EC) at a C/10 rate.

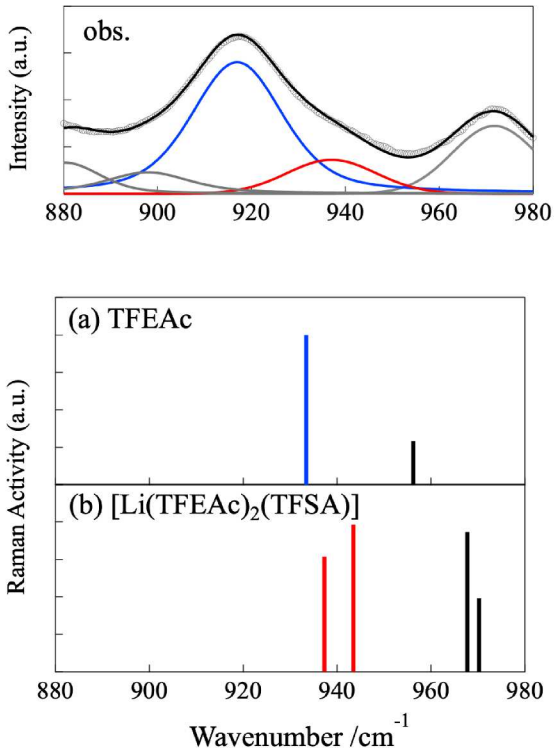

Figure A5.5 Theoretical Raman bands obtained from the optimized geometries of (a) isolated TFEAc and (b) [$Li(TFEAc)_2(TFSA)$] complex by DFT calculations, together with the experimental Raman bands for 1.0 mol dm^{-3} LiTFSA/TFEAc solution.

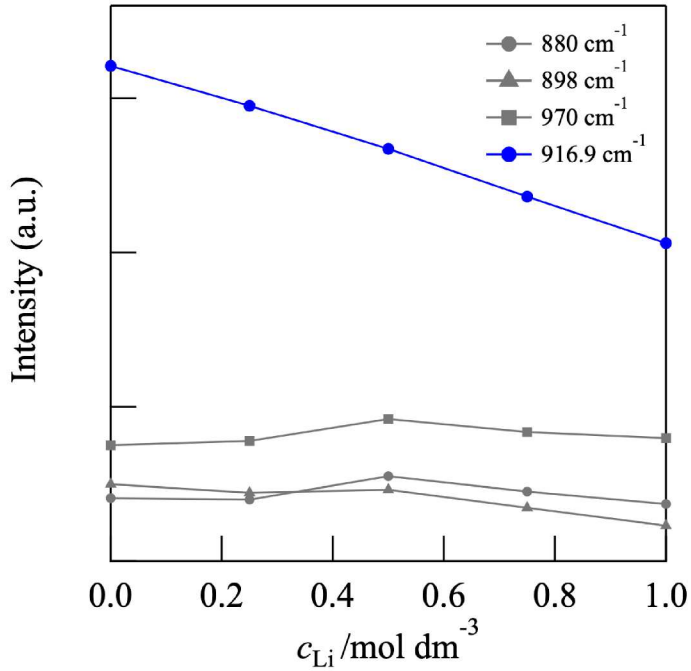

Figure A5.6 The c_{Li} dependence of the integrated Raman intensites of 880, 898 and 970 cm^{-1}-bands (gray circle, triangle, and square, respectively) for the 1.0 mol dm^{-3} LiTFSA/TFEAc solutions, together with the 916.9 cm^{-1}-band (blue circle) that is used in the determination of solvation number.

In **Figure 5.3b**, I showed the three deconvoluted curves colored with gray at approximately 880, 898 and 970 cm^{-1}. The 970 cm^{-1}-band can be assigned to the TFEAc component [$\delta_{as}(CH_2)$] according to theoretical Raman band by the current DFT calculations as shown in **Figure A5.5**. The other two band at 880 and 898 cm^{-1} are unknown at the present stage. There were no theoretical Raman band in this frequency range in **Figure A5.5**. However, I have confirmed no contribution of these two bands to the determination of solvation number. As can be seen in this Figure, it is clear that there is no c_{Li} dependence in the intensity to be a flat even with varying c_{Li}. This means that the three bands (gray lines) are no contribution to the solvation number analysis.

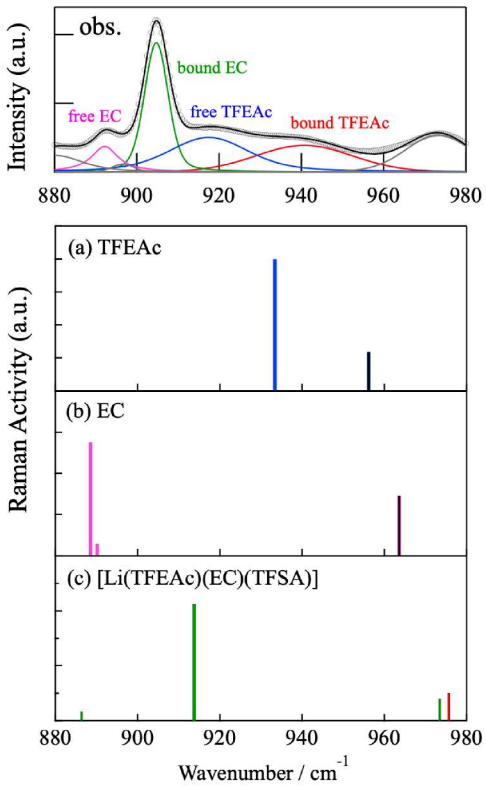

Figure A5.7 Theoretical Raman bands obtained from the optimized geometries of (a) isolated TFEAc, (b) isolated EC, and (c) [Li(TFEAc)(EC)(TFSA)] complex by DFT calculations, together with the experimental Raman bands for 1.0 mol dm^{-3} LiTFSA/TFEAc+EC solution (x_{EC} = 0.1).

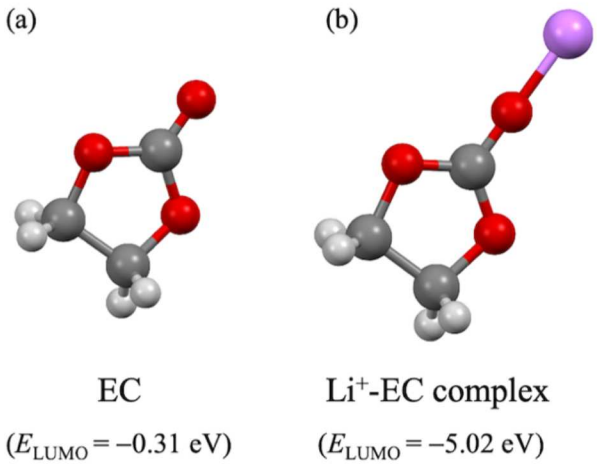

Figure A5.8 The optimized geometries of (a) isolated EC and (b) Li^+-EC complex and their LUMO energies obtained from DFT calculations.

Chapter 6

Effect of a Weak Coordination Solvent on a Kinetically Favorable Electrode Reaction in Concentrated Lithium-Ion Battery Electrolytes

6.1 Introduction

In Chapter 5, I proposed a significantly high-rate performance LIB electrolyte using a fluorinated acetate solvent (2,2,2-trifluoroethyl acetate, termed TFEAc). According to the DFT calculations in our previous work, TFEAc has much weaker coordination power to metal ions, corresponding to D_N = 9.1.[1] The TFEAc-based electrolyte solution containing 1.0 mol dm^{-3} of LiTFSA salt [TFSA: bis(trifluoromethanesulfonyl)amide] exhibited excellent charge–discharge behaviors and improved rate performance compared to conventional carbonate-based electrolytes.[1] Doi et al. used TFEAc as a solvent for a highly concentrated electrolyte for positive electrode, such as $LiNi_{0.8}Co_{0.1}Mn_{0.1}O_2$, to successfully conduct a charge–discharge reaction with a high discharge capacity of approximately 200 mAh g^{-1}.[2] However, unlike dilute electrolytes, the electrode reaction mechanism in highly concentrated electrolytes based on weak coordination solvent, fluorinated acetate, has not been reported. Even in conventional negative electrode materials for LIBs, information on basic charge–discharge characteristics is unavailable.

The electrode reaction mechanism has been established in a dilute electrolyte system (e.g., 1.0 mol dm^{-3} Li salt in solvent mixtures of carbonates). Kinetic studies on an intercalation-type electrode, such as a graphite negative electrode, have been actively reported to provide molecular insights into the Li-ion intercalation process. Abe et al. reported the activation energy (E_a) on the Li^+-insertion reaction for the graphite electrode in dilute carbonate-based electrolyte to be 53 – 59 kJ mol^{-1}, which was mainly attributed to the desolvation process for solvated Li ions, usually 4-coordinated $[Li(solvent)_4]^+$ complex, near the electrode/electrolyte interface.[3-5] Further systematic investigation on electrode reaction kinetics reveals the following results:[5] (1) The E_a value strongly depends on the solvation power of the solvent molecule (Gutmann's donor number, D_N); that is, stronger Li-ion solvation leads to larger E_a value, resulting in kinetically unfavorable Li-ion intercalation. (2) In such an intercalation-type reaction, the charge transfer process is almost independent of negative electrode materials and passivation SEI films; that is, only Li-ion desolvation is predominant in reflecting the E_a value. Therefore, controlling ion-solvent interactions to achieve "much weaker Li-ion coordination" may be a key to developing practical LIBs with high-rate performance.

In this study, I extend my study on a dilute TFEAc-based electrolyte to a "highly concentrated electrolyte," focusing on the role of a weaker coordination solvent on electrode reaction (Li-ion intercalation) kinetics in concentrated conditions. First, the electrochemical properties and charge–discharge performance of the graphite anode are investigated in concentrated LiFSA/TFEAc electrolytes. I determineed the E_a value during the charge transfer process in a Li-ion intercalation reaction to propose a kinetically favorable reaction in this TFEAc-based system. The electrode reaction mechanism at the molecular level based on specific Li-ion structures and its easier decoordination characteristics are also discussed.

6.2 Experimental

6.2.1 *Materials*

The corresponding molarities (Li salt concentration, c_{Li}) of Sample were then calculated using the solution density (g cm^{-3}) to prepare LiFSA/TFEAc solutions at c_{Li} = 1.0, 1.9, 2.4, and 3.2 mol dm^{-3}, corresponding to the molar ratios of Li salt/solvent, 1/7.6, 1/4, 1/3, and 1/2, respectively. Karl Fischer titration was used to determine that the sample solution's water content was less than 50 ppm. I demonstrated "nonflammability" of the highest c_{Li} = 3.2 mol dm^{-3} solution using a flam test (**Figure A6.1** in **Appendix**), proving that it can serve as a safer electrolyte for LIBs. The composition (i.e., number of LiFSA salt and TFEAc molecule) in MD simulation box and the box length at equilibrium condition are listed in **Table A6.1**. Flame tests were conducted by using a glass filter soaked with each electrolyte close to gas burner flame in a draft chamber.

6.3 Results and discussion

6.3.1 *Electrochemical properties*

Figure 6.1 shows the ionic conductivity (σ) and viscosity (η) for the concentrated LiFSA/TFEAc electrolytes at various Li salt concentrations (c_{Li} = 1.9 ~ 3.2 mol dm^{-3}) at 298 K. The viscosity value gradually increased with increasing c_{Li}, resulting in decreased ionic conductivity. Note that the LiFSA/TFEAc electrolyte is less viscous even at the extremely highest c_{Li} (= 3.2 mol dm^{-3}, corresponding to Li salt/TFEAc = 1/2, by mol.) than the concentrated electrolytes using conventional organic solvents, such as acetonitrile (AN, LiFSA/AN = 1/1.9, 138 mPa s),[6] dimethyl carbonate (DMC, LiFSA/DMC = 1/1.1, 238.9 mPa s),[7] and triglyme (G3, LiFSA/G3 = 1/1, 139 mPa s).[8] Therefore, I propose that TFEAc is a specific organic solvent that, when combined with LiFSA salt, produces a low viscous concentrated electrolyte. **Figure 6.1b** shows the electrochemical window obtained from LSV using a Pt electrode in the 3.2 mol dm^{-3} LiFSA/TFEAc electrolyte to evaluate its electrochemical stability. The reductive and oxidative currents were observed at 0.2 and 5.4 V (vs. Li/Li$^+$), respectively, resulting in a nearly 5.0 V electrochemical window that allowed for the practical use of LIBs. **Figure 6.2** shows the typical CVs for the graphite anode in the c_{Li} = 1.9, 2.4, and 3.2 mol dm^{-3} solutions. I observed clear redox currents at around 0 V (vs. Li/Li$^+$) in the 1.9 mol dm^{-3} solution (**Figure 6.2a**), that is, reductive peaks due to Li$^+$-insertion into the graphite anode from 0.2 to 0 V and oxidative peaks due to Li-ion deinsertion from 0 to 0.4 V. The observed peaks split into several peaks, which is typical for the sequential formation of stage structures of Li–graphite intercalation compounds.[9-10] A reductive current was found at ~0.5 V, which remained unchanged at subsequent cycles. This is because the reductive decomposition of the TFEAc component in the electrolyte occurred, as observed in our previous study,[1] and thus did not result from SEI formation on the graphite electrode during a cathodic scan. When c_{Li} was increased up to 3.2 mol dm^{-3} (**Figures 6.2b and c**), I found two features: (1) the redox peaks at ~ 0 V (i.e., Li$^+$-insertion/deinsertion reaction) were gradually weakened and (2) reductive decomposition at ~0.5 V was observed only at the first cycle and decreased at subsequent cycles; particularly, it completely disappeared for c_{Li} = 3.2 mol dm^{-3} solution. This behavior is typical of anion-derived SEI formation on graphite electrodes in concentrated LIB electrolytes containing TFSA or FSA anion and is attributed to the LUMO energy stabilization of such imide-type anions trapped in a specific ionic ordering structure based on multinuclear ion-pair complexes.[11-13, 6] Furthermore, I evidently observed the reductive decomposition of the FSA component beginning at ~2.0 V using the *in situ* SEIRAS spectra (1399 cm^{-1}, **Figure A6.3**), which is discussed extensively in the Supporting Information. I thus concluded that in concentrated LiFSA/TFEAc systems, (1) increasing c_{Li} enhances structural ordering, such as multiple Li$^+$···FSA$^-$···Li$^+$ ion-pairs (discussed in detail in later section), resulting in the formation of FSA-derived SEI on the graphite negative electrode; (2) the SEI formation is seriously overlapped with TFEAc decomposition at ~0.5 V, yielding a broad reductive current during the first cycle, followed by no current at this voltage after the subsequent cycles. **Figure 6.3** shows the discharge rate performance of the graphite/Li metal half-cell using the 3.2 mol dm^{-3} LiFSA/TFEAc solution, together with that for the analogous system, that is, concentrated LiTFSA/TFEAc solution with maximum c_{Li} (= 3.0 mol dm^{-3}; molar ratio of Li salt to TFEAc, 1/1.7). The discharge capacity was ~372 mAh

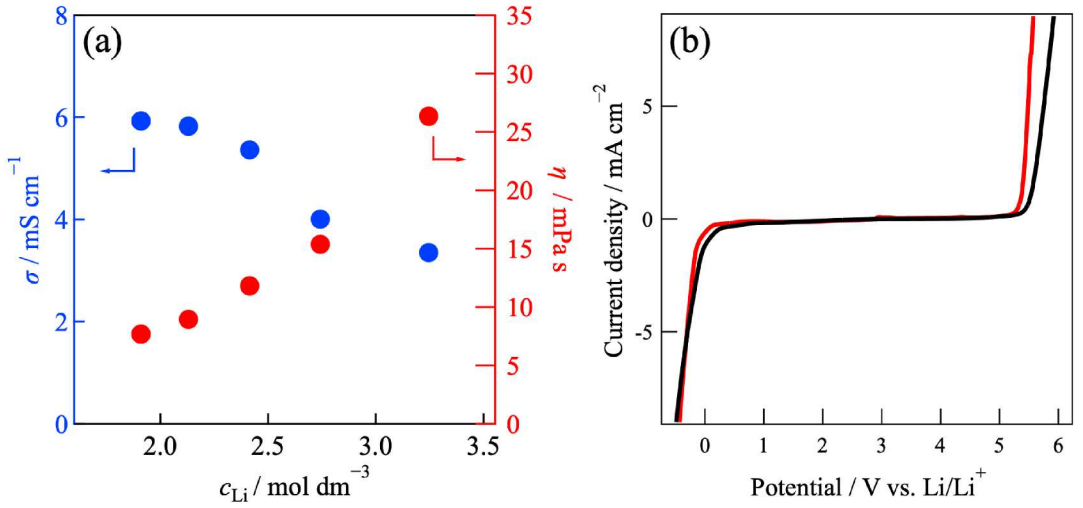

Figure 6.1 (a) Ionic conductivity (blue, left axis) and viscosity (red, right axis) for the concentrated LiFSA/TFEAc with varying c_{Li} (298 K). (b) Electrochemical window obtained using a Pt electrode in the 3.2 mol dm^{-3} LiFSA/TFEAc [scan rate: 5.0 (black) and 0.2 mV s^{-1} (red), 298 K].

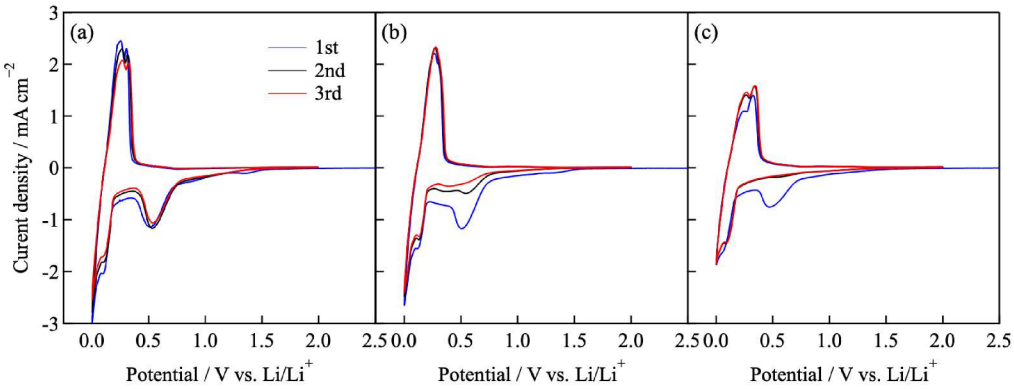

Figure 6.2 CV profiles for the graphite electrode in concentrated LiFSA/TFEAc with c_{Li} = (a) 1.9, (b) 2.4, and (c) 3.2 mol dm^{-3} (scan rate: 0.2 mV s^{-1}).

g^{-1} at 0.1 C (lowest C-rate examined herein), which is comparable to the theoretical capacity of fully lithiated LiC_6 (~372 mAh g^{-1}).[10, 14] I found that the capacity degradation in the LiFSA/TFEAc system was slight even with increasing C-rate up to 1 C to maintain the capacity of ~355 mAh g^{-1}, which significantly differed from that of the LiTFSA/TFEAc system with almost no capacity at 0.5 C. A significant degradation occurred at a higher C-rate (2 C and 5 C). **Figure A6.4** shows the cycling performance of the discharge capacity up to 50 cycles at the 0.1 C-rate for 3.2 mol dm^{-3} LiFSA/TFEAc solution.

The capacity remained ~372 mAh g^{-1} up to 10 cycles, but then gradually decreased to ~307 mAh g^{-1} up to 50 cycles. The coulomb efficiency was close to 100% over all cycles examined, except for the first cycle. It is thus plausible that in **Figure 6.3**, the observed capacity at high C-rate after multiple cycles (e.g., 97.2 mAh g^{-1} at 5 C in the 16 ~18 cycles) includes a few cycling degradations; indeed, the 5 C-capacity observed in earlier cycles was 142 mAh g^{-1}, as shown in **Figure**

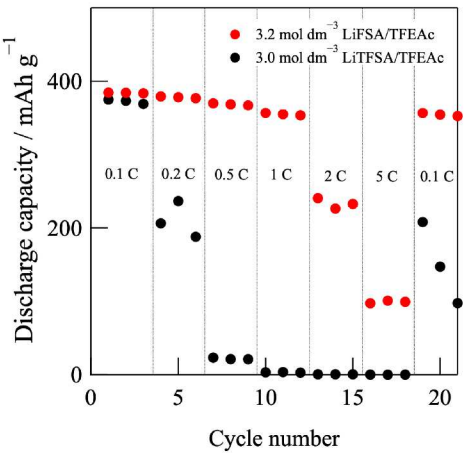

Figure 6.3 Discharge capacity of the graphite electrode in 3.2 mol dm^{-3} LiFSA/TFEAc (red) at various C-rates, together with that in 3.0 mol dm^{-3} LiTFSA/TFEAc (black). The 1 C rate corresponds to 1.256 mA.

A6.5. To gain more insights into the electrode reaction mechanism, I estimated the activation energy of a Li$^+$-insertion reaction using the temperature dependence of AC impedance spectra.

6.3.2 *Activation energy in the Li-ion insertion*

Figure A6.6 shows the AC impedance spectra (as a form of Nyquist plot) with various potential E at 298 K for the graphite electrode in 3.2 mol dm^{-3} LiFSA/TFEAc solution. A larger semicircle (in the lower frequency region around approximately 4 Hz) appeared at ~0.4 V,[4-5] corresponding to the onset-E of Li$^+$-insertion reaction, and decreased in diameter as E decreased. This result suggests that this semicircle originates from the resistance in the charge transfer process (R_{ct}), that is, Li-ion transfer resistance at the electrode/electrolyte interface, corroborating the results obtained in conventional carbonate-based electrolytes.[5] Using the temperature dependence of the R_{ct} values (**Figure A6.7**) at a potential of 0.1 V, I determined the activation energy E_a for the Li$^+$-insertion reaction according to the Arrhenius equation, that is, $1/R_{ct} \propto A\exp(-E_a/RT)$,[4] where T, A, and R denote the absolute temperature, frequency factor, and gas constant, respectively. The results are shown in **Figure 6.4**. The plots show an ideal straight line for calculating the E_a value from the slope, which was 19.9 ± 0.6 kJ mol^{-1}. Notably, in conventional carbonate electrolytes, such as $LiClO_4$/EC+DMC (1:1, by vol.) with approximately 1.0 mol dm^{-3} of Li salt, the characteristic E_a for the Li$^+$-insertion reaction is 53 – 59 kJ mol^{-1}.[5] The E_a value originates from the decoordination of EC from the Li-ion solvation complexes at the electrode/electrolyte interface, which controls a charge transfer process in the graphite electrode reaction (Li$^+$-insertion reaction). Therefore, the resulting E_a value (= 19.9 kJ mol^{-1}) is specifically lower than that in the conventional carbonate electrolytes. Here, I propose that the Li ions are co-coordinated with both TFEAc and FSA, which are categorized into much weaker coordination species, in

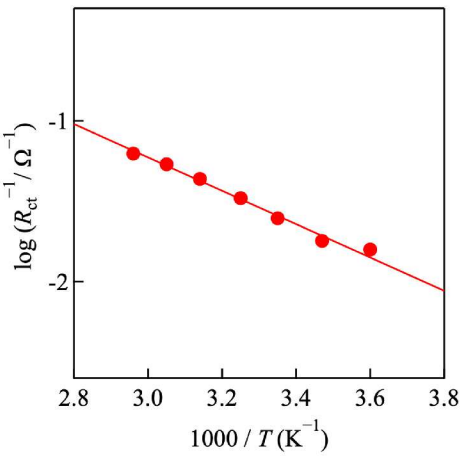

Figure 6.4 Temperature dependence of the R_{ct} values for the graphite electrode at a potential of 0.1 V in the 3.2 mol dm^{-3} LiFSA/TFEAc.

the concentrated LiFSA/TFEAc, resulting in superior decoordination in activation energy on the electrode reaction. To quantitatively determine the Li-ion coordination in the current LiFSA/TFEAc system, I combined HEXTS experiments and all-atom MD simulations to visualize the ordered Li-ion complex structures that are competitively surrounded by TFEAc and FSA.

6.3.3 *Ordered Li-ion complex structures*

Figure 6.5 shows the X-ray structure factor $S(q)$ and the corresponding radial distribution function $G(r)$ obtained from the HEXTS experiments and MD simulations for the concentrated LiFSA/TFEAc solution (c_{Li} = 3.2 mol dm^{-3}). The $S(q)$ and $G(r)$ obtained for the dilute solution (c_{Li} = 1.0 mol dm^{-3}) are shown in **Figure A6.8**. In both the concentrated and dilute solutions, the MD-derived $S^{MD}(q)$ successfully reproduced the experimental $S^{exp}(q)$ in the whole q range examined (**Figures 6.5a and A6.8a**, respectively). A similar effect was found in the $G(r)$ profiles as a form of $r^2[G(r) - 1]$ for both solutions (**Figures 6.5b and S6.8b,** respectively). These results imply that the force field parameters used in the current MD simulations were valid for reproducing actual solution structures. To discuss the local coordination structure around a Li-ion, I evaluated the atom–atom pair correlation functions, $g^{MD}_{Li-X}(r)$, particularly focusing on the nearest neighbor correlations, that is, Li^+–O_{tfeac} and Li^+–O_{fsa} correlations for the Li^+–TFEAc and Li^+–FSA interactions, respectively. The resulting $g^{MD}_{Li-Otfeac}(r)$ and $g^{MD}_{Li-Ofsa}(r)$ are shown in **Figure 6.6**, together with the average coordination number $N_{Li-Ox}(r)$ calculated by integrating the corresponding g^{MD}_{Li-Ox} up to a given r. In the concentrated LiFSA/TFEAc solution (**Figure 6.6a**), a major peak appeared at approximately 1.9 Å for both $g^{MD}_{Li-Otfeac}(r)$ and $g^{MD}_{Li-Ofsa}(r)$, which corresponded to the closest Li^+–TFEAc and Li^+–FSA interactions in the primary coordination shell. The $N_{Li-Ox}(r)$ values for the Li^+–O_{tfeac} and Li^+–O_{fsa} interactions (plateau in the $N_{Li-Ox}(r)$ at r = 2.4~3.0 Å) were ~2.0 and ~2.2, respectively, indicating that Li ions are stabilized via O-coordination provided by two of TFEAc and one or two of FSA for a total coordination number of approximately 4, even in highly concentrated conditions. In the $g^{MD}_{Li-F}(r)$ functions, F atoms were not found in either TFEAc or FSA (**Figure A6.9**). Meanwhile, the Li-ion coordination prefers TFEAc [$N_{Li-Otfeac}(r)$ ~ 3.1] to FSA [$N_{Li-Ofsa}(r)$ ~ 0.9] in dilute solution (**Figure 6.6b**) to form a tetrahedral-type Li-ion complex with three O_{tfeac} and one O_{fsa}, which is similar to the coordination structure in dilute TFEAc-based solution containing LiTFSA.[1] **Figure 6.6c** shows the $g^{MD}_{Li-Li}(r)$ function, corresponding to Li^+–Li^+ correlation, in the concentrated LiFSA/TFEAc solution. Clear multiple peaks were found in the long-r range up to 20 Å (at 6.1, 8.2, 11, 13.1, and 15.7 Å), suggesting the formation of ordered Li-ion structures linked via FSA anions (see **Figure 6.6e**; snapshot confirmed in the

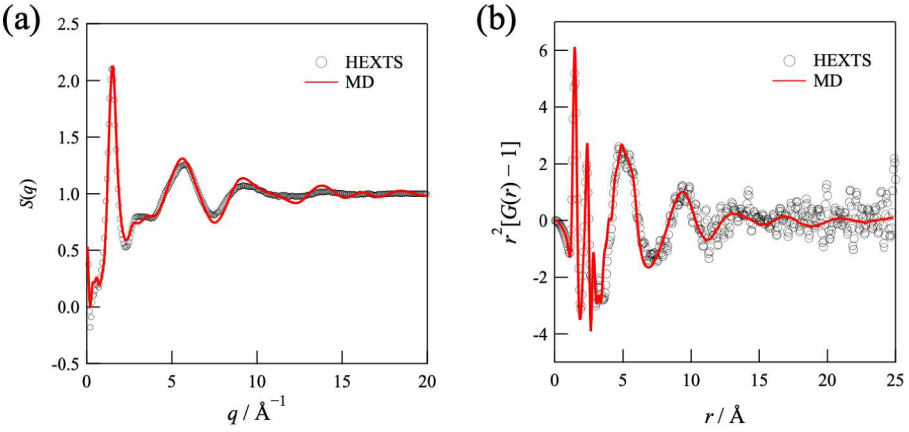

Figure 6.5 (a) X-ray structure factor $S(q)$ and (b) X-ray radial distribution function in the $r^2[G(r) - 1]$ form obtained from HEXTS experiments (open circles) and MD simulations (solid lines) for the 3.2 mol dm^{-3} LiFSA/TFEAc.

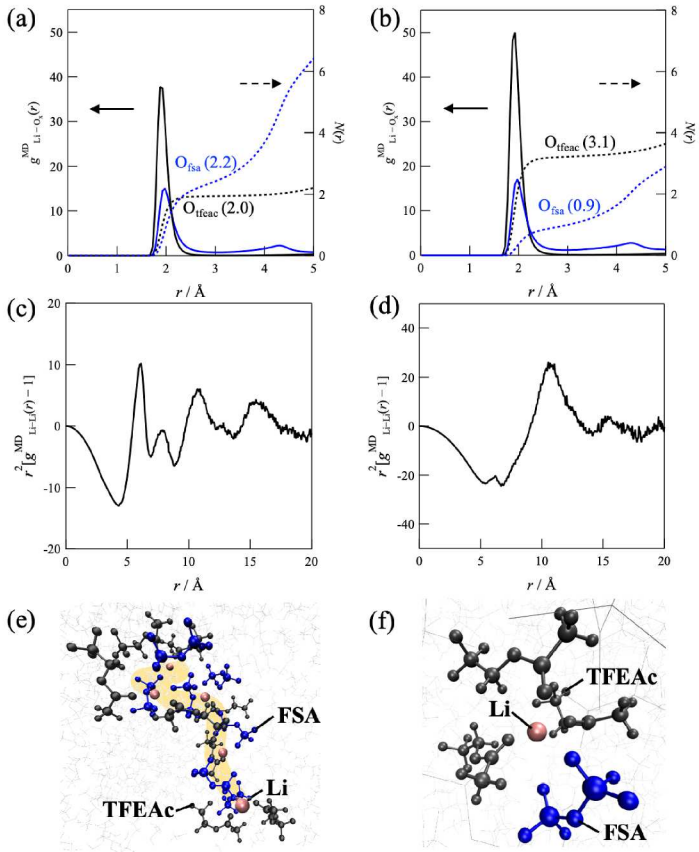

Figure 6.6 (a, b) Atom–atom pair correlation functions [$g^{MD}_{Li\text{-}Ox}(r)$: left axis, solid lines] for O atoms of TFEAc (black) and FSA (blue) around Li ions for the 3.2 and 1.0 mol dm^{-3} LiFSA/TFEAc, together with their integrated profiles (coordination number $N(r)$: right axis, dashed lines). (c, d) Atom–atom pair correlation functions between Li ions [$g^{MD}_{Li\text{-}Li}(r)$] for the 3.2 and 1.0 mol dm^{-3} LiFSA/TFEAc. (e, f) Typical snapshots confirmed in the MD simulation box for the 3.2 and 1.0 mol dm^{-3} LiFSA/TFEAc; pink: Li^+, black: TFEAc, and blue: FSA.

simulation box). There was no such a periodic peak in the dilute solution; that is, only a broad peak appeared at ~11 Å (**Figure 6.6d**). This is because the Li ions form a mononuclear ion-pair complex [$Li(TFEAc)_3(FSA)_1$] (**Figure 6.6f**) to provide a broad correlation between mononuclear Li-ion complexes. The ordered Li ions are accompanied by TFEAc molecules to produce intricate [$Li_x(FSA)_y(TFEAc)_z$] complexes in the concentrated solution, resulting in no free solvent (TFEAc) and counteranion (FSA) in the bulk.

6.3.4 *Electrode reaction mechanism*

As mentioned above, I proposed that the concentrated LiFSA/TFEAc solution exhibits much lower activation energy (E_a = 19.9 kJ mol^{-1}) for the Li^+-insertion reaction into the graphite electrode compared to those in dilute carbonate-based LIB electrolyte solutions. In the structural aspect, all TFEAc molecules and FSA anions coordinate to the Li ions to form ion-ordered complex structures in the bulk solution. To understand the molecular origin of the activation energy, that is, to identify which decoordination process of the TFEAc or FSA species trapped in the ordered Li-ion complexes mainly contributes to the experimental E_a value, I performed E_a-determination in the FSA-based ionic liquid (IL) containing high LiFSA salt concentration as a model system. That is, I assumed herein that the Li ions are coordinated with only the FSA component in the IL solution[15] containing an anion (coordination species, FSA) and two cations (IL cation and Li^+); therefore, the decoordination during the charge transfer process should originate from the coordinated FSA to fully reflect the experimental E_a value. **Figure A6.10** shows the $\log(1/R_{ct})$ vs. $1/T$ plots obtained for the concentrated IL solution, that is, 3.4 mol dm^{-3} LiFSA in 1-ethyl-3-methlyimidazolium FSA ([C_2mIm][FSA]). The resulting E_a value was 34.9 kJ mol^{-1}, which is approximately two-fold larger than that in the concentrated LiFSA/TFEAc solution (19.9 kJ mol^{-1}). This result strongly suggests that TFEAc decoordination from the Li-ion complexes is a major contribution to the specific E_a in the TFEAc system.

Based on these findings, I came to the following conclusions about the electrode reaction mechanism in

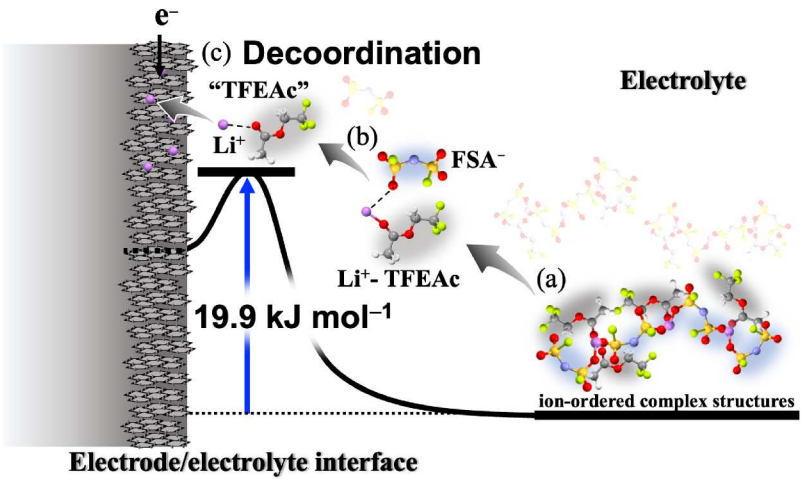

Figure 6.7 Possible electrode reaction mechanism for the graphite electrode in the concentrated LiFSA/TFEAc system: Li-ion structures (a) in the bulk electrolyte, (b) intermediate process during cathodic scanning, and (c) decoordination process at the charge transfer reaction.

the concentrated TFEAc-based solution: (1) In the bulk electrolyte, the Li ions are coordinated with both TFEAc and FSA species to exist as the ion-ordered complexes (**Figure 6.7a**). (2) The electrostatic repulsion between the negatively charged electrode and FSA anions within the ordered complexes may cause gradual rupturing the ordered structures near the electrode interface with cathodic scanning (**Figure 6.7b**). (3) At the activation state, the residual TFEAc interacted with the Li-ion are decoordinated to control the charge transfer process in the graphite electrode reaction (**Figure 6.7c**). The TFEAc molecule possesses a much weaker electron-pair donating ability (lower D_N value), that is, much weaker Li^+···TFEAc interactions, resulting in kinetically favorable decoordination and thus a lower E_a value in the concentrated LiFSA/TFEAc electrolyte.

6.4 Conclusions

Herein, I propose a kinetically favorable electrode reaction in a concentrated LIB electrolyte using a TFEAc solvent that has much weaker solvation power and LiFSA salt. The concentrated LiFSA/TFEAc electrolyte exhibited an excellent Li^+-insertion/deinsertion reaction (charge–discharge reaction) for a graphite negative electrode with significantly lower activation energy (E_a = 19.9 kJ mol^{-1}) compared with the dilute carbonate-based electrolytes for commercialized LIBs. The structural investigation based on a combined HEXTS and MD simulation revealed that in highly concentrated conditions, (1) all TFEAc molecules and FSA anions coordinate with the Li ions, that is, no free solvent and dissociated anions in the bulk solution, and hence (2) Li ions form structurally ordered Li-ion complexes co-coordinated with both TFEAc and FSA species. I found that the weakly coordinated TFEAc trapped within the ordered Li-ion complexes predominates the electrode reaction kinetics; that is, a weaker Li^+···TFEAc interaction leads to easier TFEAc decoordination from the ordered Li ions during the charge transfer process, resulting in a lower E_a value in the concentrated TFEAc-based electrolyte.

6.5 References

(1) Sawayama, S.; Ochi, R.; Mimura, H.; Morita, M.; Fujii, K. 2,2,2-Trifluoroethyl Acetate as an Electrolyte Solvent for Lithium-Ion Batteries: Effect of Weak Solvation on Electrochemical and Structural Characteristics. *J. Phys. Chem. C* **2021,** *125*, 27098-27105.

(2) Doi, T.; Fujii, R.; Aoki, Y.; Nagashima, T.; Takehara, K.; Inaba, M. Physicochemical Features of Fluorinated Ethyl Acetate-Based Highly Concentrated Electrolyte Solutions and Their Effects on Electrochemical Properties of $LiNi_{0.8}Co_{0.1}Mn_{0.1}O_2$ Positive Electrodes. *J. Phys. Chem. C* **2021,** *125*, 12578-12584.

(3) Yamada, Y.; Furukawa, K.; Sodeyama, K.; Kikuchi, K.; Yaegashi, M.; Tateyama, Y.; Yamada, A. Unusual Stability of Acetonitrile-Based Superconcentrated Electrolytes for Fast-Charging Lithium-ion Batteries. *J. Am. Chem. Soc.* **2014,** *136*, 5039-5046.

(4) Wang, J.; Yamada, Y.; Sodeyama, K.; Chiang, C. H.; Tateyama, Y.; Yamada, A. Superconcentrated electrolytes for a high-voltage lithium-ion battery. *Nat. Commun.* **2016,** *7*, 12032-12040.

(5) Ueno, K.; Yoshida, K.; Tsuchiya, M.; Tachikawa, N.; Dokko, K.; Watanabe, M. Glyme–Lithium Salt Equimolar Molten Mixtures: Concentrated Solutions or Solvate Ionic Liquids? *J. Phys. Chem. B* **2012,** *116*, 11323-11331.

(6) Aurbach, D.; Zaban, A.; Ein-Eli, Y.; Weissman, I. Recent studies on the correlation between surface chemistry, morphology, three-dimensional structures and performance of Li and Li-C intercalation anodes in several important electrolyte systems. *J. Power Sources* **1997,** *68*, 91-98.
(7) Dahn, J. R. Phase diagram of Li_xC_6. *Phys. Rev. B* **1991,** *44*, 9170-9177.
(8) Fujii, K.; Wakamatsu, H.; Todorov, Y.; Yoshimoto, N.; Morita, M. Structural and Electrochemical Properties of Li Ion Solvation Complexes in the Salt-Concentrated Electrolytes Using an Aprotic Donor Solvent, *N,N*-Dimethylformamide. *J. Phys. Chem. C* **2016,** *120*, 17196-17204.
(9) Sawayama, S.; Morinaga, A.; Mimura, H.; Morita, M.; Katayama, Y.; Fujii, K. Fluorophosphate-Based Nonflammable Concentrated Electrolytes with a Designed Lithium-Ion-Ordered Structure: Relationship between the Bulk Electrolyte and Electrode Interface Structures. *ACS Appl. Mater. Interfaces* **2021,** *13*, 6201-6207.
(10) Sodeyama, K.; Yamada, Y.; Aikawa, K.; Yamada, A.; Tateyama, Y. Sacrificial Anion Reduction Mechanism for Electrochemical Stability Improvement in Highly Concentrated Li-Salt Electrolyte. *J. Phys. Chem. C* **2014,** *118*, 14091-14097.
(11) Ohzuku, T.; Iwakoshi, Y.; Sawai, K. Formation of Lithium-Graphite Intercalation Compounds in Nonaqueous Electrolytes and Their Application as a Negative Electrode for a Lithium Ion (Shuttlecock) Cell. *J. Electrochem. Soc.* **1993,** *140*, 2490-2498.
(12) Abe, T.; Sagane, F.; Ohtsuka, M.; Iriyama, Y.; Ogumi, Z. Lithium-Ion Transfer at the Interface Between Lithium-Ion Conductive Ceramic Electrolyte and Liquid Electrolyte-A Key to Enhancing the Rate Capability of Lithium-Ion Batteries. *J. Electrochem. Soc.* **2005,** *152*.
(13) Kondo, Y.; Abe, T.; Yamada, Y. Kinetics of Interfacial Ion Transfer in Lithium-Ion Batteries: Mechanism Understanding and Improvement Strategies. *ACS Appl. Mater. Interfaces* **2022,** *14*, 22706-22718.
(14) Fujii, K.; Hamano, H.; Doi, H.; Song, X.; Tsuzuki, S.; Hayamizu, K.; Seki, S.; Kameda, Y.; Dokko, K.; Watanabe, M.; Umebayashi, Y. Unusual Li^+ Ion Solvation Structure in Bis(fluorosulfonyl)amide Based Ionic Liquid. *J. Phys. Chem. C* **2013,** *117*, 19314-19324.
(15) Jorgensen, W. L.; Maxwell, D. S.; Tirado-Rives, J. Development and Testing of the OPLS All-Atom Force Field on Conformational Energetics and Properties of Organic Liquids. *J. Am. Chem. Soc.* **1996,** *118*, 11225-11236.
(16) Price, M. L. P.; Ostrovsky, D.; Jorgensen, W. L. Gas-Phase and Liquid-State Properties of Esters, Nitriles, and Nitro Compounds with the OPLS-AA Force Field. *J. Comput. Chem.* **2001,** *22*, 1340–1352.
(17) Shimizu, K.; Almantariotis, D.; Gomes, M. F. C.; ́dua, A. ı. A. H. P.; Lopes, J. N. C. Molecular Force Field for Ionic Liquids V: Hydroxyethylimidazolium, Dimethoxy-2- Methylimidazolium, and Fluoroalkylimidazolium Cations and Bis(Fluorosulfonyl)Amide, Perfluoroalkanesulfonylamide, and Fluoroalkylfluorophosphate Anions. *J. Phys. Chem. B* **2010,** *114*, 3592–3600.

6.6 Appendix

Table A6.1 Compositions (number of ion-pair, LiFSA and TFEAc molecule), box length of the systems for MD simulations, and density (d) with c_{Li} = 1.0 and 3.2 mol dm^{-3} LiFSA/TFEAc.

c_{Li} / mol dm^{-3}	Li-FSA	TFEAc	Box length / Å	d / g cm^{-3}	
				MD[a]	Exp.[b]
1.0	170	1292	64.3	1.384	1.361
3.2	530	1060	63.8	1.542	1.530

[a] Value obtained from the present MD simulations. [b] Experimental values.

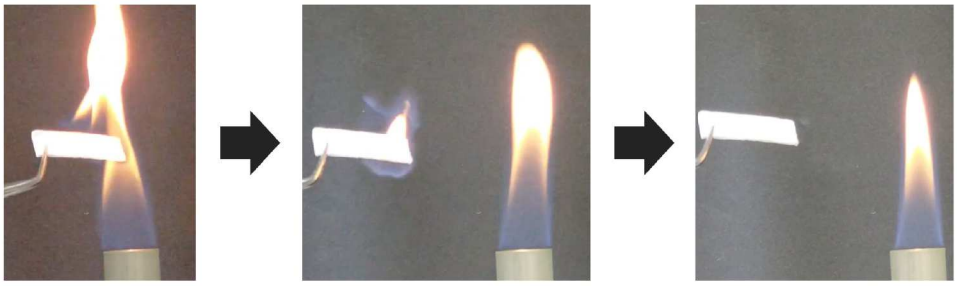

Figure A6.1 Flame test of the concentrated 3.2 mol dm^{-3} LiFSA/TFEAc solution.

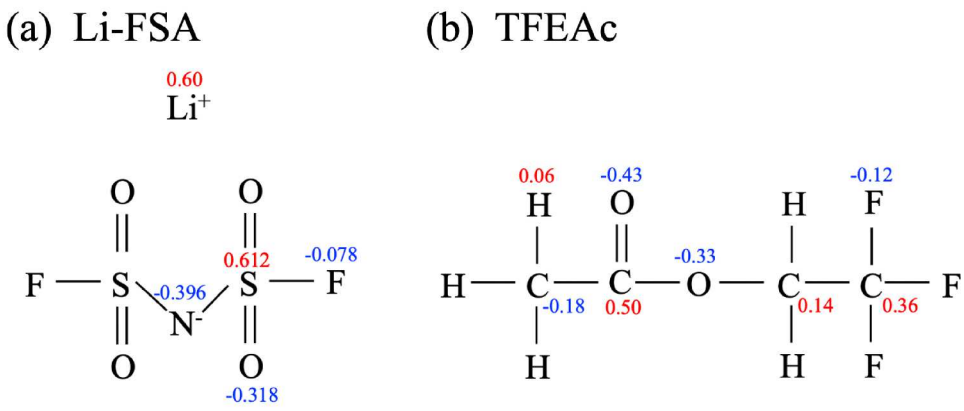

Figure A6.2 The partial charge values of (a) Li-FSA and (b) TFEAc[16-17] used in the MD simulations.

With regard to Li^+ and FSA^-, I used the modified partial charges by weighting a factor (f) to their original values,[18] in the current MD simulations. In our previous study (LiTFSA/fluorinated solvent system), I reported the optimum f values to be 0.6 (i.e., 60% of the original q^+ and q^- for Li-TFSA ion-pair), resulting in a successful agreement of experimental and simulation-derived radial distribution functions, $G^{exp}(r)$ and $G^{MD}(r)$, respectively. I thus adopted the f = 0.6 in this LiFSA/TFEAc system (**Figure A6.2a**); then, the $G^{MD}(r)$ using $0.6q^+$ and $0.6q^-$ in coulombic term successfully reproduced the corresponding experimental $G^{exp}(r)$, as shown by solid line in the **Figure 6.5**.

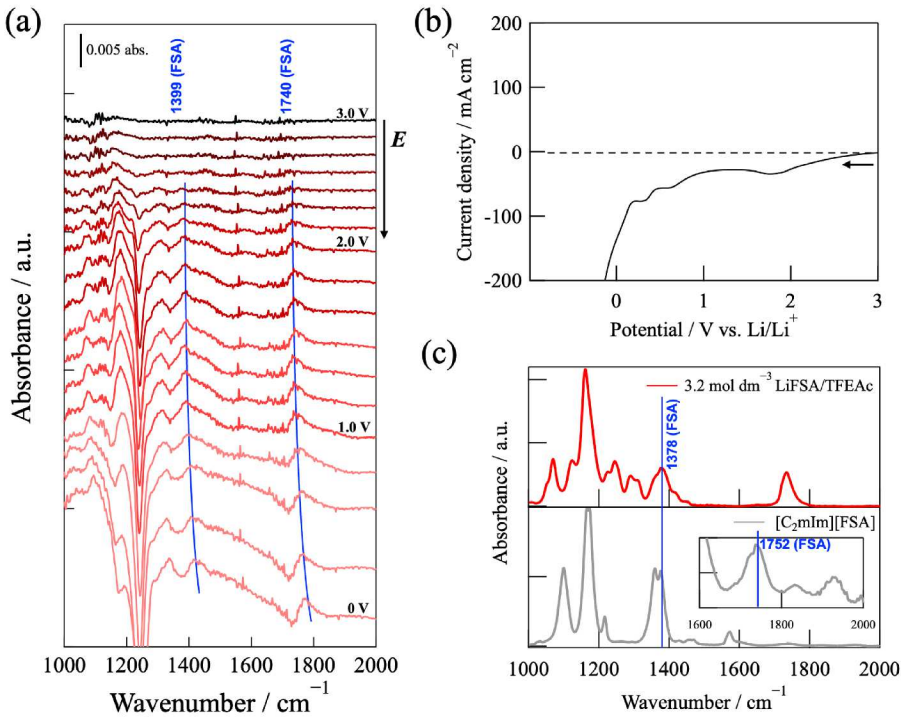

Figure A6.3 (a) Typical *in situ* surface-enhanced infrared absorption spectroscopy (SEIRAS) obtained during LSV in a potential E range of 3.0 – 0 V in the 3.2 mol dm^{-3} LiFSA/TFEAc (scan rate: 0.2 mV s^{-1}) and (b) the corresponding LSV profile. (c) ATR-IR spectra in (upper) the LiFSA/TFEAc and (bottom) 1-ethly-3-methylimidazolium FSA ([C_2mIm][FSA]). The SEIRAS spectra shown herein correspond to the difference spectra obtained by subtracting the reference spectrum at 3.0 V (vs. Li/Li$^+$) from that measured at a given potential (E). In **Figure A6.3a**, the peaks appeared at 1399 and 1740 cm^{-1} when E was decreased to ~2.0 V, and increased in intensity with decreasing E down to 0 V. These peaks can be assigned to the reductively decomposed FSA in the vicinity of the electrode; indeed, the ATR-IR spectra for the 3.2 mol dm^{-3} LiFSA/TFEAc and neat [C_2mIm][FSA] showed a significant IR peak at 1378 and 1752 cm^{-1} (**Figure A6.3c**), assigned to FSA anions[12]. I thus concluded that the FSA anions were preferentially decomposed at the electrode/electrolyte interface, leading to the formation of a stable FSA-derived SEI.

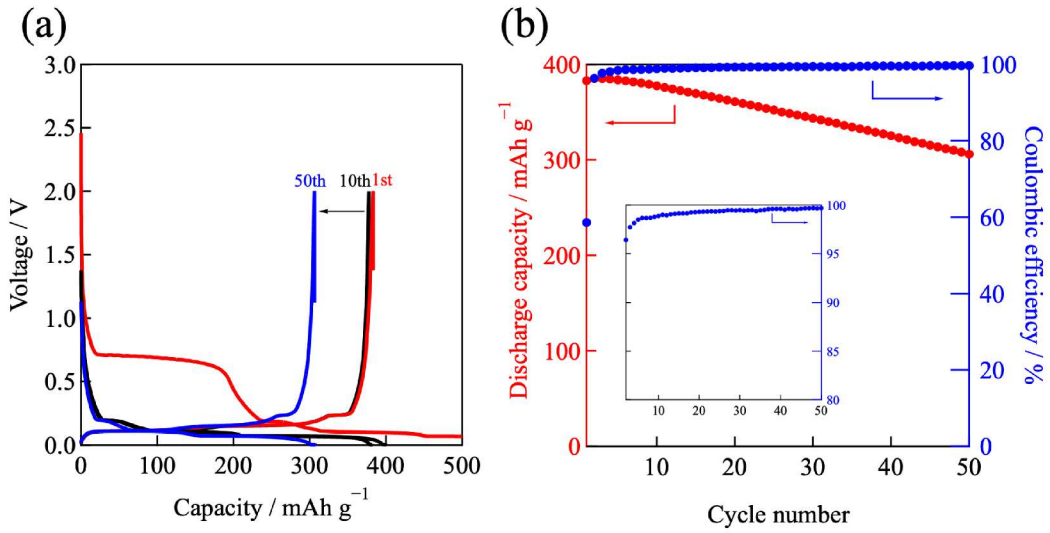

Figure A6.4 (a) Charge–discharge curves for the graphite electrode in the 3.2 mol dm^{-3} LiFSA/TFEAc at a 0.1 C rate. (b) Cycling performance (red, left axis) and coulombic efficiency (blue, right axis) of the same solution.

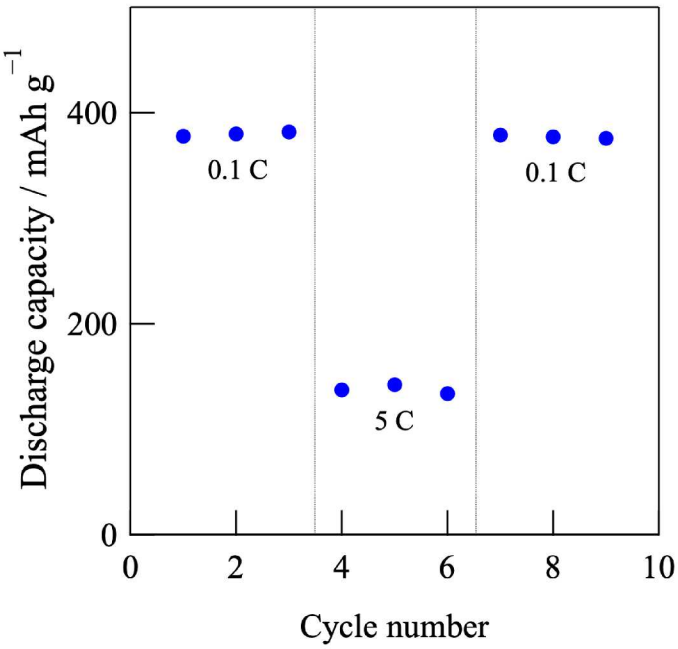

Figure A6.5 Discharge capacity of the graphite electrode in 3.2 mol dm^{-3} LiFSA/TFEAc at the C-rates of 0.1 C and 5 C.

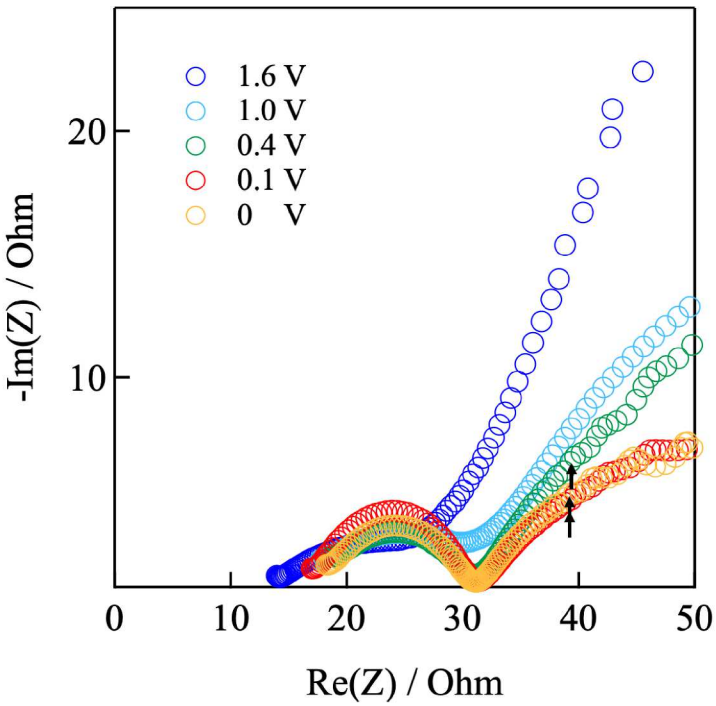

Figure A6.6 Nyquist plots observed for the graphite electrode in the 3.2 mol dm^{-3} LiFSA/TFEAc with various potential *E* at 298 K. The arrows indicate the frequency of 4 Hz.

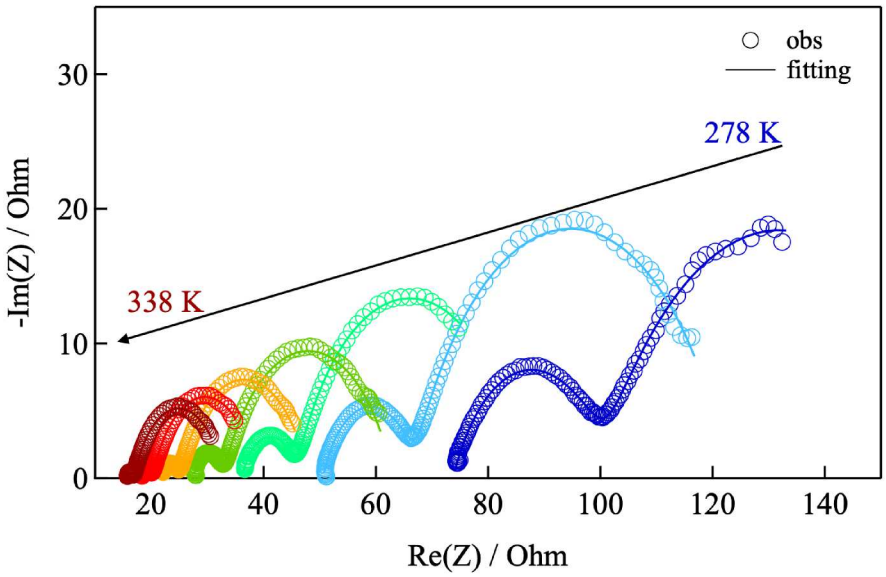

Figure A6.7 Nyquist plots observed for the graphite electrode in the 3.2 mol dm^{-3} LiFSA/TFEAc with various temperatures (278, 288, 298, 308, 318, 328, and 338 K) at a fixed potential of 0.1 V.

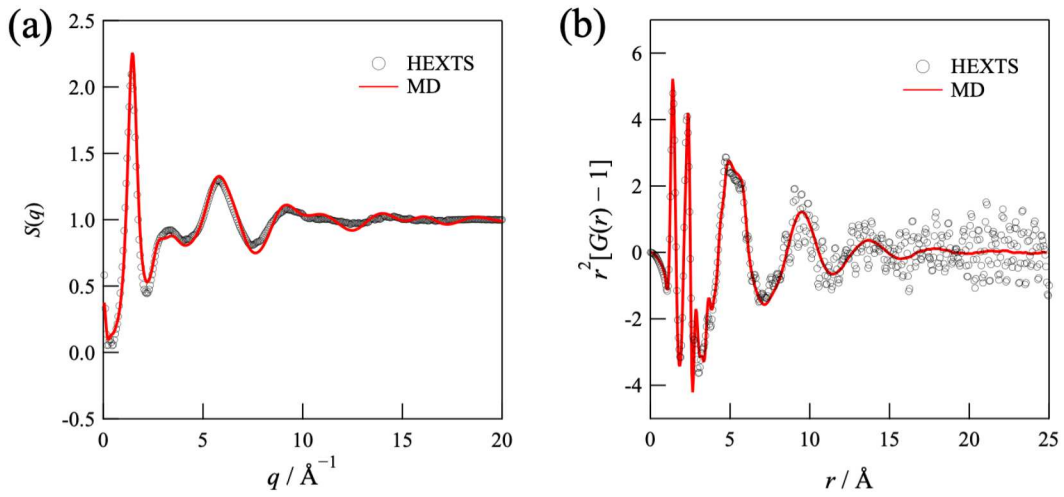

Figure A6.8 (a) X-ray structure factor $S(q)$ and (b) X-ray radial distribution function in the $r^2[G(r) - 1]$ form obtained from HEXTS experiments (open circles) and MD simulations (solid lines) for 1.0 mol dm^{-3} LiFSA/TFEAc.

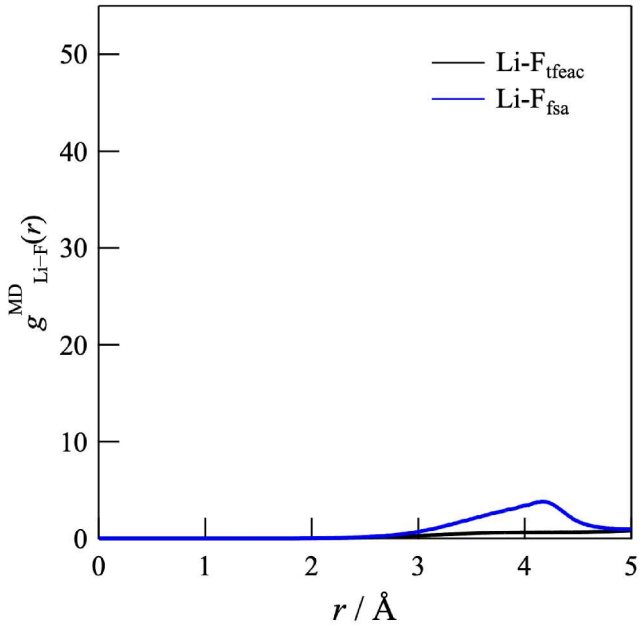

Figure A6.9 Atom-atom pair correlation functions [$g^{MD}_{Li-F}(r)$] for the F atoms of TFEAc (black) and FSA (blue) around a Li ion for 3.2 mol dm^{-3} LiFSA/TFEAc.

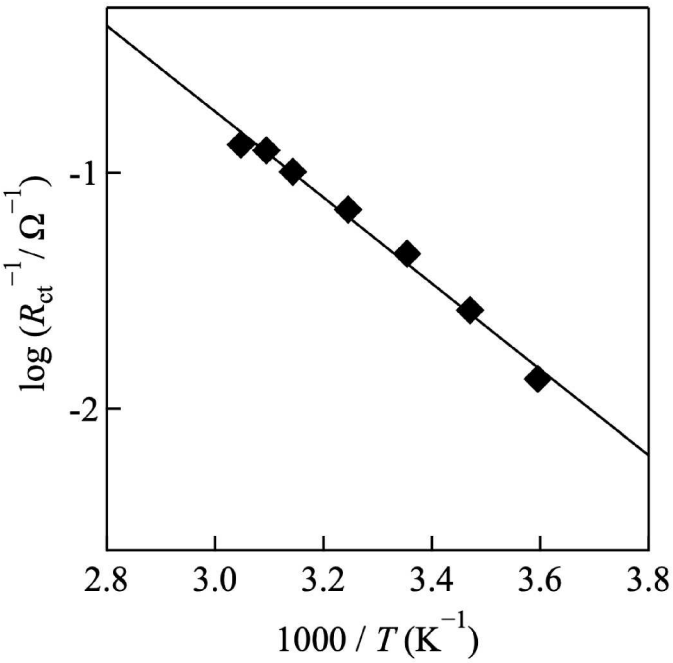

Figure A6.10 Temperature dependence of the R_{ct} values for the graphite electrode at a potential of 0.1 V in concentrated 3.4 mol dm^{-3} LiFSA/[C_2mIm][FSA].

References

(1) Sawayama, S.; Ochi, R.; Mimura, H.; Morita, M.; Fujii, K. 2,2,2-Trifluoroethyl Acetate as an Electrolyte Solvent for Lithium-Ion Batteries: Effect of Weak Solvation on Electrochemical and Structural Characteristics. *J. Phys. Chem. C* **2021,** *125*, 27098-27105.

(2) Doi, T.; Fujii, R.; Aoki, Y.; Nagashima, T.; Takehara, K.; Inaba, M. Physicochemical Features of Fluorinated Ethyl Acetate-Based Highly Concentrated Electrolyte Solutions and Their Effects on Electrochemical Properties of $LiNi_{0.8}Co_{0.1}Mn_{0.1}O_2$ Positive Electrodes. *J. Phys. Chem. C* **2021,** *125*, 12578-12584.

(3) Abe, T.; Fukuda, H.; Iriyama, Y.; Ogumi, Z. Solvated Li-Ion Transfer at Interface Between Graphite and Electrolyte. *J. Electrochem. Soc.* **2004,** *151*, A1120.

(4) Abe, T.; Sagane, F.; Ohtsuka, M.; Iriyama, Y.; Ogumi, Z. Lithium-Ion Transfer at the Interface Between Lithium-Ion Conductive Ceramic Electrolyte and Liquid Electrolyte-A Key to Enhancing the Rate Capability of Lithium-Ion Batteries. *J. Electrochem. Soc.* **2005,** *152*.

(5) Kondo, Y.; Abe, T.; Yamada, Y. Kinetics of Interfacial Ion Transfer in Lithium-Ion Batteries: Mechanism Understanding and Improvement Strategies. *ACS Appl. Mater. Interfaces* **2022,** *14*, 22706-22718.

(6) Yamada, Y.; Furukawa, K.; Sodeyama, K.; Kikuchi, K.; Yaegashi, M.; Tateyama, Y.; Yamada, A. Unusual Stability of Acetonitrile-Based Superconcentrated Electrolytes for Fast-Charging Lithium-ion Batteries. *J. Am. Chem. Soc.* **2014,** *136*, 5039-5046.

(7) Wang, J.; Yamada, Y.; Sodeyama, K.; Chiang, C. H.; Tateyama, Y.; Yamada, A. Superconcentrated electrolytes for a high-voltage lithium-ion battery. *Nat. Commun.* **2016,** *7*, 12032-12040.

(8) Ueno, K.; Yoshida, K.; Tsuchiya, M.; Tachikawa, N.; Dokko, K.; Watanabe, M. Glyme–Lithium Salt Equimolar Molten Mixtures: Concentrated Solutions or Solvate Ionic Liquids? *J. Phys. Chem. B* **2012,** *116*, 11323-11331.

(9) Aurbach, D.; Zaban, A.; Ein-Eli, Y.; Weissman, I. Recent studies on the correlation between surface chemistry, morphology, three-dimensional structures and performance of Li and Li-C intercalation anodes in several important electrolyte systems. *J. Power Sources* **1997,** *68*, 91-98.

(10) Dahn, J. R. Phase diagram of Li_xC_6. *Phys. Rev. B* **1991,** *44*, 9170-9177.

(11) Fujii, K.; Wakamatsu, H.; Todorov, Y.; Yoshimoto, N.; Morita, M. Structural and Electrochemical Properties of Li Ion Solvation Complexes in the Salt-Concentrated Electrolytes Using an Aprotic Donor Solvent, *N,N*-Dimethylformamide. *J. Phys. Chem. C* **2016,** *120*, 17196-17204.

(12) Sawayama, S.; Morinaga, A.; Mimura, H.; Morita, M.; Katayama, Y.; Fujii, K. Fluorophosphate-Based Nonflammable Concentrated Electrolytes with a Designed Lithium-Ion-Ordered Structure: Relationship between the Bulk Electrolyte and Electrode Interface Structures. *ACS Appl. Mater. Interfaces* **2021,** *13*, 6201-6207.

(13) Sodeyama, K.; Yamada, Y.; Aikawa, K.; Yamada, A.; Tateyama, Y. Sacrificial Anion Reduction Mechanism for Electrochemical Stability Improvement in Highly Concentrated Li-Salt Electrolyte. *J. Phys. Chem. C* **2014,** *118*, 14091-14097.

(14) Ohzuku, T.; Iwakoshi, Y.; Sawai, K. Formation of Lithium-Graphite Intercalation Compounds in Nonaqueous Electrolytes and Their Application as a Negative Electrode for a Lithium Ion (Shuttlecock) Cell. *J. Electrochem. Soc.* **1993,** *140*, 2490-2498.

(15) Fujii, K.; Hamano, H.; Doi, H.; Song, X.; Tsuzuki, S.; Hayamizu, K.; Seki, S.; Kameda, Y.; Dokko, K.; Watanabe, M.; Umebayashi, Y. Unusual Li^+ Ion Solvation Structure in Bis(fluorosulfonyl)amide Based Ionic Liquid. *J. Phys. Chem. C* **2013,** *117*, 19314-19324.

(16) Jorgensen, W. L.; Maxwell, D. S.; Tirado-Rives, J. Development and Testing of the OPLS All-Atom Force Field on Conformational Energetics and Properties of Organic Liquids. *J. Am. Chem. Soc.* **1996,** *118*, 11225-11236.

(17) Price, M. L. P.; Ostrovsky, D.; Jorgensen, W. L. Gas-Phase and Liquid-State Properties of Esters, Nitriles, and Nitro Compounds with the OPLS-AA Force Field. *J Comput Chem* **2001,** *22*, 1340-1352.

(18) Shimizu, K.; Almantariotis, D.; Gomes, M. F. C.; Pádua, A. A. H.; Lopes, J. N. C. Molecular Force Field for Ionic Liquids V: Hydroxyethylimidazolium, Dimethoxy-2-Methylimidazolium, and Fluoroalkylimidazolium Cations and Bis(Fluorosulfonyl)Amide, Perfluoroalkanesulfonylamide, and Fluoroalkylfluorophosphate Anions. *J. Phys. Chem. B* **2010,** *114*, 3592-3600.

Chapter 7

Conclusion

Novel nonflammable Li-ion battery (LIB) electrolytes using fluorinated organic solvents were established and characterized from the structural and electrochemical viewpoints. Among fluorinated organic solvents, tris(2,2,2-trifluoroethyl)phosphate (TFEP, Chapter 3 and 4) and 2,2,2-trifluoroethyl acetate (TFEAc, Chapter 5 and 6) were used as a main solvent to prepare the LIB electrolytes with wide c_{Li}-range from dilute up to highly concentrated condition. Particularly, I established "electrolyte science" based on the structural investigation at the molecular level from both experimental and theoretical approaches and demonstrated that the structural knowledge is helpful to understand the electrode reaction and LIB performance. Major findings throughout this study are as follows: (1) the structure of Li ions strongly depends on c_{Li}. Particularly, in highly concentrated electrolytes, Li ions form multinuclear complexes with the long-range ordered structures linked via counter-anions, which is largely different from the mononuclear Li-ion complex in dilute electrolytes. The ordered Li ion structures directly affect the electrode reaction (in this work, Li insertion/deinsertion for graphite electrode, as a model system) to enhance the oxidative/reductive stability and reaction kinetics. (2) Solvent bulkiness (i.e., size of solvent molecule) plays a crucial role on "structuredness" of Li-ion complexes in highly concentrated electrolytes. The bulky solvent, e.g., TFEP, results in less ordered Li-ion complexes (4-coordinated mononuclear Li ions) even in highly concentrated conidiation owing to the steric hinderance among TFEP molecules in the coordination sphere of Li ion. Contrary, using smaller solvent in size leads to a successful ionic ordered structure formation; indeed, Li ions in the concentrated TFEP electrolyte easily form the ordered structure when adding small molecule into the TFEP electrolyte. (3) the electron-pair donating ability (i.e., D_N value) of solvent molecule, which is a good indicator of solvation power to metal ion, controls the electrode reaction kinetics. The solvent molecule with lower D_N value (in this work, TFEAc) yields the weaker interactions between Li ions and solvent molecules, which induces the easier decoordination of Li-ion complexes at the charge-transfer process to reduce the activation energy in the electrode reaction.

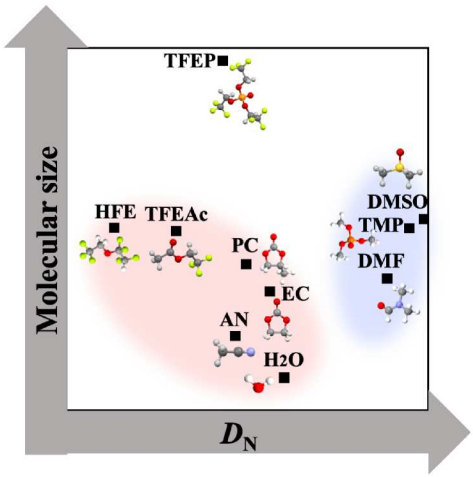

Figure 7.1 Mapping of solvent species in terms of both D_N value and molecular size of solvent molecules.

Based on these results, I can propose a simple concept to design an electrolyte component in highly concentrated system from the viewpoint of solution chemistry. **Figure 7.1** shows species mapping categorized using two features of electrolyte solvent. In this mapping, solvents placed on the bottom left (that is, smaller molecular size and lower D_N value) may be suitable to use as a main solvent for highly concentrated LIB electrolytes to provide the specific ordered Li-ion complexes and the kinetically favorable electrode reaction kinetics. On the other hand, those on the top right is hard to observe LIB electrode reaction.

Publication List

・Publication paper in regard to doctoral dissertation

1. S. Sawayama, Y. M. Todorov, H. Mimura, M. Morita, and K. Fujii* "Fluorinated alkyl-phosphate-based electrolytes with controlled lithium-ion coordination structure" *Phys. Chem. Chem. Phys.*, **21**, 11435-11443 (2019). (Chapter 3)

2. S. Sawayama, A. Morinaga, H. Mimura, M. Morita, Y. Katayama, and K. Fujii* "Fluorophosphate-Based Nonflammable Concentrated Electrolytes with a Designed Lithium-Ion-Ordered Structure: Relationship between the Bulk Electrolyte and Electrode Interface Structures" *ACS Appl. Mater. Interfaces,* **13**, 6201-6207 (2021). (Chapter 4)

3. S. Sawayama, R. Ochi, H. Mimura, M. Morita, and K. Fujii* "2,2,2-Trifluoroethyl Acetate as an Electrolyte Solvent for Lithium-Ion Batteries: Effect of Weak Solvation on Electrochemical and Structural Characteristics" *J. Phys. Chem. C*, **125**, 27098-27105 (2021). (Chapter 5)

4. S. Sawayama, R. Ochi, T. Kawaguchi, Y. Katayama, M. Morita, and K. Fujii* "Effect of a Weak Coordination Solvent on a Kinetically Favorable Electrode Reaction in Concentrated Lithium-Ion Battery Electrolytes" *ACS Appl. Energy Mater.,* **6**, 989-996 (2023). (Chapter 6)

・Other Publications

1. M. Sogawa, S. Sawayama, J. Han, C. Satou, K. Ohara, M. Matsugami, H. Mimura, M. Morita, and K. Fujii* "Role of Solvent Size in Ordered Ionic Structure Formation in Concentrated Electrolytes for Lithium-Ion Batteries" *J. Phys. Chem. C*, **123**, 8699-8708 (2019).

2. S. Takano, S. Sawayama, J. Han, and K. Fujii* "A Homogeneous Polymer Network Organogel Prepared in the Concentrated Lithium-ion battery Electrolytes Using a Nonflammable Fluorinated Solvent" *Chem. Lett.,* **51**, 142-145 (2022).

3. M. Shibata, S. Sawayama (co-first), M. Osugi, and K. Fujii* "Structural aspect on "Salting-in" mechanism of PEG chains into a phosphonium-based ionic liquid using lithium salt" *J. Mol. Liquids,* **366**, 120255 (2022).

4. K. Suzuki, S. Sawayama (co-first), Y. Deguchi, R. Sai, J. Han, and K. Fujii* "Structural and electrochemical study of lithium-ion battery electrolytes using an ethylene sulfite solvent: from dilute to concentrated solutions" *Phys. Chem. Chem. Phys.,* **24**, 27321-27321 (2022).

5. Y. Chikaoka, N. Nakata, K. Fujii, S. Sawayama, R. Ochi, E. Iwama, N. Okita, Y. Harada, Y. Orikasa, W. Naoi, and K. Naoi "Strategy for Ultrafast Cathode Reaction in Magnesium-Ion Batteries Using BF_4 Anion Based Dual-Salt Electrolyte Systems: A Case Study of $FePO_4$" *ACS Appl. Energy Mater.,* **6**, 4657-4670 (2023).

Acknowledgements

Firstly, the author wishes to express deepest gratitude to **Prof. Kenta Fujii,** Yamaguchi Uni., who suggest the subject matter of this study and helped the author to achieve better understanding on the science of solution chemistry through many extensive discussions. His guidance helped me in all the time of research and writing of this thesis.

The author expresses her thank to Assoc. Prof. Masaru Matsugami, Kumamoto Univ., for their helpful advice and guidance of MD simulations.

The author also expresses her thank to Dr. Asuka Morinaga and Assoc. Prof. Yu Katayama, Osaka Univ., for their valuable discussion and kind support for SEIRAS experiments.

The author also expresses her thank to Assoc. Prof. Koji Ohara Shimane Univ., for their kind support to teach measurements method for HEXTS experiments.

The author expresses her thank to Prof. Masayuki Morita, Kyoto Univ., for their valuable discussion and kind support for writing papers.

The author also expresses her thank to the members of laboratory, Yamaguchi University.

Lastly, the author wishes to express her deepest gratitude to her parents who gave her a chance for further education, supported and encourage her throughout this study.